Applications of Microwave Antenna Array for Wireless Power Transmission and Radar Imaging in Complex Environment

Ce Zhang

A dissertation
submitted in partial fulfillment of the
requirements for the degree of

Doctor of Philosophy

University of Washington

2016

Reading Committee:

Yasuo Kuga, Chair

Akira Ishimaru

James A. Ritcey

Program Authorized to Offer Degree:
Electrical Engineering

University of Washington

Abstract

Applications of Microwave Antenna Array for
Wireless Power Transmission and Radar Imaging in Complex Environment

Ce Zhang

Chair of the Supervisory Committee:
Professor Yasuo Kuga
Department of Electrical Engineering

The focus of my research interests lies in the application of microwave antenna array system and array signal processing techniques to the problems in wireless power transmission and radar imaging. The two research areas share the same underlying mathematical principle of time reversality of electromagnetic wave propagation. Based on this principle, the array antenna system and the associated signal processing algorithm are further improved to adapt to different scenarios.

In my dissertation, the first part presents an optimal algorithm for wireless power transmission with beamforming array. The optimal weight distribution on antenna array elements is found based on time reversal eigenmode technique. Our method is adaptive to the medium of the channel and can be applied to arbitrarily positioned antenna without degradation of efficiency. This novel method is analytically studied and verified with numerical electromagnetic simulations.

The second part presents a new problem called "Hard-Wall Radar Imaging" (HWRI) has been proposed when the electromagnetic waves cannot penetrate the shielding walls (such as metallic walls). The research methodology involves algorithm development combined with experimental results to gain more insights into the real microwave imaging system. First, we implemented the imaging system with the conventional time reversal DORT (Decomposition

of Time-Reversal Operator) imaging algorithm and adapted it into a new signal processing technique (multiplicative array technique) to obtain the image in the proposed scenario. Second, after having identified the drawbacks of the first imaging system, the imaging system is improved to distributed MIMO radar configuration. The new imaging algorithm is also developed based on the techniques of Direction-of-Arrival(DoA) estimation and adaptive nulling. From this algorithm, the experimental results show that the new imaging system can localize two targets correctly. To resolve the problem of spurious clutter reflection, a new unidirectional UWB antenna is developed using the technique crossed dipoles and integrated into a dual linear polarized array for the application of high-resolution two-dimensional imaging.

TABLE OF CONTENTS

LIST OF FIGURES

LIST OF TABLES

ACKNOWLEDGMENTS

This work is not just a summary of my past research in Electromagnetics and Remote Sensing Laboratories(ERSL), but also a record of my past five years in graduate school. First and foremost, I would like to thank my advisor Prof Kuga, who led me into the world of electromagnetics. In my research, he has given the freedom to grow as an independent researcher and the flexibility to explore areas in which I am interested. The research experience in ERSL will be on of most precious experience in my future life and career.

I would like to express my gratitude to Prof Ishimaru for instructing me, guiding me and enlightening me through the past five years. He is a genuine master and role model for me. In my graduate life, whenever I need help or discussion, he is always there to help me. His insightful thoughts into electromagnetics are one of the most important reasons for me to complete my research work.

Furthermore, I would like also say thank you to Prof Kutz and Prof Ritcey for serving on my committee. I am also grateful to Prof Rudell, who has taught me almost all the RF circuit design courses in graduate school.

My Ph.D. life in the past five years was stressful and struggling to me. Thanks to the constant support from my family members, I could survive and complete my degree. At this moment, I would like to thank my parents and my wife for being behind me in the past five years. The completion of Ph.D. degree is not an end, but a new start for the future. After all, I believe, no matter where I am, these five years at the University of Washington will be kept in my memory for the whole life.

DEDICATION

To my parents and my dear wife, Ran Sun

Chapter 1

INTRODUCTION

With the publication of A Dynamical Theory of the Electromagnetics(EM) Field in 1865, James Clerk Maxwell demonstrated that electric and magnetic fields travel through space as waves moving at the speed of light and described the EM wave propagation elegantly with the famous Maxwell's Equation. Thanks to Maxwell's work, the whole world has gained more insightful understanding oft the wave propagation, from which a variety of applications have arisen, such as wireless communication, radar, and remote sensing. The control of EM waves has reshaped the human life and behavior in past century.

1.1 Research Motivations

As described in Maxwell equation, the radiated field in open space is unbounded and follows the Transverse Electromagnetic(TEM) mode propagation. However, in the real world, the propagation medium is rich of scatterers and too complex to predict its behavior. Therefore, the wave propagation in a complex environment is extremely challenging for some applications. The time reversal(TR) techniques have been widely studied since the first work by M.Fink in 1989 [30]. This technique is built on the basis of the TR invariance of the Maxwell equation and achieves the focusing onto the scatterers selectively based on the received signal. This focusing effect implies the electric field concentration in the area of the scatterers/targets and viewed from different perspectives in different applications. In the wireless communication, the focusing effect means the improvement of signal-to-noise ratio in the complex medium. In the wireless power transmission, the focusing effect means the enhancement of the power transmission efficiency. In the radar imaging application, the

focusing effect means that the identification of focusing position is equivalent to the localization or even imaging of the object/scatterers. There have been extensive studies on its applications of wireless communications, especially underwater communication. In this dissertation, we will start with its applications on wireless power transmission(WPT) and radar imaging but not limited to the time reversal technique.

To implement the genuine wireless charging, the WPT system has to make use of large scale antenna array to improve the transmission efficiency and phased array technique to perform the fast beam steering, at the transmitter side. At the receiver side, the large antenna array is required to intercept more incident power wave, so the point source approximation in TR technique is not valid. The simple use of TR method gives lower the transmission efficiency in the scenario with large receive aperture size and short range of power delivery. The aim of my research is to propose an optimal beamforming technique to maximize the transmission efficiency in any propagation medium.

The conventional TR imaging is useful for imaging point scatterers in the cluttered and rich scattering environment, as long as the wave propagation in the medium satisfies the reciprocity, which is true in almost all cases. In recent years, there have been many studies on "Through Wall Radar Imaging" based on the waves from the sensors which penetrate through the wall to form images and TR imaging a good candidate to resolve such a problem. However, a metallic shield is used as "Anti-imaging" wall and makes TWRI technology useless in the battlefield. Moreover, if the objects are completely hidden by non-penetrating (hard) walls/obstacles, which is referred as "Hard Wall Radar Imaging" (HRWI) in [42], the TR imaging is not so powerful as usual due to the limited number of the path from antenna/sensor to object. The aim of this dissertation is to propose a new imaging algorithm for HWRI and build a microwave system that can image and detect an object in an experiment.

1.2 Overview and Organization

Chapter 2 presents the applications of TR signal processing in adaptive array beamforming. The transmission efficiency of WPT has been clarified, and the EM field propagation from the power transmitter to the receiver has been formulated after the experimental studies. Based on the formulation, it has been proved that the proposed TR eigenmode technique gave the optimal WPT efficiency and verified with the commercial EM simulator.

Chapter 3 presents the applications of TR signal processing in HWRI application. The conventional time reversal imaging technique is modified with multiplicative array technique and validated with both analytical formulation and numerical simulations.

Chapter 4 demonstrates a ultrawideband (UWB) microwave antenna array system, which is used for the experiment work of HWRI. The modified TR imaging technique in Chapter 2 is implemented with a multistatic array system in Anechoic Chamber to validate its algorithm. However, it has been found that the multistatic configuration suffers from the low signal-to-noise ratio (SNR) and signal-to-clutter ratio (SCR). Then the system is upgraded to bistatic MIMO (Multiple-In-Multiple-Out) configuration, which has a high gain transmit antenna and wide beamwidth receive antenna. This improved microwave imaging has been shown successfully localize multiple two objects behind the shielding wall.

Chapter 5 provides an enhanced design of UWB receive antenna and the associated microwave array configuration. This antenna structure employs the crossed-dipole technique, which uses one electric dipole and one virtual magnetic dipole, so as to enable the placement of UWB reflector below the broadside antenna. Thanks to such a UWB receive antenna elements, the SCR can be further improved.

Chapter 6 gives a brief discussion on the future development of microwave imaging system, which can resolve the false pair problem in the microwave imaging system in Chapter 4 and Chapter 7 provides a summary of my past research work in graduate school.

Chapter 2

OPTIMAL ARRAY BEAMFORMING FOR MICROWAVE POWER TRANSMISSION IN COMPLEX ENVIRONMENT

Wireless Power Transfer(WPT) is a popular research field in recent years and can be categorized into three approaches: inductive coupling, laser beaming and microwave power transmission(MPT). MPT system operates at the microwave frequency and transfers the energy to more than a few wavelengths. It has its unique advantages of supplying power to non-accessible and mobile receivers. The overall efficiency, which is the ratio between available DC power at receiver and supplied DC power at the transmitter, depends on both circuit design and wave propagation. As a comprehensive theory of MPT system is not available, this chapter starts with the study of MPT system from the perspectives of mathematical formulation and the experiment in an indoor environment, in Section 2.2. The preliminary study leads to the conclusion that highly directional wireless transmitter is very useful in the MPT system for achieving high transmission efficiency. For this reason, phased array antennas with beamforming functionality are usually used to direct the electromagnetic wave towards mobile receivers, and adaptive array algorithms are implemented to enable wireless power focusing in a complex environment. Section 2.4 presents a novel beamforming algorithm, which is proven to give the optimal transmission efficiency and applies to the arbitrarily positioned unequal array based on our problem formulation. To verify this algorithm, Section 2.5 validates it with numerical electromagnetic simulation in different cases. The numerical comparison of these examples shows that this algorithm gives higher transmission efficiency over other optimal beamforming algorithms discussed in Section 2.3.

2.1 Background of WPT

Wireless Power Transfer(WPT) is a popular research field in recent years and can be categorized into three approaches: inductive coupling, laser beaming and microwave power transmission(MPT). Microwave power transmission has its unique advantages for its ability to supply power to not-accessible and mobile receivers and is also called long-range wireless power transmission. As summarized in [61], it has a variety of applications such as powering ubiquitous sensor nodes at low power level [78], and transferring energy to electrical vehicle [69] [67], unmanned aerial vehicles(UAV)and high altitude platforms(HAPs)at high power level [32] [66]. Also, MPT has also been proposed and implemented in the very-high-power transmission from the space to earth, which is called "Solar Power Satellites"(SPSs) [62].

In the long distance WPT, the major power loss is attributed to the low transmission efficiency in the propagation medium, so the key challenge is how to maximize the efficiency using beamforming towards the receivers. The radiated field of transmit array elements adds up coherently to create a narrow beam in the direction of receive aperture and the direction of the beam is determined by weight distribution at each array elements. The conventional array synthesis technique arises from previous studies on phased array design. In previous studies, the array synthesis technique is modeled using the array factor and the multi-objective optimization is carried out to find the solution to beam steering with the constraints such as sidelobe level and beamwidth [68]. However, it is widely acknowledged by antenna designers that the assumption that element gain pattern can never be uniform for various reasons, especially for a small array. Besides, the performance of beam steering is also degraded due to the variance of element position and unequal element pattern. For these reasons, the retrodirective/phase conjugating array is one possible way for fast and adaptive beam steering [34] and the time reversal synthesis technique is proposed for arbitrarily structured antenna array with [105].

The aforementioned methods are favorable to obtain a predefined antenna pattern with the beam focused towards a certain direction. But when the light-of-sight(LOS) is not avail-

able, and the propagation medium is fast-changing, the beamforming requires the dynamic measurement of channel characteristics. Thus, the MIMO (Multiple-In-Multiple-Out) system is required to implement the digital beamforming, and the antenna array excitation is determined through the signal processing of the probed channel information. Eigenbeamforming is a well-known adaptive array processing technique for its capability of maximizing the signal-to-noise ratio(SNR) [107] at baseband. However, for the application of WPT, the transmission efficiency is to be maximized, so a different algorithm and formulation are needed to approach the optimal excitation.

In this chapter, we demonstrate the energy focusing effect by the time reversal signal processing and discusses how it is applied to optimize the transmission efficiency of the wireless power transmission. In Section 2.2, the power, and efficiencies are clarified and the microstrip antenna array used in the numerical example in Section 2.4 is also formulated in the frequency domain. Section 4.3 presents a new beamforming technique based on the time reversal principle and eigenbeamforming, which is defined as time reversal eigenmode technique in the application of large-scale array beamforming. Furthermore, the representative examples are simulated in the numerical electromagnetic simulator to compare the proposed methods with other beamforming techniques in Section 2.5.

2.2 Microwave Power Transmission System

Microwave power transmission(MPT) is a promising technology for its capability of supplying energy to receivers over a long range, so it is also called long distance wireless power transmission in [61]. MPT has a variety of applications such as powering ubiquitous sensor nodes at low power level [78], and transferring energy to electrical vehicle [69] [67], unmanned aerial vehicles(UAV)and high altitude platforms(HAPs)at high power level [32] [66]. Also, MPT has also been proposed and implemented in the very-high-power transmission from the space to earth, which is called "Solar Power Satellites"(SPSs) [62].

The estimation of MPT system efficiency with high accuracy is a challenging task, as there is no theory available for accurately modeling the electromagnetic wave radiation and

reception. We start this section with the general formulation of the MPT, which clarifies the efficiencies of different building blocks in MPT system. Then we study the transmission efficiency from different perspectives. If the gain of transmitting and receiving antenna is known, the quick estimation of transmission efficiency is easy, but its accuracy is highly limited. If the channel transfer matrix between the transmit and receive array and impedance matrix of transmit array can be measured with the built-in hardware in the RF system, a more accurate and dynamic transmission efficiency can be found with our proposed model in this section. Following the theoretical study, an experiment has been carried out in the lab environment with clutters such as equipment and furniture. The measurement data is analyzed with the help of simulation data and gives us an insight into the power loss contribution of the MPT system. The experiment shows that the propagation loss contributes to the most significant percentage of system loss, given the highly efficient wireless power transmitter and receiver.

2.2.1 Problem Formulation

In the MPT system, the DC power is modulated with RF carrier and radiated from transmitting antenna onto "rectenna", which collects and converts the impinging power of microwave to available DC power. As shown in [61], five efficiencies are defined respectively to evaluate the efficiency of these five building blocks(Fig.2.1). The overall efficiency (end-to-end efficiency) is the ratio between available DC power at receiver and supplied DC power at the transmitter, which is the product of these five efficiency values from each building block.

Antenna is a transducer to bridge circuit theory and field theory. Since the excitation weight of antenna array is normally controlled by circuit elements and transmission efficiencies are evaluated at the circuit level, the powers are expressed in terms of the voltage and current vectors. The definitions of power are firstly clarified in this section so that we can clearly set an optimization goal.

In array antenna system, each array elements is not independent, and the radiated fields interfere to form the radiation pattern. In this way, in the far field, the array is treated as

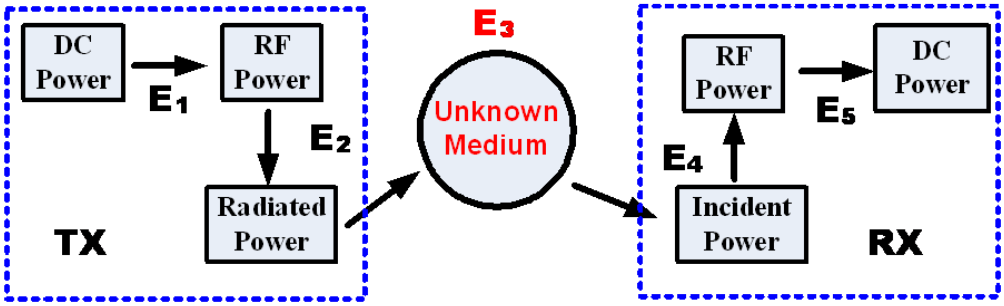

Figure 2.1: Microwave power transmission system: E_1 to E_5 are power transfer efficiencies

a single antenna and propagated in a spherical coordinate with the array at the origin. The total radiated power (P_{rad}) can be expressed in terms of the current fed to each port($\mathbf{I}$) and mutual impedance matrix ($\mathbf{Z}$). The real part of $\mathbf{Z}$ corresponds to the radiated energy while the imaginary part corresponds to the reactive energy stored in near field region.

$$P_{rad} = \frac{1}{2}\mathbf{V}^H\mathbf{I} = \frac{1}{2}\mathbf{V}^H\Re\{\mathbf{Z}_A^{-1}\}\mathbf{V} \tag{2.1}$$

The total power(P_Ω) can also be computed by taking the integral over the enclosing sphere with antenna at center. Moreover, the power focused at the angular region Ψ given by receive aperture (P_Ψ) is also defined for the beamforming optimization. These expressions can be similarly simplified into the product of vectors [68].

$$P_\Omega = \int_\Omega W_n dS \tag{2.2}$$

$$P_\Psi = \int_\Psi W_n dS \tag{2.3}$$

where W_n is Poynting flux density.

By energy conservation, the radiated power (P_{rad}) is equal to the power enclosed by the sphere (P_Ω), and is related to the input power by reflection coefficiency(Γ) of antenna ports: $P_{rad} = (1 - |\Gamma|^2)P_{in}$. Normally the antenna impedance is matched to the port impedance, so the reflection coefficient is approximately equal to 0 (in this condition, $P_{rad} = P_{in}$).

The incident power with matched load is summed up at the receiver side, as the incident field induces RF currents at each port of receive antenna. The transmission efficiency (E_3) in Fig. 2.1, which connects the transmit and receive array, is therefore optimized in power beamforming.

$$E_3 \triangleq \frac{P_{inc}}{P_{rad}} \tag{2.4}$$

In array synthesis theory, the beam collection efficiency (BCE) is usually used to evaluate the ability to shape the total power (P_Ω) towards the targeted angular region (P_Ψ) [68]. The overall efficiency is defined as the ratio between the total available RF power ($P_{L,tot}$) and the total input power at transmit array($P_{in,tot}$), which includes the efficiency of transmit antenna (E_2), transmission efficiency(E_3) and receive antenna (E_4).

$$BCE \triangleq \frac{P_\Psi}{P_\Omega} = \frac{P_\Psi}{P_{rad}} \tag{2.5}$$

$$\eta \triangleq E_2 E_3 E_4 = \frac{P_{out}}{P_{in}} \tag{2.6}$$

Since BCE is proportional to the transmission efficiency (E_3), BCE is usually the optimization goal instead of the transmission efficiency for the simplicity of mathematical formulation with array factor(AF). However, in the scenario with multipath and high-absorbing or reflection obstacles, the AF and BCE are not valid for optimization as the line-of-sight(LOS) is not available.

2.2.2 Transmission Efficiency based on Antenna Parameters

The electromagnetic field radiated from the antenna can be described as plane wave propagation in the far field, where the power of radiation decays as the square of the distance. In most of the wireless applications, the antenna operates in the region of far field and the transmission efficiency is computed in the way of link budget calculation with the help of the well-known Friis transmission equation. The complete version of Friis transmission equation

is usually expressed as (2.7) in terms of antenna gain.

$$\frac{P_{rx}}{P_{tx}} = G_{tx}G_{rx}(\frac{\lambda}{4\pi R})^2(1-|\Gamma_{tx}|^2)(1-|\Gamma_{rx}|^2)|\hat{a_{tx}}\cdot\hat{a_{rx}}^*|^2 \tag{2.7}$$

where G_t denotes the gain of transmit antenna and G_r denotes the gain of receive antenna. R is the distance between transmit antenna and receive antenna. $|\Gamma_t|$ and $|\Gamma_r|$ are the reflection coefficient of transmit and receive antenna respectively. $\hat{a_r}$ denotes the polarization vector of receive antenna while $\hat{a_t}$ denotes the incident wave electric field vector or polarzation vector of transmit vector in LOS propagation. The term $|\hat{a_t}\cdot\hat{a_r}^*|^2$ represents the polarization conversion loss in converting the incident wave into RF power available at antenna port. The antenna gain is proportional to the effective aperture size of antenna,

$$G = \frac{4\pi}{\lambda^2}A_{eff} = \frac{4\pi}{\lambda^2}\eta_{ap}A_{phy} \tag{2.8}$$

where A_{eff} is the effective aperture size and the A_{phy} is the effective physical size. η_{ap} is the aperture efficiency of the antenna. The aperture effieicny relates the physical aperture are to the effecive aperture area and can be treated as constant for a given array element geometry.

$$\begin{aligned}\eta_{far} = \frac{P_{rx}}{P_{tx}} &= \frac{A_{eff,tx}A_{eff,rx}}{c^2}(\frac{f}{R})^2 \\ &= \eta_{ap,tx}\eta_{ap,rx}\frac{A_{phy,tx}A_{phy,rx}}{c^2}(\frac{f}{R})^2\end{aligned} \tag{2.9}$$

After rearranging the Friis transmission equation (Eq.(2.7), a more intuitive expression can be expressed regarding physical size and operation frequency in (2.9), assuming no polarization loss and negligible mismatch loss. This expression gives the design guideline of the phased array antenna. Given the range of propagation and the limitation of the array size, the higher frequency of operation leads to higher transmission efficiency. This conclusion contradicts our normal intuition in link budget calculation of wireless communication that the lower frequency gives lower path loss. The reason for this contradictory conclusion is that, give the fixed physical size of the array antenna, the number of antenna elements increased as with the decrease of wavelength instead of using the single antenna as in wireless

communication. Besides, for the use of consumer electronics, the receiver of wireless power is mobile and has to be as small as possible so the demand of smaller size receive array can be compensated by the larger size of transmit array from the observation of this equation.

However, the Friis equation is defined in the region of the far field that is given by $R > \frac{2D^2}{\lambda}$, where D is the dimension of array aperture. It implies that, in most cases, the array antenna operates in the Fresnel near field region and incident wave is spherical wave instead of plane wave, if we attempt to achieve the higher transmission efficiency by increasing the frequency of operation and the larger size of transmit array. Another expression for estimating the transmission efficiency in the intermediate near-field region is given in [79] and [9]. This expression is more accurate when the aperture size of transmit array is very large and more comparisons can be found in the book [79].

$$\eta_{near} = \frac{P_{rx}}{P_{tx}} = 1 - e^{-\tau^2} \tag{2.10}$$

where $\tau = \eta_{far}$ is equal to the Friis equation.

2.2.3 Transmission Efficiency based on Channel Transfer Function

This subsection presents a general model in terms of the channel transfer equation and mutual impedance matrix. The microstrip patch antenna is taken as an example in our formulation and simulation, which is the most popular planar antenna because it is relatively inexpensive to manufacture and integrate with printed circuit design. In Fig. 2.3, the input voltage at the port of n_{th} patch antenna is denoted by $V_{in,n}$ and the voltage at the radiating slot of this patch is the transmitted wave $V_n = (1 - \Gamma_n)V_{in,n}$, where $\Gamma_n = (Z_A - Z_0)/(Z_A + Z_0)$.

From the model in [12] , the electric field, at any point $\vec{r}$, given by the n_{th} patch antenna of transmit array at $\vec{r}_n$, is expressed in terms of the locations, dimensions of patch and the voltage at radiating slots as Fig.2.2. The microstrip antenna is a rectangular patch with width of W and length of L and the substrate thickness is h.

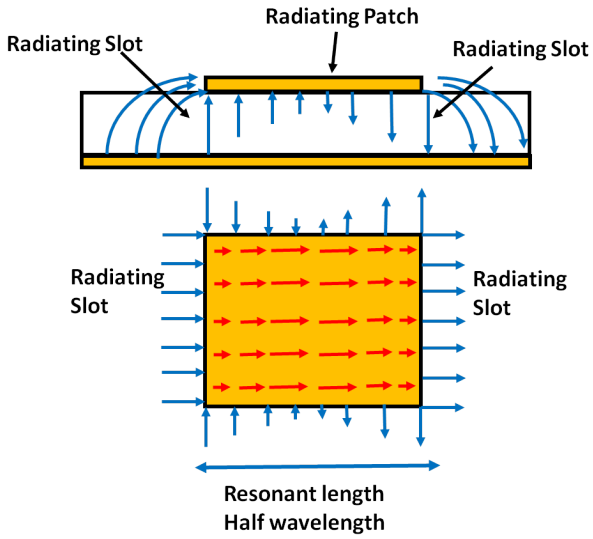

Figure 2.2: Radiation of the patch antenna in TM_{10} mode: blue arrow is electric field and red arrow is current flow

$$\vec{E}(\vec{r},\vec{r}_n) = \frac{-jV_n k_0 W e^{-jk_0 R}}{\pi R} F(\theta,\phi) \tag{2.11}$$

$$\vec{E}(\vec{r},\vec{r}_n) = \kappa V_n G(R) F(\vec{\theta},\phi) \tag{2.12}$$

where $R = |\vec{r} - \vec{r}_n|$, $\kappa = (-jk_0 W)/\pi$ and $G = e^{-jk_0 R}/R$.

θ and ϕ are the spherical angles corresponding to the location $\vec{r}_n$. In the directivity pattern$\vec{F}(\theta,\phi)$, the origin of spherical angles for different patch elements should be the geometric center of the corresponding patch. However, since we have the far field approximation $\theta_1 \cong ... \cong \theta_M \cong \theta$ and $\phi_1 \cong ... \cong \phi_M \cong \phi$, the values of θ and ϕ corresponding to every transmit element can be approximated by the angle from the phase center of array to the observation point.

The directivity pattern $\vec{F}(\theta,\phi)$ has two orthogonal components $\vec{F_\theta}$ and $\vec{F_\phi}$.

$$\begin{aligned}
&\vec{F}(\theta,\phi) = \hat{\theta}F_\theta + \hat{\phi}F_\phi \\
&\vec{F}(\theta,\phi) = [\hat{\phi}cos\theta sin\phi - \hat{\theta}cos\phi]cos(khcos\theta) \\
&\qquad \frac{sin(\frac{k_0 W}{2} sin\theta sin\phi)}{\frac{k_0 W}{2} sin\theta sin\phi} cos(\frac{k_0 L}{2} sin\theta cos\phi)
\end{aligned} \tag{2.13}$$

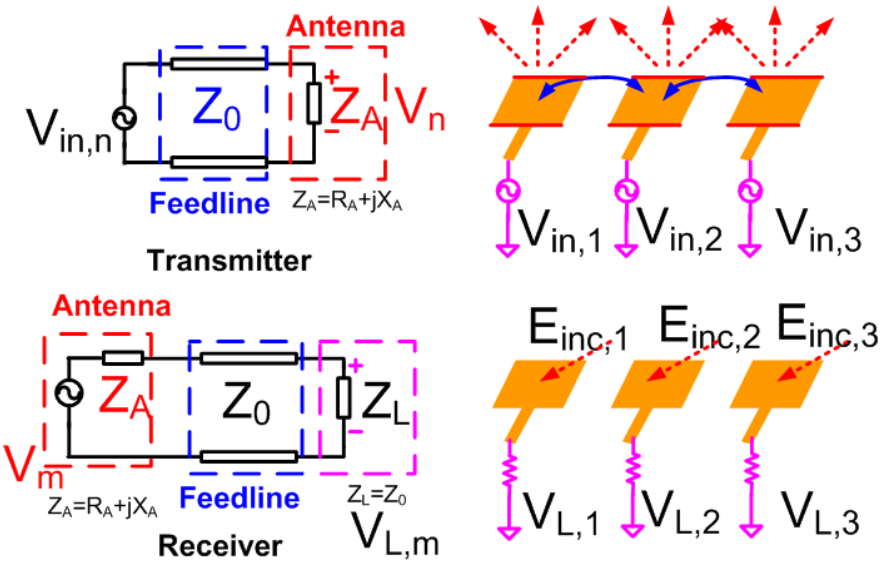

Figure 2.3: Transmit and receive patch antenna array: $E_{inc,n}$ is the incident electric field onto the n_{th} receive antenna elements; $V_{in,n}$ is the input voltage at the port of n_{th} transmit antenna; Z_A is the impedance of transmit/receive antenna; $V_{L,n}$ is the available voltage at the load of receive antenna; Z_L is the load impedance of the receive antenna.

The electric field in Eq.(2.12) can be constructed coherently in space to cancel out the power flow in undesirable direction. Since the electric field is governed by the law of linear superposition, the incident electric field at the m_{th} receive patch antenna ($\vec{r}_m$) is denoted by the sum of electric fields due to input voltage at all M transmit elements.

$$\vec{E}_{inc}(\vec{r}_m) = \sum_{n=1}^{N} \kappa V_n G(|\vec{r}_m - \vec{r}_n|)\vec{F}(\theta,\phi) \tag{2.14}$$

By introducing the vector effective length $\vec{L}_{eff}(\theta_m,\phi_m)$ [70], the induced voltage at the m_{th} receive element is simply the dot product between incident field and effective length.

$$\begin{aligned} V_m &= \vec{E}_{inc}(\vec{r}_m)\cdot\vec{L}_{eff}(\theta_m,\phi_m) \\ &\approx \sum_{n=1}^{N} \kappa V_n G(|\vec{r}_m - \vec{r}_n|)[\vec{F}(\theta,\phi)\cdot\vec{L}_{eff}(\theta',\phi')] \end{aligned} \tag{2.15}$$

It is noted that, in the far field approximation, the angles θ_m and ϕ_m can be referred to the geometric center of receive array and the effective length of all the receive elements are approximately equal from the equal incident angles $\theta^{'}$ and $\phi^{'}$. In addition, since there is no widely-accepted theory to calculate the exact efficiency of power absorption at receive antennas [71], the effect of scattering or reradiation is not discussed in this chapter and its effect is simply included into the polarization mismatch of incident field and the impedance mismatch at the load impedance. Hence, the transfer function from the input port to output load, which is actually the S parameters in numerical simulations, can be formulated as follows.

$$\begin{aligned} H_{mn} &= \frac{V_{out,m}}{V_{in,n}}|_{V_{in,j}=0 for j\neq n} \\ &= \kappa(1-\Gamma_n)G(|\vec{r}_m - \vec{r}_n|) \\ &[\vec{F}(\theta_n,\phi_n)\cdot\vec{L}_{eff}(\theta_m,\phi_m)]\frac{Z_0}{Z_0+Z_A} \end{aligned} \tag{2.16}$$

At transmitter side, $(1-\Gamma_n)$ denotes the reflection at the input port of transmit antenna. At receiver side, $[\vec{F}(\theta_n,\phi_n)\cdot\vec{L}_{eff}(\theta_m,\phi_m)]$is the polarization factor while $Z_0/(Z_0+Z_A)$ is mismatch factor [70].

$G(|\vec{r}_m-\vec{r}_n|)$ is the Green's function, which represents the wave propagation from the transmit element to receive element. In free space, it can be simply taken as its simplest form $G = e^{-jk_0R}/R$ while, in complex medium, this function has to be modified to a different expression of Green's function accordingly [44].

The total RF power deliverable to the load can be added up over all the receive elements

incoherently.

$$\begin{aligned} P_{out} &= \sum_{m=1}^{M} \frac{V_{out,m} V_{out,m}^*}{2Z_L} \\ &= \frac{1}{2Z_L} \sum_{m=1}^{M} \sum_{n=1}^{N} (V_{in,n} H_{mn})(V_{in,n} H_{mn})^* \\ &= \frac{1}{2Z_L} \mathbf{V}_{in} \mathbf{H} \mathbf{H}^H \mathbf{V}_{in}^H \end{aligned} \tag{2.17}$$

The total input power can also be computed at circuit level in terms of mutual impedance matrix in (2.1) and reflection coefficient $P_{in} = P_{rad}/(1 - |\Gamma|^2)$. Hence, the overall RF transmission efficiency, which includes the efficiencies due to transmit antenna, receive antenna and wave propagation in medium, is computed as follows ($\eta = E_2 E_3 E_4$).

$$\begin{aligned} \eta = \frac{P_{out}}{P_{in}} &= \frac{(1 - |\Gamma|^2)}{Z_L} \frac{\mathbf{V}_{in} \mathbf{H} \mathbf{H}^H \mathbf{V}_{in}^H}{\mathbf{V}_{in} \Re\{\mathbf{Z}^{-1}\} \mathbf{V}_{in}^H} \\ &\sim \frac{\mathbf{V}_{in} \mathbf{H} \mathbf{H}^H \mathbf{V}_{in}^H}{\mathbf{V}_{in} \Re\{\mathbf{Z}_A^{-1}\} \mathbf{V}_{in}^H} \end{aligned} \tag{2.18}$$

2.2.4 Experiment Study of Indoor MPT

Since the accuracy of the aforementioned models is to be validated, a wireless power transmission experiment is carried out in our lab environment with two arrays placed face-to-face with each other. To obtain the insight into the MPT in such a scenario, the complete MPT system is built with the detailed analysis of link budget.

Firstly, the indoor experiment is carried out with two standard gain horn antennas with the realized gain of 14 dB and the measured S_{21} (dembedded to the plane of antenna port) is tabulated as follows when the two antennas are facing with each other accurately. Moreover, it it noted that the dimension of the horn antenna is approximately $D = 0.2m$ so the far field condition is $R > \frac{2D^2}{\lambda} \approx 1.54m$ while the near field condition is $R > 0.62\sqrt{\frac{D^3}{\lambda}} \approx 0.24m$. This implies that the system operates in the Fresnel near field region, where the radiation pattern or spatial distribution of electromagnetic field varies significantly with the distance. From the Table 2.1, it is found that the far field equation gives a closer estimation of transmission

Table 2.1: Measurement with horn antenna versus distance. The S_{21} reflects the power ratio at the network analyzer so the cable loss is extracted to deembed the reference to the antenna ports. The path loss is computed from Friis equation with unity antenna gain assuming the transmision with isotropic radiator.

Distance	0.6m	1.2m	1.8m	2.4m	3m
Deembeded S_{21}	-22dB	-27dB	-30dB	-31dB	-32dB
Path Loss	-50dB	-55dB	-58dB	-59dB	-60dB
Near Field Equation (2.10)	-30dB	-42dB	-49dB	-54dB	-58dB
Far Field Equation (2.9)	-15dB	-21dB	-25dB	-27dB	-29dB

efficienc while the estimation error of near field equation is much larger. The reason for this is that the receiver is closer to the far field boundary than near field boundary. The general rule of determining which equation is stated in [79] as that the near field efficiency is more accurate when the value of τ is larger than 1.

Next, the prototype of MPT system including both transmitter and receiver is also built to study the contribution of real system losses. As shown in Fig.2.4, the full system includes the signal generator, power divider, transmit and receive antenna array, RF rectifier with load resistor and high power amplifier.

The transmit and receive antenna array are the same series-fed microstrip antenna array, which has 14 elements connected in series governed by the Chebyshev distribution of width tapering and operates in the resonant mode. In the other dimension, ten input ports are connected in parallel with the spacing of half free space wavelength. At the transmitter side, the ten parallel input ports are fed with a 10-way broadband power divider, which is made up of the cascaded two-way Wilkinson power dividers and three-way dividers. Therefore, the ten ports of power divider are weighted rather than equally distributed. This feeding network can reduce the sidelobe level (SLL) to some extent while achieving broadband power combining at the cost of increased insertion loss. The antenna array and the power divider are fabricated on two separate FR-4 printed circuit board (PCB). The antenna array gives

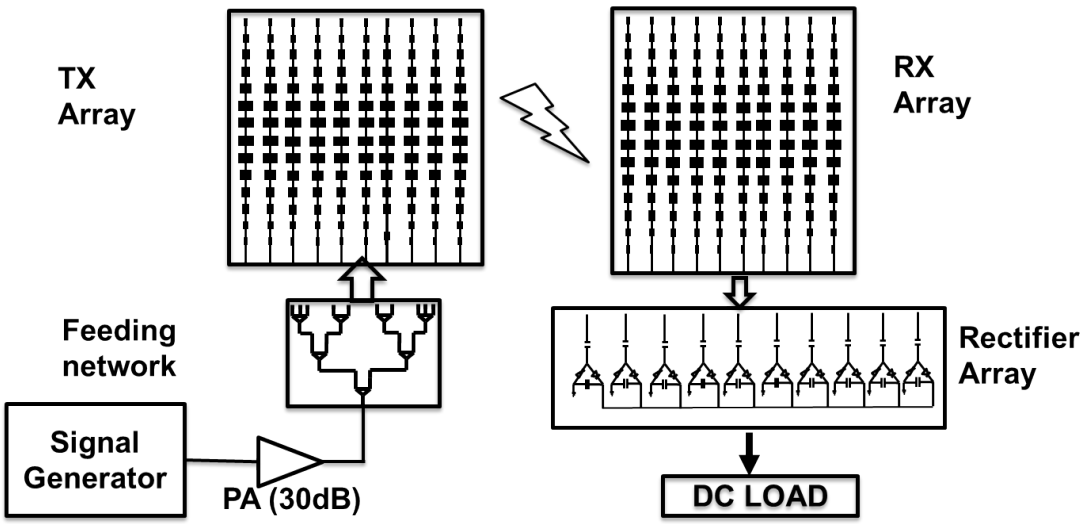

Figure 2.4: Experimental configuration of the full MPT system

a simulated realized gain of 25 dB, and the broadband power divider gives a measured -6.96 dB insertion loss of power division. Therefore, the total array with the power divider at the transmitter gives a realized gain of approximately 19 dB. The power amplifier is a broadband high power amplifier by Mini-Circuits with typical power added efficiency (PAE) of 30% at 5.8 GHz and can output up to 1 Watt RF signal without distortion.

At the receiver side, the RF rectifier array is implemented with the single stage charge pump topology and converts the RF signal to DC power. The diode in the rectifier is the HSMS-286x surface mount a Schottky detector diode by Avago Technology, which gives the low series resistance of 6Ω. The single rectifier unit achieves up to 73% conversion efficiency with this low loss diode. The rectifier array employs the hybrid of series and parallel power combining at DC and is optimized to 20% to 40% conversion efficiency with the DC load of 150Ω and the input signal of 0 dBm sinusoidal wave at 5.8GHz, which is the case in our measurement. It is noted that the efficiency of rectifier varies with the input power level, input signal frequency, the way of DC power combining and DC load present to the rectifier, so the conversion efficiency keeps changing with the experimental condition.

The full system measurement is carried out with the separation distance of 3 meters between the transmitter and receiver. To find out the contribution of the system loss, each component of the whole system must be measured one by one and, when the signal generator outputs the RF power of 0 dBm, the link budget can be estimated as in Fig.2.5. To analyze the contribution of low efficiency, the total system losses are dissected in the view of a pie chart as shown in Fig.2.6.

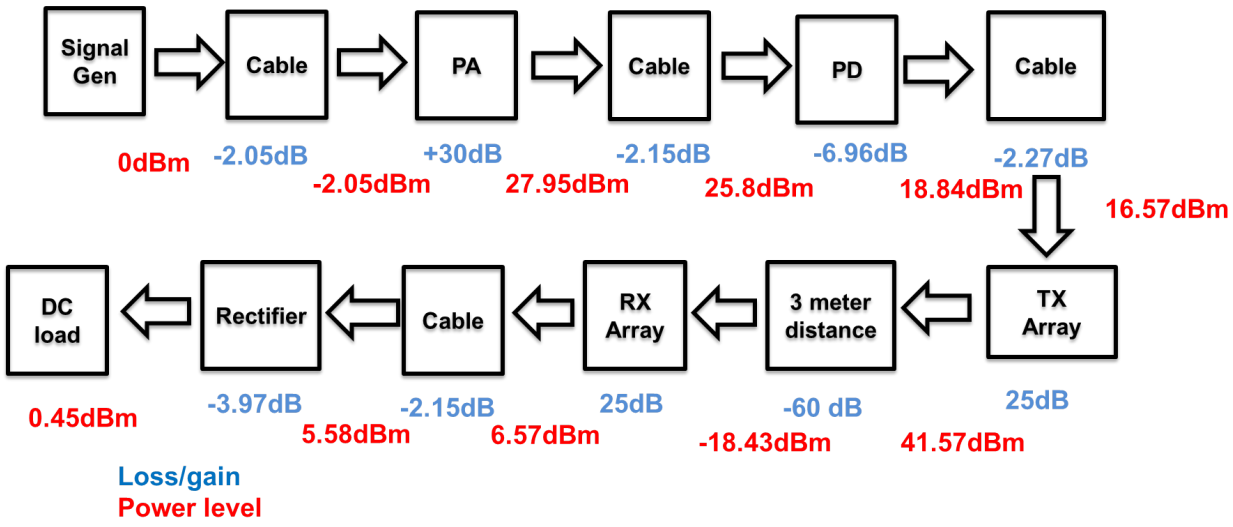

Figure 2.5: The link budget of prototype system. The PAE of power amplifier is taken as 30% as given by the device specification while the conversion efficiency of rectifier array is taken as 40%. The distance between transmitter and receiver it taken as 3 meter. The path loss excluding antenna gain is estimated using the measurement in Table 2.1 and the radiation into wave proagation medium is labeld as radiation loss.

From the analysis of system losses, it can be found that, because the total DC power at the transmitter is almost equal to DC power consumption of power amplifier, the upper limit of power loss is set by the PAE of the power amplifier (PA) and the amount of this loss is fixed. Though the second and third largest power loss are contributed by the feeding network and RF cable as Fig.2.6, these losses can be effectively reduced using the spatial power combining technique.

However, in spite of the high-efficiency circuit design, the radiation loss will dominate

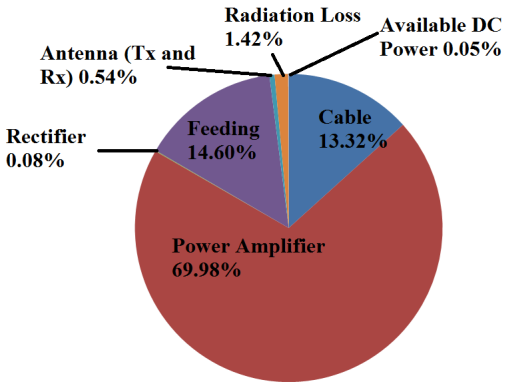

Figure 2.6: Contribution of system losses: The measured output DC power is consistent with the estimated link budget in Fig.2.5.The total DC to DC transmission efficiency is computed as 0.068%.

the system loss and is hard to suppress. The degradation of efficiency is more serious when the LOS propagation is not available. When the LOS channel is blocked in the experiment, the loss of the fixed beam array increases by more than 20 dB according to our experiment. The only possible solution to high transmission efficiency is adaptive beamforming array. Techniques for the adaptive array will be discussed in the following Section 2.3.

2.3 Reivew of Optimal Beamforming Techniques

The antenna beamforming is achieved through the coherent operation of antenna elements, so the excitation weight of each element determines the performance of beamforming.

2.3.1 Array Factor Optimization

In traditional beamforming based on AF synthesis, the antenna elements are assumed to have the same radiation pattern and accurately positioned. The steering vector $\mathbf{v}_s = [e^{ik(ux_n+vy_n)}]$ is used to yield the AF $F(u,v) = \sum_{n=1}^{N} w_n e^{ik(ux_n+vy_n)}$,where (u,v) identifying the angular region . Since the power of AF is proportional to the spatial distribution of the radiated power, BCE is expressed in terms of the power of AF and a closed form expression of BCE

is derived for the planar array case by Oliveri et.al [68].

$$BCE = \frac{\int\limits_{\Psi} \sum_{n=1}^{N} w_n e^{ik(ux_n+vy_n)}}{\int\limits_{\Omega} \sum_{n=1}^{N} w_n e^{ik(ux_n+vy_n)}} = \frac{\mathbf{w}^H \mathbf{A} \mathbf{w}}{\mathbf{w}^H \mathbf{B} \mathbf{w}} \tag{2.19}$$

where $B_{mn} = 4\pi sinc(k\sqrt{(x_m - x_n)^2 + (y_m - y_n)^2})$ and $A_{mn} = 4\pi u_0 v_0$
$sinc(k(x_m - x_n))sinc(k(y_m - y_n))$

This approximation greatly reduces the computation time at the cost of accuracy. However, for other structures and spacings of array, the closed form expression is not available and the numerical integral of powers has to be performed, which may take a long time to approach an optimal solution. In reality, the radiation pattern of array element is never the same due to mutual coupling, edge effect and manufacturing process. More importantly, this technique is not valid for power optimization if the array is not regular shape with known position [68].

2.3.2 Retrodirective Array/Phase Conjugate Array

Retrodirective Array is the array to reflect the incident plane wave toward the source direction without any prior information on the source location. The retrodirective array works in the following way: the receive array/interrogate antenna out a probing signal and then transmit array retransmits the amplified signal towards receiver by taking phase conjugate of the observed probing signal. Since the phase conjugating functionality can be implemented at RF frequency with hardware, its popularity arises from the automatic beam steering without any computational algorithm (i.e. digital signal processing hardware). Although this technique is also adaptive to the propagation channel, it only works for a fixed frequency. The array calibration becomes problematic, depending on the hardware design.

2.3.3 Adaptive Array Digital Beamforming

Digital beamforming is more powerful and flexible than conventional phased array at the expense of hardware complexity and cost. However, if the estimation of channel characteris-

tics is enabled by the additional receive antennas, the adaptive signal processing results in a more powerful beamforming transmitter and flexible beamforming formulation regardless of array shape and position. Digital beamforming based on the channel estimation is also an important technique to enhance the signal-to-interference ratio (SIR), signal-to-noise ratio (SNR) and the intersymbol interference (ISI) in the in MISO or MIMO communication.

The time reversal(TR) technique has been studied extensively in wireless communication by many researchers [64], as this scheme can improve SNR greatly in multipath and the rich scattering environment. The receivers send a probing signal to a transmitter for channel estimation, and the transmitters convolve the time-reversed channel impulse response $h(-t)$ with the transmitted signal $s(t)$. The received signal will be equal to the convolution between the transmitted signal $s(t)$ and the autocorrelation of the channel impulse response. Eq.(2.20) indicates that the energy will be spatially focused at the target receiver in any environment. When the receiver has multiple antennas, this TR beamforming technique is not valid for energy focusing.

$$y(t) = s(t) * h(-t) * h(t) = s(t) * R(t) \tag{2.20}$$

The eigen-beamforming is an optimal scheme for maximizing the average SNR [107] in the narrowband MIMO. Nevertheless, the optimization of SNR happens at the output of matched filter instead of the summed power at the receiver. Besides, it is noted that the maximization is implemented with the coding scheme, which results in the spectrum spread. For this reason, this technique is not applicable for adaptive beamforming in MPT, which requires the continuous wave transmission.

$$SNR = \frac{E\{\mathbf{h}^H\mathbf{C}^H\mathbf{Ch}s\}}{E\{\mathbf{h}^H\mathbf{C}^H\mathbf{nn}^H\mathbf{Ch}\}} \tag{2.21}$$

where $\mathbf{h}$ is the matrix of channel impulse response in time domain and $\mathbf{C}$ is the coding scheme of eigen-beamforming. $\mathbf{n}$ is the Gaussian noise and s is the baseband signal carrying information.

Furthermore, the time revesal scheme is analyzed using the model of Green's function in

the frequency domain [40] [45] ,as the time reversed signal is equivalent to the complex conjugate in frequency domain. The paper [40] and [45] demonstrate that the communication efficiency can be improved with the proposed beamforming scheme in theory and in experiment, respectively. To our knowledge, the specific application of adaptive beamforming for WPT has not been reported yet.

2.4 Time Reversal Eigenmode Beamforming

The classic array synthesis technique is developed based on the model of AF with the assumption of equal element pattern. As is widely known by antenna designer, the mutual coupling leads to the unequal pattern, especially for the edge element. For the array with the unequal element and arbitrary location, the AF is no longer valid, and the adaptive array processing has to be employed for the array synthesis using the knowledge of probing channel characteristics. However, the previous studies of adaptive beamforming are developed for improving the signal-to-noise (SNR) ratio or channel capacity based on MIMO wireless communication and no discussions on how to devise an adaptive algorithm for MPT. This section presents a modified algorithm for MPT based on the time reversal signal processing techniques. Besides, it will also be proved as a new optimal array synthesis method without the prior knowledge of element spacing and positions.

2.4.1 Pseudo Transmission Efficiency

To implement the adaptive optimization of transmission efficiency, we propose the pseudo transmission efficiency(PTE) as an alternative optimization goal. PTE is the ratio between the total RF power available at the receiving array, and the incoherent sum of the input power over all transmit elements.

The incoherent sum of radiated power takes the sum of input power at each radiator independently and is only physical for the special case that the mutual impedance matrix is a diagonal matrix ($P_{sum,in} \neq P_{in}$). However, the incoherent power is used in communication society for evaluation of power in wireless communication by neglecting the mutual coupling

effect. Similarly, the incoherent sum of radiated power is related to input power ($P_{sum,rad} = (1 - |\Gamma|^2)P_{sum,in}$).

$$P_{sum,rad} = \frac{\mathbf{V}^H\mathbf{V}}{2R_{rad}} = \frac{1}{2}\mathbf{V}^H\Re\{diag[\mathbf{Z}_A^{-1}]\}\mathbf{V} \tag{2.22}$$

$$PTE \triangleq \frac{P_{out}}{P_{sum,in}} \tag{2.23}$$

PTE is not a physical efficiency, but the difference between PTE and η (Eq.(2.18) is negligible if the real part of mutual coupling impedance terms are sufficiently small. When the adjacent antenna elements are weakly coupled to each other, the transmit channels are uncorrelated with each other. The correlation between transmits channels is expected to be low in both MPT and MIMO communication. While the envelope correlation coefficient(ECC) is an indicator of the MIMO antenna design, the independence of MPT array is reflected by the ratio between the radiated power and the coupled power dissipation in the following Eq.(2.24). It is noted that this correlation power factor is related to the complex excitations of the array elements and the power ratio R increases as with the improved isolation between adjacent elements.

$$R(\mathbf{V}_{in}) \triangleq \frac{\sum_{i=1}^{N} v_i\Re\{y_{ii}\}v_i^*}{\sum_{j=1}^{N}\sum_{i=1,i\neq j}^{N} v_i\Re\{y_{ij}\}v_j^*} \tag{2.24}$$

To verify this assumption quantitatively, a simple 2 x 2 rectangular array is simulated in Ansys HFSS and the expored Y parameter is used to compute the correlation power factor with several complex excitation combinations. These five excitation vectors have the uniform magnitude but random linear phase progression. Fig.2.7 shows that the exact value of correlation power factor is dependent on the excitation vector but the average increases with the array element spacing, which is equivalent to the isolation between two elements. The improvement of mutual coupling can also be implemented by the techniques of enhancing ECC in MIMO antenna design.

In Fig.2.8, the error between incoherent power sum ($P_{sum,in}$) and physical input power(P_{in}) is defined as $Error \triangleq |(P_{sum,in} - P_{in})/P_{sum,in}|$ and the error is plotted for different excitations

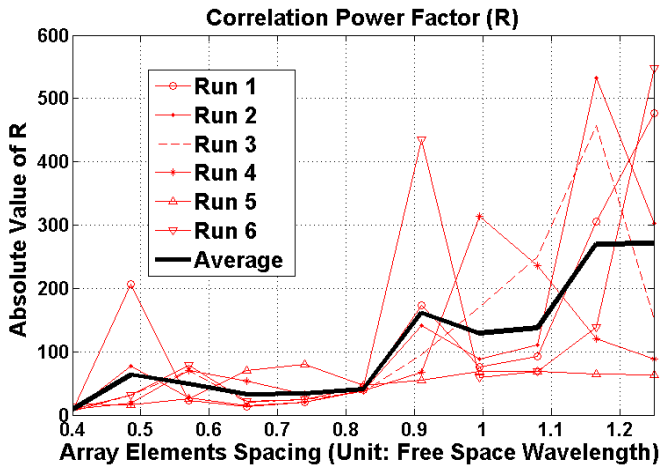

Figure 2.7: Correlation power factor (R): the average correlation power factor increases as with the increase of element spacing.

as in Fig.2.7. The average of the five excitations shows that the average error is well below 5% when the array spacing is greater than the half free space wavelength. In summary, the plots in Fig.2.7 and Fig.2.8 quantitatively justify why the PTE gives a good estimation of transmission efficiency for weakly coupled array.

2.4.2 Transmission Efficiency Optimization

Since the correlated power is sufficiently low in most array setup, this chapter will discuss the optimization of PTE instead of either η or BCE. If the PTE is rearranged, Eq.(2.23) can be simplified as in (2.25).

$$\begin{aligned} PTE = \frac{P_{out}}{P_{sum,in}} &= \frac{(1-|\Gamma|^2)}{Z_L}\frac{\mathbf{V}_{in}\mathbf{H}\mathbf{H}^H\mathbf{V}_{in}^H}{\Re\{Z_{rad}^{-1}\}\mathbf{V}_{in}\mathbf{V}_{in}^H} \\ &\sim \frac{\mathbf{V}_{in}\mathbf{H}\mathbf{H}^H\mathbf{V}_{in}^H}{\mathbf{V}_{in}\Re\{diag(\mathbf{Z}_A)^{-1}\}\mathbf{V}_{in}^H} \\ &\sim \frac{\mathbf{V}_{in}\mathbf{H}\mathbf{H}^H\mathbf{V}_{in}^H}{\mathbf{V}_{in}\mathbf{V}_{in}^H} \end{aligned} \tag{2.25}$$

From Eq.(2.18) and Eq.(2.25), it is clear that the ultimate goal of achieving optimal transmission efficiency is to solve the eigenvalue problem $\mathbf{R}_Z\mathbf{P}\mathbf{V}_{\mathbf{in}} = \lambda\mathbf{V}_{\mathbf{in}}$, where $\mathbf{P} = \mathbf{H}^H\mathbf{H}$ and

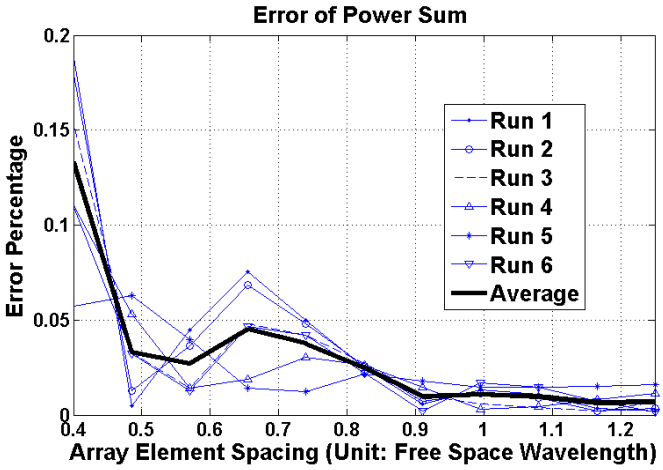

Figure 2.8: Error percentage of incoherent sum: the average error decreases as with the increase of element spacing

$\mathbf{R}_Z = \Re\{\mathbf{Z}\}$. $\mathbf{V_{in}}$ is the input voltage, which also corresponds to the eigenvector of this problem. This is a Rayleigh Quotient and the eigenvalues of $\mathbf{R}_Z\mathbf{P}$ give the possible range of the transmission efficiency η. From Min-Max Theorem, it is known that the dominant eigenvector (the eigenvector corresponding to the largest eigenvalue) maximizes the transmission efficiency η.

$$\mathbf{V}_{in,opt} = arg[\max_{\mathbf{V}_{in}} \frac{\mathbf{V}_{in}\mathbf{H}\mathbf{H}^H\mathbf{V}_{in}^H}{\mathbf{V}_{in}\Re\{\mathbf{Z}^{-1}\}\mathbf{V}_{in}^H}] \tag{2.26}$$

However, the mutual impedance matrix can only be estimated from measurements but the measurement is difficult if the number of array elements are very large so finding the matrices in this eigenvalue problem is a difficult task.

$$\mathbf{V}_{in,opt} = arg[\max_{\mathbf{V}_{in}} \frac{\mathbf{V}_{in}\mathbf{H}\mathbf{H}^H\mathbf{V}_{in}^H}{\mathbf{V}_{in}\mathbf{V}_{in}^H}] \tag{2.27}$$

Therefore, as discussed above, we may think of optimizing the PTE as an alternative goal because it can be computed from the signal levels observed at the input ports. This method is validated in Fig.2.8 as the error between η and PTE is expected to be negligibly small for the array with large spacing. In this way, another eigenvalue problem is formulated

$\mathbf{PV}_{in} = \lambda \mathbf{V}_{in}$. The Min-Max Theorem is also applicable for this as Eq.(2.27). In most cases, the maximization of PTE yields the maximal values of transmission efficiencies. Hence, the next challenge is how to devise an algorithm to approach this optimal eigenvector excitation.

2.4.3 Time Reversal Eigenmode Beamforming

Time reversal signal processing technique is derived from the research on acoustic focusing effect with time reversal mirror(TRM) by M.Fink [27, 28]. This principle focuses the energy thanks to the reciprocity of wave equation: the TR (using a negative time) of the wave functions' solution is also a solution to this equation as long as the media is slowly varying, reciprocal and linear. When the TRM emits the plane wave towards a passive scatterer and observes the thescattered signal, the emitted energy by TRM can be focused to this scatterer by retransmitting a time reversed copy of the observed signal. If the process is iterated, the energy becomes more and more focused on this passive target. This technique has been developed into applications including wireless communication and radar imaging in cluttered and complex medium with computational iterative process [44, 45, 73, 100].

If the channel transfer function between transmit and receiving antenna can be measured in real time, the iterated time reversal process can be performed with a simple eigendecomposition process as discussed in [44]. Thus, the proposed method requires the probing of channel transfer matrix and digital beamforming architecture. The RF hardware of MPT system is similar to the massive MIMO communication as in Fig.2.9 [87]. In such a power transmission system, the communication module is integrated with the power delivery module and used to probe the channel characteristics as MIMO communication. Given a transmit array of N elements and a receive array of M elements, the process of the proposed technique is stated as follows.

- **Measurement of transfer matrix H(M-by-N)**

  The probing signal is an impulse waveform $s_n(t)$ spanning over the power transmission band and sent from each receive array elements one by one. The observed signal is

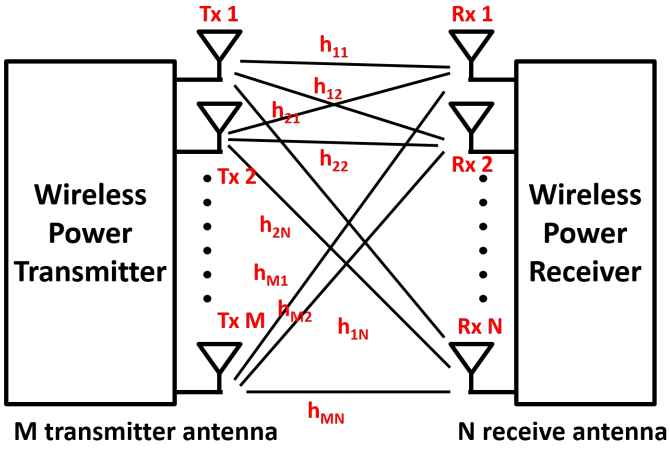

Figure 2.9: Time reversal eigenmode beamforming system

recorded simultaneously at all the transmit elements and the recorded transient signal $y_m(t)$ is tranformed to frequency domain $Y_m(\omega)$ through Fourier Transform. Then the recorded signal is normalized to the probing signal as $h_{mn}(\omega) = Y_m(\omega)/S_n(\omega)$. $h_{mn}(\omega)$ is defined as the channel transfer function in frequency domain between the n_{th} element of transmit array and m_{th} element of receive array.

- **Construction of transfer power matrix P (N-by-N)**

  The transfer functions h_{mn} at the frequency of ω are rearranged into the matrix format as $\mathbf{H}(\omega)$.

$$\mathbf{H}(\omega) = \begin{bmatrix} h_{11} & h_{12} & h_{13} & \dots & h_{1N} \\ h_{21} & h_{22} & h_{23} & \dots & h_{2N} \\ \vdots & \vdots & \vdots & \ddots & \vdots \\ h_{M1} & h_{M2} & h_{M3} & \dots & h_{MN} \end{bmatrix} \tag{2.28}$$

  The transfer matrix is used for the computation of the transfer power matrix($\mathbf{P}(\omega)$).

$$\mathbf{P}(\omega) = \mathbf{H}(\omega)^H \mathbf{H}(\omega) \tag{2.29}$$

- **Calculation of dominant eigenvectors(corresponding to largest eigenvalue)**

The eigenvector of the power transfer matrix can be found through the numerical eigenvalue decomposition of measured data. As discussed before, the eigenvector that corresponding to the largest eigenvalue leads to the maximization of PTE and will be used for beamforming.

$$\mathbf{PV}_{in,1} = \lambda_1 \mathbf{V}_{in,1} \tag{2.30}$$

- **Power delivery according to dominant eigenvector**

  Each element in the eigenvector $\mathbf{V}_1$ corresponds to the complex excitation of one antenna element. Since, in most cases, the single tone signal is used for wireless power transmission, the sinusoidal wave at the frequency of ω is weighted with the dominant eigenvector as follows.

$$y_m(t) = \mathfrak{F}^{-1}\{v_{1m}(\omega)\} = |v_{1m}(\omega)| sin(\omega t + \angle v_{1m}(\omega)) \tag{2.31}$$

The proposed scheme is implemented with the digital beamforming architecture so the synchronized transmitters synthesize the desired transmit signal $y_m(t)$ with analog-to-digital converter(ADC) and feed into each transmit elements for power beamforming. It is noted that in the real scenario of MPT, the available frequency of power transmission spans over a bandwidth of hundreds of megahertz while only a single carrier frequency is needed. To maximize the transmission efficiency, the eigenvalues of power transfer matrix over the available bandwidth can be compared to find at which frequency the power transmission has lowest propagation loss for the given environment.

The TR eigenmode technique have a drawback that is the susceptibility to interfering source. When there are multiple receivers requesting power transmission, the transmitter has to characterize the propagation channel corresponding to these receivers one by one and determine which frequencies are allocated to these receivers based on the frequency dependent eigenvalues corresponding to the receivers. After haveing determined the complex excitations, the simultaneous power transmission can be implemented by superimposing two signals at the baseband. For example, the m_{th} transmitter directly synthesize the sig-

nal which simultaneous power transmission to two receives as $y_m(t) = |v_{1m}^1(\omega_1)|sin(\omega_1 t + \angle v_{1m}^1(\omega_1) + |v_{1m}^2(\omega_2)|sin(\omega_2 t + \angle v_{1m}^2(\omega_2))$. In this way, the transmitter generates dual beams at two different frequencies pointing towards two receivers.

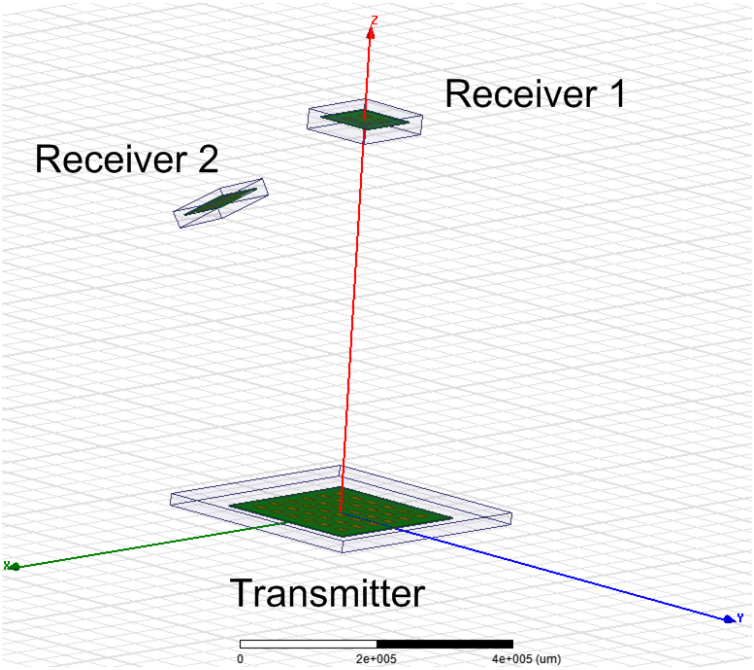

Figure 2.10: Simulation in HFSS-IE. The rectangular patch array antennas are used for both receiver and transmitter. The positions of transmit elements are randomized.

2.5 Numerical Examples

The paper [68] reports that the BCE can be up to 99% by evaluating the power of AF. However, as discussed in Section 2.3 the efficiency derived from AF is not valid when the element pattern is not equal. To compare the effectiveness of different beamforming technique, the numerical simulation in different experiment setup is carried out in Ansys HFSS. The experimental verification of transmission efficiency and channel transfer function is extremely challenging and costly for large-scale array beamforming. In this chapter, the electromagnetic simulation is carried out in HFSS-IE, which is a new module based on Method of

Moment-Integral Equation (MoM-IE) and designed for electrically large simulations.

As shown in Fig. 2.10, microstrip rectangular patch antenna is chosen for investigation as a representative of directive antenna rather than an isotropic radiator. In HFSS, each antenna is placed on the planar Duroid 5870 substrate, so each element has an image due to the ground plane. Its radiation pattern of each antenna is modeled in the previous formulation. The field distribution on the virtual spherical air box is shown in Fig.2.13 to illustrate the power distribution in space. The amplitude and phase of excitation are modified in the postprocessing function of HFSS according to the calculation of our proposed formulation.

Due to the intensive computation cost and limitation of computer memory, the six by six microstrip array is examined to make a comparison with our theoretical model, and the power transfer frequency is taken at 5.8 GHz in HFSS simulation. In the postprocessing, the excitations at each port can be specified with both amplitude and phase and the resultant beam pattern is observed in the far field. The followings are several examples to show the advantages of the proposed scheme with the aid of comparison table and figures.

2.5.1 Arbitrary Array Beamforming in Free Space

In the first example, the beamforming techniques are evaluated in free space in terms of several transmission efficiencies (η, η_{near}, η_{far} and PTE) and spatial distribution of electric field. Four beamforming techniques are chosen for investigation: uniform excitation, phase conjugate(same as a retrodirective array), the proposed method, and AF synthesis technique described in [68].

In the HFSS simulation setup, the transmit array is arbitrarily positioned 6-by-6 antenna array as in Fig. 2.11, the inset of which shows the resultant arbitrary array for beamforming. The random spacing is generated by the normal distribution function of Matlab with the mean of $0.65\lambda_0$. The receive array is a 3-by-3 rectangular array with the spacing of $0.65\lambda_0$ in both x and y-direction. The receiver is located at a distance 0.5m from the center of transmit array and takes the angular area of 0.1×0.1 receive aperture, which is defined as $-\arcsin(0.1/2) \leq \theta \leq \arcsin(0.1/2)$ and $-\arcsin(0.1/2) \leq \phi \leq \arcsin(0.1/2)$)in spherical

coordinate. It is noted that, in this case, the receive array is located in the Fresnel near field region because the distance between receiver and transmitter is between the far field ($\frac{2D^2}{\lambda} \approx 2.18m$) and near field boundary ($0.62\sqrt{\frac{D^3}{\lambda}} \approx 0.31m$). As the exact position of the arbitrary array is not available, the mean spacing is taken for the formulation of AF. Therefore, the degradation of beamforming is expected due to the random phase error.

To compute the beamforming efficiency, the power density can be integrated over angular

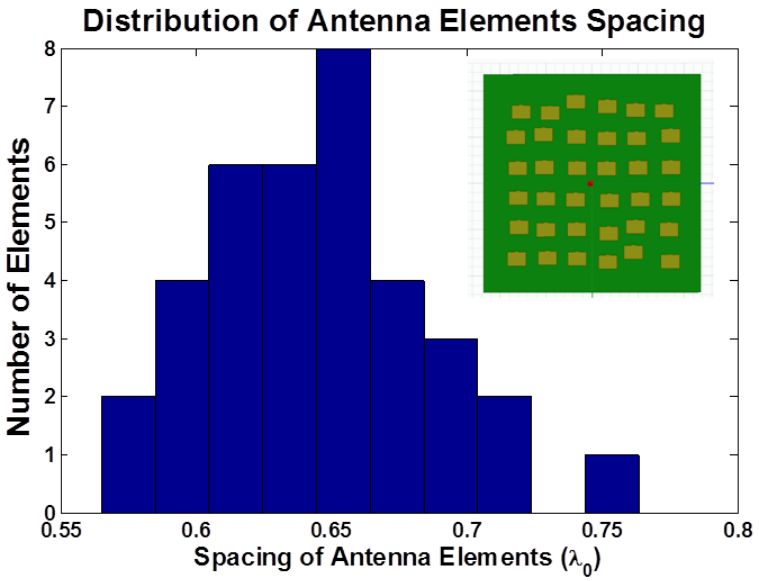

Figure 2.11: Spacing distribution of randomly positioned antenna array: the mean of element spacings is $0.65\lambda_0$

regions(Ψ) to obtain the power focused into the target area. It is noted that, when we compute the spatial power flow, the transmit antenna is simulated without receive antenna with finite element method(FEM) only and enclosed with an upper hemisphere of radius 0.5m. Then the BCE (Eq.(2.5)) is computed to evaluate the ability to shape power beam into angular regions of 0.1×0.1 receive aperture. Besides, the received power and transmitted power are computed from mutual impedance matrix and S-parameters are used to evaluate the transmission efficiency (Eq.(2.6)). For comparison, the incoherent sum of transmitted power is obtained from simulation and used for the computation of PTE as Eq.(2.6).

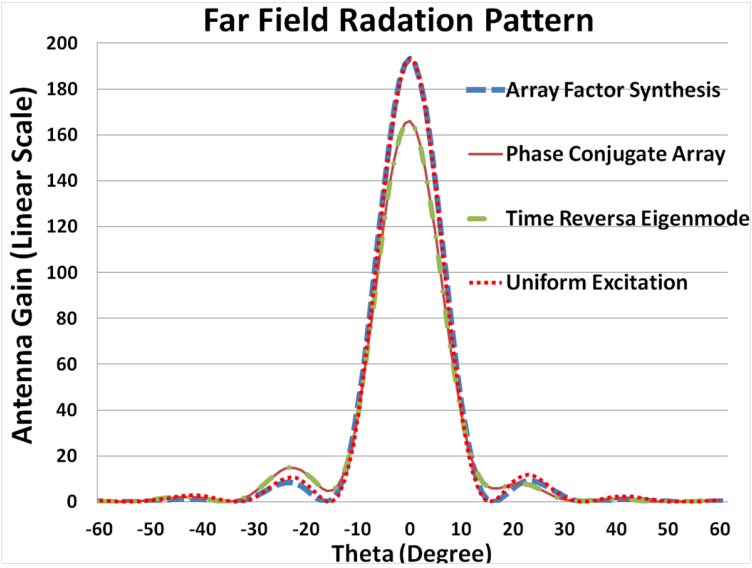

Figure 2.12: Far field radiation pattern of transmit array with different beamforming techniques: max array gain in linear scale can be read from radiation pattern as 165.82, 177.16, 193.35 and 193.41 for the techniques of phase conjugate array, TR eigenmode, uniform excitation, and AF synthesis, respectively.

FEM simulation solves the far field antenna pattern with different complex excitations as in Fig.2.12. The max antenna gains can be read from radiation pattern as 165.82, 177.16, 193.35 and 193.41 (in linear scale) for the techniques of phase conjugate array, TR eigenmode, uniform excitation, and AF synthesis, respectively. These four beamforming techniques gives the effective aperture for the calculation in Eq.(2.9) and Eq.(2.10). The AF synthesis technique and uniform excitation give much higher gain and narrower beamwidth. From the models based on antenna parameters, it implies that these two techniques give higher transmission efficiency with the specific equations. However, the HFSS-IE simulation shows a contradictory results. The AF synthesis and uniform excitation result in the significant leakage of the real power flow (Fig.2.13 if the spatial electric field distribution is plotted on the enclosing hemisphere. The phase conjugate and TR eigenmode techniques have lower far field gain but focus most of the power into the region of receive aperture. For this reason, Table 2.2 shows that the model based estimation (either η_{near} or η_{far}) overestimates the

Table 2.2: Comparison of different optimization techniques for MPT in free space

Beamforming Method	BCE (0.1×0.1)	PTE	η	η_{near}	η_{far}	Gain (linear scale)
Uniform	21.37%	34.18%	18.50%	50.64%	70.59%	193.41
Phase Conjugate	33.05%	45.82%	25.14%	45.47%	60.65%	177.16
TR Eigenmode	33.22%	45.86%	25.22%	45.41%	70.59%	165.82
AF Synthesis	22.64%	36.58%	18.91%	50.63%	60.52%	193.35

efficiency if it is compared with the simulated efficiency. The discrepancy is attributed to the wide main beam at the cost of lower gain so that the adaptive beamforming directs more integrated power into the targeted area.

Futhermore, Table 2.2 shows that either phase conjugate array or time reveral eigenmode technique leads to higher transmission efficiency η especially in the case that the position of antenna elements is not available. It also verifies that the assumption of negligible correlated power dissipation is valid in adaptive beamforming and shows their advantages over the classic array synthesis.

2.5.2 Arbitrary Array Beam Steering

The previous section demonstrates the potential of maximizing transmission efficiency when the receive array at the scan angle of 0 degrees. At this scan angle, the transmit array gives the largest gain and the consequent transmission efficiency over any other beam pointing angles. In our analytical model, although the propagation channel is irrelevant with the location of scan angle, the synthesized beam by adaptive technique has the beam pointing error in some cases as discussed by [105]. Therefore, it is worthy of studying the impact of steering the beam away from the center.

In this subsection, the positions of transmit array elements are the same as last section

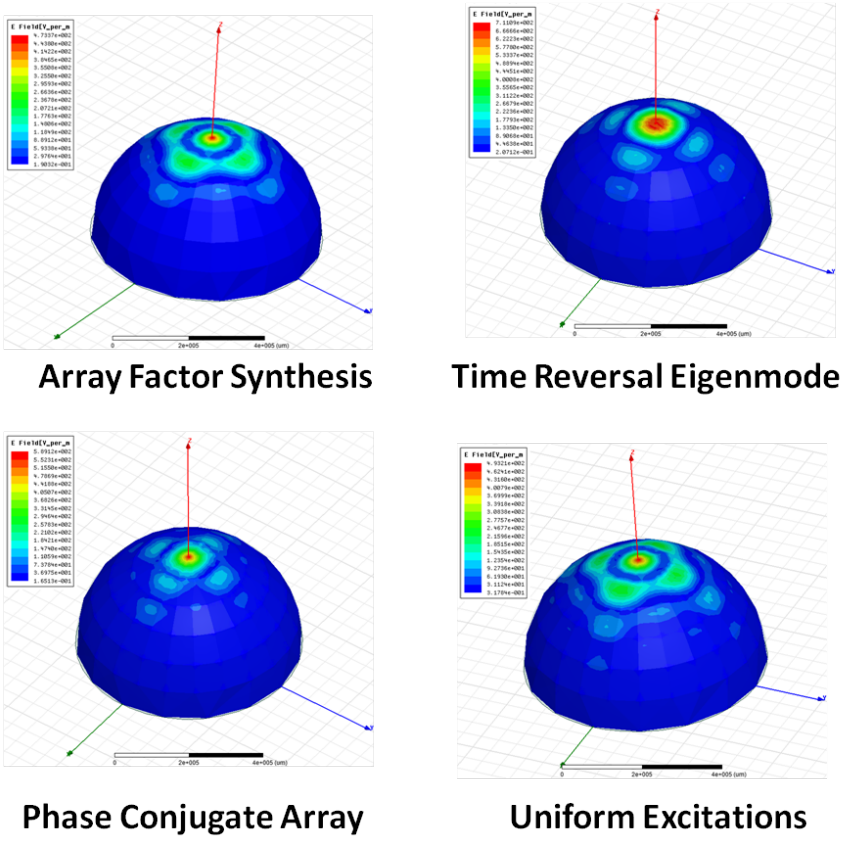

Figure 2.13: Spatial power distribution from different beamforming methods: significant amount of power leakage appears for the AF synthesis and uniform excitations. The enclosing sphere shows the spatial distribution of the real power flow in the region of Frensnel near field region.

while the receive array is rotated along the x-axis to create different receiving angles. Fig.2.14 shows the beam steering towards the receive array based on the time reversal eigenmode technique. The main beam is steered to the angular region without the grating lobe where the receiver is until the scan angle is greater than 30^o. The limited scan angle is due to array spacing of $0.65\lambda_0$. According to the array theory, the maximum scan angle can be computed from the array spacing as $\theta_{max} = arcsin(d/\lambda_0 - 1) = arcsin(0.538) = 32.57^o$. It is noted that, for the scan angle of 45^o, the most of the power flows towards to the direction of receive array with the significant grating lobe at the symmetric location. However, when the scan

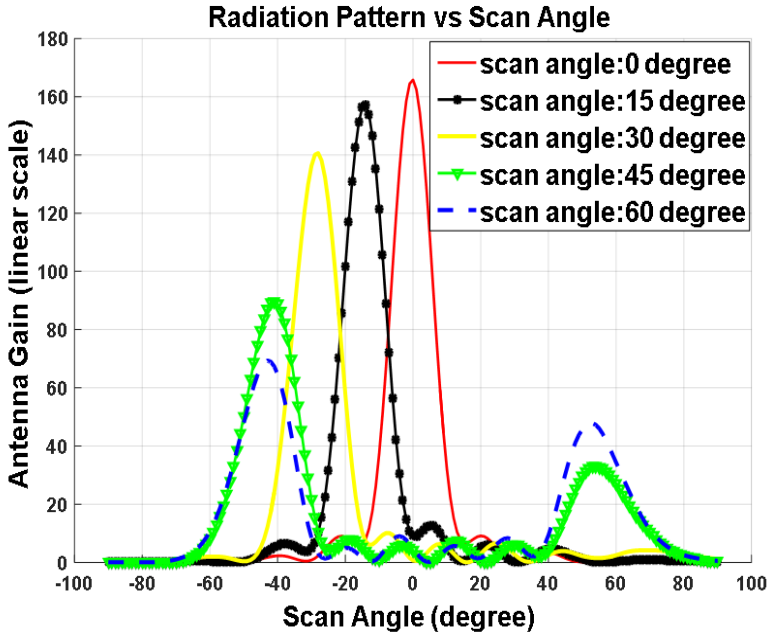

Figure 2.14: Antenna pattern over different scan angles: grating lobe becomes large for the scan angle of $\theta = 45^o$ and 60^o; for the scan angle of 60^o, the main beam cannot be steered to the direction of receive aperture.

angle moves further to 60^o, the main beam cannot be steered to the direction of receiver any more. In fact, this phenomenon is attributed to the scan blindness due to surface wave and can be mitigated by the proper antenna elements design with cavity backing and so on. The beam scanning pattern is given by the adaptive array technique also presents the degradation of array gain, which is called the scan loss. The simulated gains at the angle of 0^o, 15^o, and 30^o, are 165.8, 157.3 and 140.6, respectively. The gain degradation is close to the scan loss equation $cos(\theta)$ (θ is scan angle).

From the aforementioned analysis, it can be found that the beam scanning leads to the drop of array gain, which is also predicated on the model of AF. As a consequence, Fig.2.15 shows that the transmission efficiency also drops as with the increase of scan angle. Given a fixed channel transfer matrix, the TR eigenmode technique gives a maximization of PTE and the consequent transmission efficiency η. However, the maximum value of η is limited

by the array setup and propagation medium, no matter what complex excitation vector is. The limitation of array beam scanning is discussed using the model of Plane wave impulse response Element Pattern in [105].

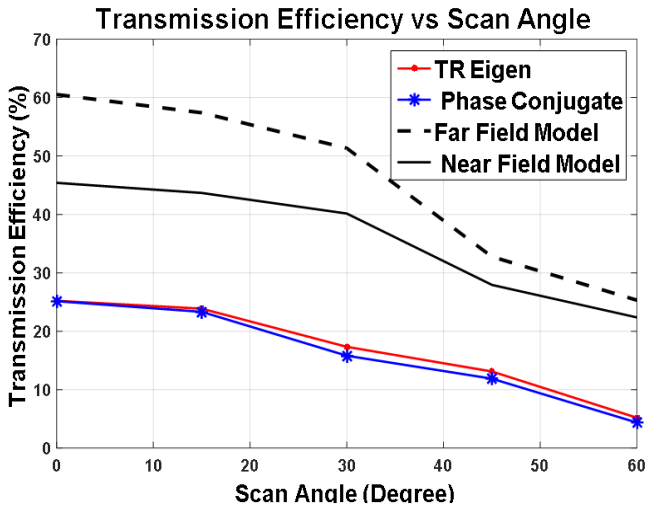

Figure 2.15: Transmission efficiency over different scan angles. The near field and far field models overestimate the transmission efficiency while the PTE has much better accuracy.

2.5.3 Arbitrary Array Beamforming in Multipath Environment

In this subsection, an obscured propagation channel is studied to demonstrate the advantages of TR eigenmode technique in multipatch environment. In this numerical example, a PEC(perfect electric conducting) spherical obstacle is inserted (Fig. 2.16) with a diameter equal to the diagonal length of receive aperture. This example has also been formulated and discussed for the application of wireless communication in [45] and [40].

The PTE and transmission efficiency are tabulated as Table 2.3 for four different techniques. In this case, if the array synthesis and uniform excitation techniques are not well-defined and shown for the purpose of comparison. Because the receiver is located in the region shadowed by the obstacle and no direct beam can be formed towards the receiver, the shaping of the main beam towards any direction leads to a large amount of backward

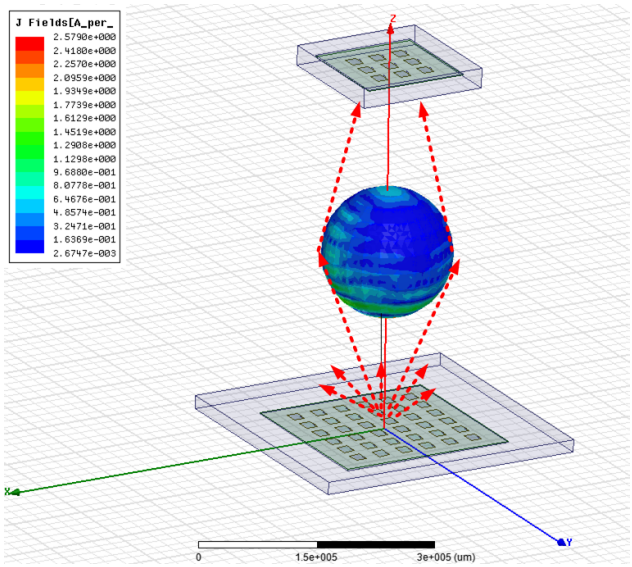

Figure 2.16: Wireless power transfer behind PEC spherical obstacle. No LOS propagation path is available

Table 2.3: Comparison of different optimization techniques for MPT behind PEC spherical obstacle

Beamforming Method	Uniform	Phase Conjugate	TR eigenmode	AF Synthesis
η	2.23%	5.22%	5.85%	2.44%
PTE	3.12%	5.96%	6.39%	3.33%

scattering. Nevertheless, the advantage of phase conjugate and TR eigenmode stands out in the comparison table. These two techniques give several times greater efficiencies (both η and BCE) over the other two techniques. Given the same norm of input power, the eigenmode method has approximately 10% higher efficiencies over the phase conjugate method (Table.2.3). It can be expected the improvements of efficiency from TR-Eigenmode method will be even more significant as with the increase of propagation channel due to the multipath environment.

In Fig.16(a) and (b), the far field pattern from TR eigenmode and phase conjugate tech-

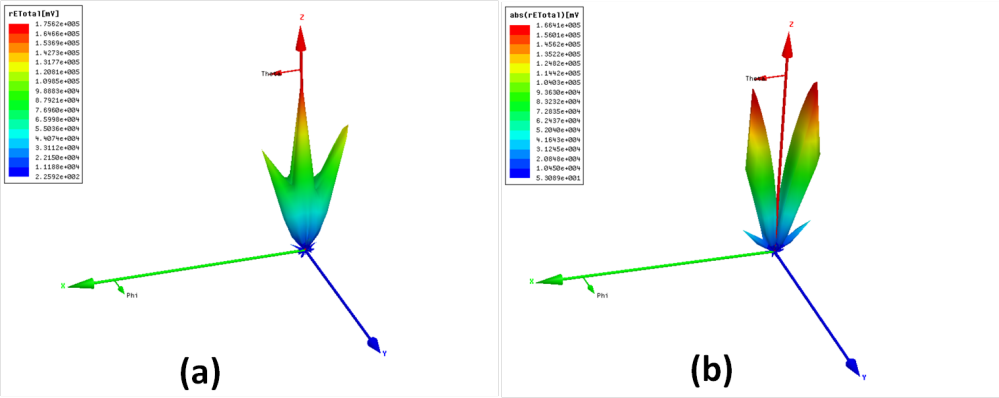

Figure 2.17: Array beamforming with the presence of spherical obstacle:(a)radiation pattern from the phase conjugate (b) radiation pattern from time reversal eigenmode. A significant main lobe exists in (a) and results in the propagation loss.

nique is computed with the results from FEM in HFSS. The reason why TR eigenmode technique is better than phase conjugate technique is shown apparently in Fig.16. Instead of one main beam in traditional beamforming technique, two beams are generated by the eigenvector excitations.The dual-beam maximizes the diffracted wave towards receiver while it minimizes the reflection by the obstacle. The phase conjugate technique, on the other hand, still maintains the main beam in the direction of LOS, apart from two side beams. Therefore, a portion of power is reflected back due to the existence of the main beam. In Fig. 2.16, the induced surface current in MoM-IE method gives an implication of how the two side beam makes use of diffractions.

In short, the TR eigenmode method is the best adaptive array synthesis technique for MPT in the channel with multipath.

2.6 Conclusion

In this chapter, the wireless power transmission system is formulated in terms of the circuit theory and the field theory. The clarification of definitions on powers and efficiencies implies the challenges of estimating the transmission efficiency. For this reason, the classic model

of transmission efficiency based on antenna parameter is reviewed while another transmission equation is presented in terms of the channel transfer function and mutual impedance matrix. Then the experimental study of transmission efficiency is carried out in an indoor environment, which is a rich scattering and multipath environment. The quantitative study of transmission efficiency in experiment shows that the adaptive array beamforming is demanded to improve the MPT in a complex environment.

Furthermore, the exact transmission efficiency is approximated with pseudo transmission equation(PTE) as the coupled power dissipation is sufficiently small if the array spacing is greater than a half wavelength. Based on this approximation, an optimal method is derived from time reversal signal processing technique. As the iterative TR process achieves spatial focusing effect through the automatic probing the channel characteristics, this property enlightens us with its application in the wireless power transmission. Then the iterative process is implemented computationally with eigendecomposition process since the channel transfer matrix can be measured and processed. Based on this principle, the time reversal eigenmode technique is proposed and validated with numerical examples. The MoM-Integral Equation was employed to demonstrate the advantages of the proposed techniques due to the prohibitive cost of the large phased array. From the simulation results, it has been shown that the proposed scheme gives an optimal transmission efficiency for an array with unequal element pattern and arbitrary position. Moreover, the simulation also shows that this method is applicable to the receivers located in either far field or near field region while conventional array synthesis assumes the far field propagation. Most importantly, we have shown that the TR eigenmode technique can improve the transmission efficiency in a complex environment.

Chapter 3

HARD WALL IMAGING OF OBJECTS HIDDEN BY NON-PENETRATING OBSTACLES USING MODIFIED TIME REVERSAL TECHNIQUE

One of the important current problems is imaging and detection of objects hidden by obscuring obstacles. There have been extensive works reported on "Through-Wall Imaging" in recent years. This chapter extends the previous works to the case where the wall is non-penetrating, and the diffraction around the edge becomes important. This hard-wall imaging is related to the historical problem of "Poisson Spot" and "Anti-Podal point". This chapter makes use of the modified time-reversal technique and GTD and shows the formulations of the multistatic data matrix, eigenvectors and steering vectors to form the imaging function. Signal processing includes the multiplicative modified time reversal technique to eliminate the unwanted extraneous images. Numerical examples include comparisons between the modified and the conventional time-reversal imaging to show the effectiveness of the hard-wall imaging method.

3.1 Introduction

One of the important current problems is imaging and detection of objects hidden by obscuring obstacles. In recent years, there have been extensive researches reported on "Through-Wall Imaging". They include imaging through opaque scattering walls [31], non-linear inverse technique [83], chaos-based technique [86], wide-band beamformer [3], Time-Reversal Mirror Technique [106], UWB imaging radar [94], singular value decomposition (SVD) inversion scheme [80], UWB SAR imaging [65], Time Reversal processing applied to moving targets [59], and historical perspective and future direction noting interplay between propa-

gation and signal processing [7].Dyadic Green's functions are studied for three-dimensional through-the-wall imaging [103]. The use of UTD in ray-tracing and multiple wall transmission, reflection and diffraction are presented for through-wall building imaging [104]. Time reversal MUSIC method is used in through-wall imaging [14] and imaging through a periodic wall structure is studied with the use of non-linear minimization solution to correct the target distortion [13].

In this chapter, we attempt to go beyond the through-wall imaging to the case where the wall is non-penetrating, and therefore the diffraction around the edges and the openings of the wall becomes important. The hard-wall imaging complements the through-wall imaging in the study of detection and imaging in geophysical or biological environments, where it may be difficult to obtain information of hidden objects using the conventional technique.

Hard-wall imaging is related to the historical problem of diffraction behind a circular disk and a sphere known as "Poisson Spot" or "Avago Spot", which was discussed by Sommerfeld [81]. This is also related to an increase of the radio signal strength at the antipodal point of the earth [88]. This is also related to the BTH (beyond-the-horizon) radar, and the use of creeping waves, and surface waves [11] [39].

This chapters makes use of the modified Time Reversal technique to obtain the image behind the wall. Green's function and the steering vector are obtained by GTD. The signal processing makes use of the "multiplication" method rather than the conventional "additive" time reversal imaging method. This multiplication method is related to the multiplicative or correlation array such as Mills Cross [19] which are discussed as one of the signal processing antennas [19]. In this chapter, we deal with a point target only and therefore the problem which arises from a multiple-target is not discussed in Sections II to IV. However, some discussions on multiple target imaging are included at the end of Section V. Numerical examples are given to show the spot images of a point target behind a perfectly-conducting wall and to show the comparison between the conventional and the modified time reversal technique.

In this chapter, we attempt to show two key points. First, if a wall is non-penetrating, we

need to devise a method to make use of the diffracted wave. However, conventional use of the diffraction including time-reversal produces extra superfluous images as shown in Figs. 3.9 and 3.11 and cannot give a clean image. To overcome this problem, we devised a modified signal processing and obtained a clear image as shown in Fig. 3.12. This is the second key point of this chapter.

3.2 Time-Reversal Imaging of a point target

Time reversal imaging has been extensively studied by Fink, Prada, Devaney, Yavuz, Teixeira and many others [22,29,72,74,95]. Here we briefly review and outline the conventional time-reversal imaging for a point target. Multi-static data matrix $[K_{ij}]$ is a symmetric matrix and its element K_{ij} is the signal received at the $i-th$ antenna where the signal is emitted from the $j-th$ antenna and reflected by the target. For a point target, $\mathbf{K}$ is given by

$$\mathbf{K} = \mathbf{g}\mathbf{g}^T, \mathbf{g} = [g_1, ..., g_N]^T \tag{3.1}$$

where g_i is the Green's function, $\mathbf{g}^T$ is the transpose of $\mathbf{g}$, Fig. 3.1

Figure 3.1: Point target behind hard wall

Transmitted signal $\mathbf{v}$ propagates to the target and is reflected back to the receiver and is given by $\mathbf{Kv}$. This is time-reversed given by the conjugate $[\mathbf{Kv}]^*$ and is transmitted. In our time reversal process, the time-reversed transmitted signal is proportional to the original transmitted signal with the singular values σ. This is consistent with DORT [95]

and SVD [22].

$$[\mathbf{Kv}]^* = \sigma\mathbf{v} \tag{3.2}$$

Taking the conjugate and multiplying by $\mathbf{K}^*$, we get

$$\mathbf{K}^*\mathbf{Kv} = \mathbf{K}^*(\sigma\mathbf{v})^* = \sigma^*(\mathbf{Kv})^* = \sigma^*\sigma\mathbf{v} \tag{3.3}$$

This is the time-reversal eigenvalue equation.

$$\mathbf{Tv} = \lambda\mathbf{v} \tag{3.4}$$

where $\mathbf{T} = \mathbf{K}^*\mathbf{K}$=Time Reversal Matrix,
$\lambda = \sigma^*\sigma$=eigenvalue. For a point target, we note

$$\mathbf{K}^*\mathbf{K}\mathbf{g}^* = \lambda\mathbf{g}^* \tag{3.5}$$

Therefore, the eigenvector $\mathbf{v}$ is equal to

$$\mathbf{v} = \mathbf{g}^* \tag{3.6}$$

And the eigenvalue is

$$\lambda = [\mathbf{g}^H\mathbf{g}]^2 \tag{3.7}$$

where H denotes conjugate transpose. It is, therefore, possible to obtain the eigenvector and the eigenvalue for a given point target problem, analytically, numerically or experimentally. Note that this process of obtaining the eigenvector experimentally can be done without the knowledge of the geometry of the problem. It requires, however, that the multistatic data matrix is determined.

Once we obtain the eigenvector and the eigenvalue, we can then obtain the image by using the steering vector $\mathbf{g}_s$, focused on the search point $\vec{r}_s$. If the steering vector is Green's function for the problem, then the wave will be focused on the target. In general, however, we may not know the exact Green's function without some knowledge of the problem. We will formulate the steering vector as shown in the next section.

In summary, we first obtain the multistatic data matrix and the eigenvector without the knowledge of the geometry of the problem. Then we construct the steering vector $\mathbf{g}_s$ based on some knowledge of the problem. With the eigenvector $\mathbf{v}$ the eigenvalue λ and the steering vector $\mathbf{g}_s$, we construct the imaging function Ψ [22, 41, 44, 95, 96].

$$\Psi = \frac{1}{2\pi} \int_{\Delta\omega} d\omega |U|^2 \sqrt{\lambda} \mathbf{g}_s^T \mathbf{v} \tag{3.8}$$

where U is the spectrum of the transmitted signal.

Here, we followed the ultrawideband (UWB) imaging functions given by Yavuz and Teixeira based on the application of SVD (singular value decomposition) [96].

3.3 Green's function for a point target behind hard wall

As stated in the last section, in order to obtain the imaging function (3.8), we need to obtain the eigenvector $\mathbf{v}$, the eigenvalue λ and the steering vector $\mathbf{g}_s$. The eigenvector is obtained by the time-reversal matrix, which can be constructed by multistatic data matrix. For a point target, the multistatic data matrix and the eigenvectors are given by Green's function. Even though Green's function for a hard wall can be obtained by numerical or experimental work, in this section, we give an approximate Green's function using GTD (Geometric Theory of Diffraction).

Consider a perfectly conducting hard-wall of width H placed between the transmitting-receiving array and a point target at $\vec{r}_t$imply Fig. 3.2. Here we use the G TD, which applies to the diffraction region. For our problem, we do not need to consider the incident and reflected waves, and the reflection and shadow boundaries, for which UTD and ATD need to be considered [36, 39].

The use of GTD is only for the cases we calculated, where the target is in the shadow region. However, in general, when the target can be located near the shadow boundary, UTD or ATD need to be applied. Green's function f for a point source at $\vec{r}_t$ and observed at $\vec{r}_i$ is

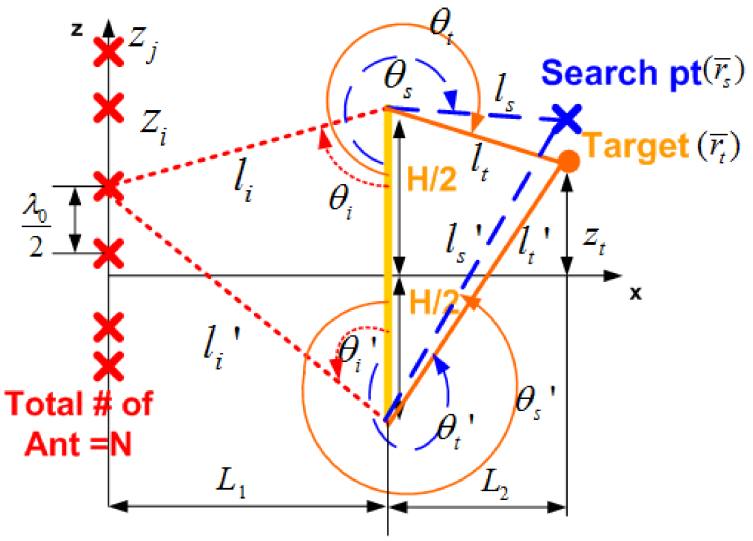

Figure 3.2: Green's functions g_i from transmitting and receiving arrays to hard wall with size H and to the target at $\vec{r}_t$. Also shown is the search point $\vec{r}_s$ for steering vector $\vec{g}_s$

therefore given by

$$\begin{aligned} f &= f_i + f_i^{'} \\ f_i &= G_i exp[ik(l_i + l_t)] \\ f_i^{'} &= G_i^{'} exp[ik(l_i^{'} + l_t^{'})] \end{aligned} \tag{3.9}$$

$$\begin{aligned} G_i &= \frac{1}{4\pi l_i} D(\theta_t, \theta_i) \sqrt{\frac{l_i}{l_t(l_i + l_t)}} \\ G_i^{'} &= \frac{1}{4\pi l_i^{'}} D(\theta_t^{'}, \theta_i^{'}) \sqrt{\frac{l_i^{'}}{l_t^{'}(l_i^{'} + l_t^{'})}} \end{aligned} \tag{3.10}$$

where $D(\theta_t, \theta_i)$ is the diffraction coefficient given by

$$\begin{aligned} D(\theta_t, \theta_i) &= \frac{-exp(i\pi/4)}{2(2\pi k)^{1/2}} [\frac{1}{cos(\frac{\theta_t - \theta_i}{2})} \mp \frac{1}{cos(\frac{\theta_t + \theta_i}{2})}] \\ D(\theta_t^{'}, \theta_i^{'}) &= \frac{-exp(i\pi/4)}{2(2\pi k)^{1/2}} [\frac{1}{cos(\frac{\theta_t^{'} - \theta_i^{'}}{2})} \mp \frac{1}{cos(\frac{\theta_t^{'} + \theta_i^{'}}{2})}] \end{aligned} \tag{3.11}$$

The minus sign is for Dirichlet boundary condition and the plus sign is for the Neummann

boundary condition.

For the steering vector, we use GTD and the Green's function given by

$$\begin{aligned} g_{si} &= G_{si} exp[ik(l_i + l_{si})] \\ g'_{si} &= G'_{si} exp[ik(l'_i + l'_{si})] \\ G_{si} &= \frac{1}{4\pi l_i} D(\theta_s, \theta_i) \sqrt{\frac{l_i}{l_s(l_i + l_s)}} \\ G'_{si} &= \frac{1}{4\pi l'_i} D(\theta'_s, \theta'_i) \sqrt{\frac{l'_i}{l'_s(l'_i + l'_s)}} \end{aligned} \tag{3.12}$$

It should be noted that these diffraction coefficients are relatively slowly varying. What is important is the phase as given in (3.9). We also make use of the Gaussian input pulse given by

$$\begin{aligned} u(t) &= A_0 exp(-i\omega_0 t - \frac{t^2}{T_0^2}) \\ U(\omega) &= A_0 \frac{2\sqrt{\pi}}{\Delta\omega} exp(-\frac{(\omega - \omega_0)^2}{\Delta\omega^2}) \end{aligned} \tag{3.13}$$

with the bandwidth $\Delta\omega$ given by $2/T_0$.

3.4 Conventional Imaging Function for Hard Wall

Using (3.9),(3.10),(3.11),(3.12) and (3.13), we obtain the imaging function. We first note that Green's function of the steering vector consists of two paths diffracted by the two edges. Fig. 3.3. Green's function ($\mathbf{f_1} + \mathbf{f_2}$) is from numerical or experimental data and therefore this cannot be separated. However, the steering vector $\mathbf{g_{s1}}$ and $\mathbf{g_{s2}}$ are signal processing and therefore we can have the choice of $\mathbf{g_{s1}}$ and $\mathbf{g_{s2}}$. If we use $\mathbf{g_{s1}}$, then we obtain

$$\Psi_1 \rightarrow \mathbf{g_{s1}}(\mathbf{f_1}^* + \mathbf{f_2}^*) \rightarrow T_1 + T_3 \tag{3.14}$$

If we use $\mathbf{g_{s2}}$, then we obtain

$$\Psi_2 \rightarrow \mathbf{g_{s2}}(\mathbf{f_1}^* + \mathbf{f_2}^*) \rightarrow T_2 + T_4 \tag{3.15}$$

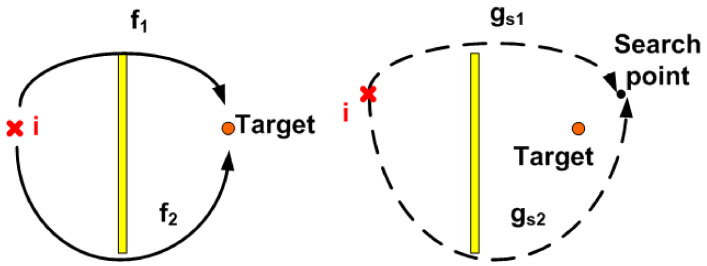

Figure 3.3: Green's function $(\mathbf{f_1} + \mathbf{f_2})$ and the steering vector $(\mathbf{g_{s1}} + \mathbf{g_{s2}})$

Including the input spectrum $U(\omega)$ integrating with respect to ω in (3.8), we obtain the following analytical formulae.

$$
\begin{aligned}
T_1 &= \frac{\sqrt{\lambda}4\pi}{(\Delta\omega)^2}\sqrt{\frac{\pi}{2}}G_iG_{si}^* \\
&\quad exp[-\frac{k_0^2(l_t+l_i-l_s-l_i)^2}{8}(\frac{\Delta\omega}{\omega_0})^2 + ik_0(l_t+l_i-l_s-l_i)] \\
T_2 &= \frac{\sqrt{\lambda}4\pi}{(\Delta\omega)^2}\sqrt{\frac{\pi}{2}}G_iG_{si}^{*'} \\
&\quad exp[-\frac{k_0^2(l_t+l_i-l_s'-l_i')^2}{8}(\frac{\Delta\omega}{\omega_0})^2 + ik_0(l_t+l_i-l_s'-l_i')] \\
T_3 &= \frac{\sqrt{\lambda}4\pi}{(\Delta\omega)^2}\sqrt{\frac{\pi}{2}}G_i'G_{si}^* \\
&\quad exp[-\frac{k_0^2(l_t'+l_i'-l_s-l_i)^2}{8}(\frac{\Delta\omega}{\omega_0})^2 + ik_0(l_t'+l_i'-l_s-l_i)] \\
T_4 &= \frac{\sqrt{\lambda}4\pi}{(\Delta\omega)^2}\sqrt{\frac{\pi}{2}}G_i'G_{si}^{*'} \\
&\quad exp[-\frac{k_0^2(l_t'+l_i'-l_s'-l_i')^2}{8}(\frac{\Delta\omega}{\omega_0})^2 + ik_0(l_t'+l_i'-l_s'-l_i')]
\end{aligned}
\tag{3.16}
$$

where the eigenvalue λ is approximately evaluated in (3.8),(3.13) and (3.16),$k = \frac{\omega}{c}$ and $k_0 = \frac{\omega_0}{c}$. First we note that T_1 has the magnitude proportional to the exponential function $exp[-(k_0^2(l_t+l_i-l_s-l_i)^2(\frac{\Delta\omega}{\omega_0})^2)/8 + ik_0(l_t+l_i-l_s-l_i)]$. This means that as long as $(l_t+l_i-l_s-l_i)$ is the same, this term is the same. This is a circle with the edge at the center, Fig. 3.4. Similarly, we have T_1, T_2, T_3 and T_4 with each on different circles as shown in Figs. 3.6 and 3.8.

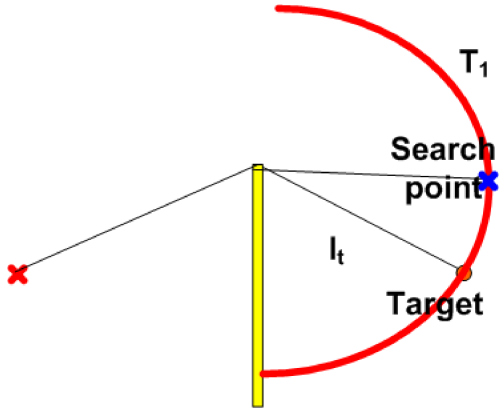

Figure 3.4: T_1 is proportional to the magnitude on a circle centered at the edge

Figures 3.6, 3.8, 3.9, and 3.11 show the imaging based on the conventional time reversal method, indicating the spurious images. Fig. 3.12 shows the results of the use of the modified signal processing with clear images without spurious images.Note that the magnitude of the images are less for Dirichlet than for the Neumann condition because the fields at the edges are zero for the Dirichlet, but are large for Neumann condition. Note that Figs. 3.6 and 3.9 are for the single antenna and Figs. 3.8 and 3.11 are for the array antenna based on the conventional time-reversal method.

Conventional time-reversal imaging is based on (3.8). The steering vector $\mathbf{g_s}$ is therefore a sum of $\mathbf{g_{s1}}$ and $\mathbf{g_{s2}}$ and the imaging function Ψ_c is proportional to

$$\Psi_c \propto (\mathbf{g_{s1}} + \mathbf{g_{s2}})(\mathbf{f_1}^* + \mathbf{f_2}^*) \tag{3.17}$$

which can be expanded as

$$\Psi_c = \sum_i (T_1 + T_2 + T_3 + T_4) \tag{3.18}$$

The conventional image is shown in Fig. 3.11, where the down range distance from array to hard wall $L_1 = 10\lambda_0$, the down range distance from wall to target distance $L_2 = 10\lambda_0$, the width of hard wall $H = 18\lambda_0$ and the cross range location of target $z_t = -5\lambda_0, 0\lambda_0$,and $3\lambda_0$. The bandwidth is $\Delta\omega = 0.5\omega_0$. The array consists of $N = 10$ elements with $\lambda_0/2$ spacing. Hence, we show each term of T_1, T_2, T_3 and T_4 in Figs. 3.5 and 3.7. Fig. 3.6 is for a single

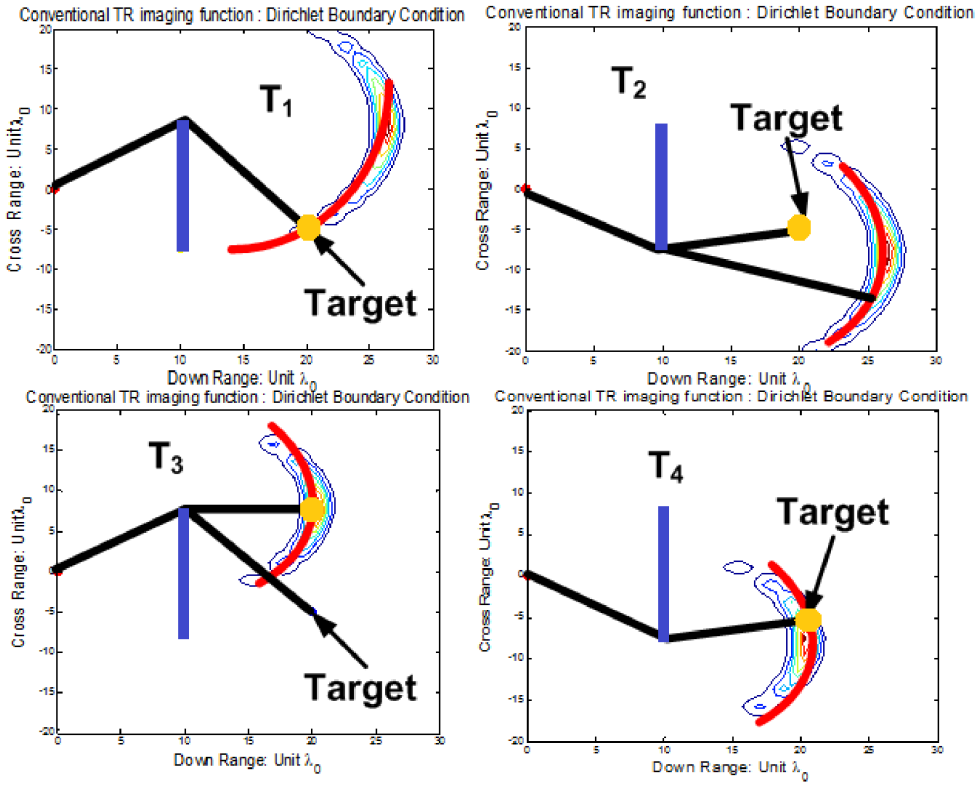

Figure 3.5: Image due to each terms for single antenna under Dirichlet boundary condition: Each Term T_1, T_2, T_3 and T_4 are shown for single antenna. Note that T,T_2,T_3,and T_4, are individual terms, shown in (3.14) and (3.15). The location of the target is shown by the yellow circle.

antenna while Fig. 3.8 is for array antennas. We also show in Figs. 3.6 and 3.8 the partial sum $T_1 + T_3$ and $T_2 + T_4$ .If we add these two ,$T_1 + T_2 + T_3 + T_4$, we obtain the conventional time reversal images. This is shown in Fig. 3.11.

3.5 New Multiplicative Imaging Function for Hard Wall

Next we show the image using the modified time-reversal technique.

It is clear that the addition of T_1, T_2, T_3 and T_4 with each on different circles creates a combination of those shown in Fig. 3.9 (single antenna) and Fig. 3.11 (array antenna). with resulting complicated figures. What is needed is to cancel out the images other than the

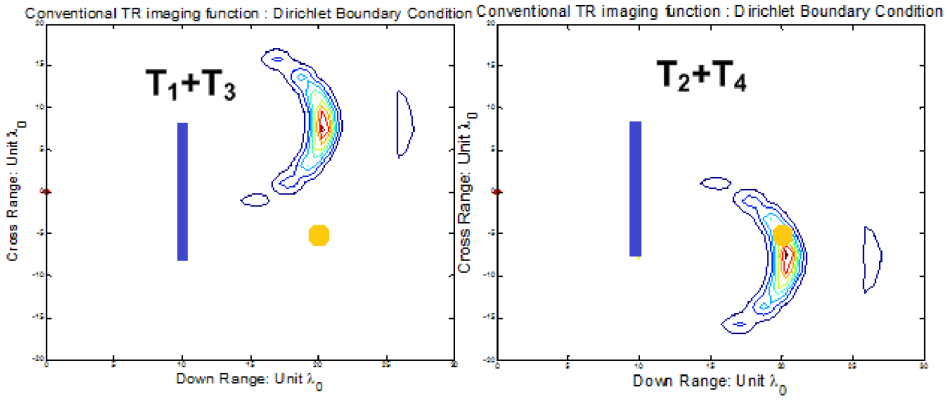

Figure 3.6: Image due to each terms for single antenna under Dirichlet boundary condition: Left figure is showing $T_1 + T_3$, and Right figure is showing $T_2 + T_4$ for single antenna.

image from the target.

It is known in the study of signal processing antennas [19] that there are several processing antennas techniques. One of them is multiplicative arrays (Chapter 27, [19]), where the outputs of two arrays are multiplied and averaged to form a narrow beam which was used in Mills Cross [19]. It may be possible to utilize the similar ideas for our time-reversal imaging. This can be done by the multiplication of the images. Specifically, if we form the imaging function by the following multiplication, we should obtain a clear image of the point target.

$$\Psi = \Psi_1 \Psi_2 = \sum_i (\mathbf{T_1} + \mathbf{T_3})(\mathbf{T_2} + \mathbf{T_4}) \tag{3.19}$$

This is an important equation to show our modified signal processing technique. Let us examine Fig.6(b). Note that $T_1 + T_3$ has a circular image and $T_2 + T_4$ has a different circular image. These two images do not overlap except at the target point. Therefore, if we can eliminate these circular images, but keep the target image, we can achieve a clear image of the target without extraneous circular images. This can be done by multiplying $T_1 + T_3$ and $T_2 + T_4$ as shown in (3.19). Note that by this multiplication, the circular images of $T_1 + T_3$ and $T_2 + T_4$ disappear, while keeping the target image.

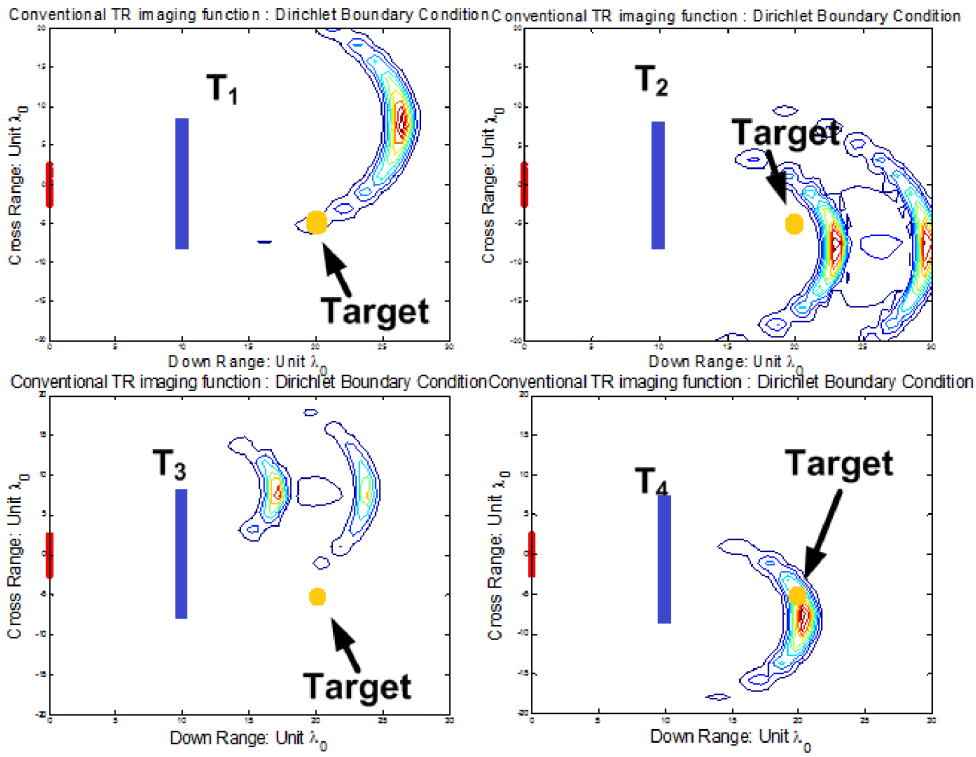

Figure 3.7: Image due to each terms for array antenna under Dirichlet boundary condition: Each Term T_1, T_2, T_3 and T_4 are shown for array antenna

Fig.3.10 shows numerical examples of this image for a single antenna. Fig.3.10 (a),(c) and (e) are for the Dirichlet boundary condition and Figs.3.10(b),(d) and (f) are for the Neumann boundary condition. Fig. 3.12 is based on the new modified time reversal technique under the same condition as in Fig. 3.11 which is based on the conventional time-reversal technique. Note that Fig. 3.11 is based on the additive technique and therefore it exhibits many unwanted extraneous images while Fig. 3.12 is based on the new multiplicative technique exhibiting images of targets with improved resolution. Let us consider the difference between the single antenna and the array antenna. Fig. 3.10 shows the images for the single antenna and Fig. 3.12 shows the images for the array antenna based on the new modified time-reversal signal processing. It may appear that since the target is at the intersection of the circles originating from the edges, an array is not needed. Figs. 3.10 and 3.12 show

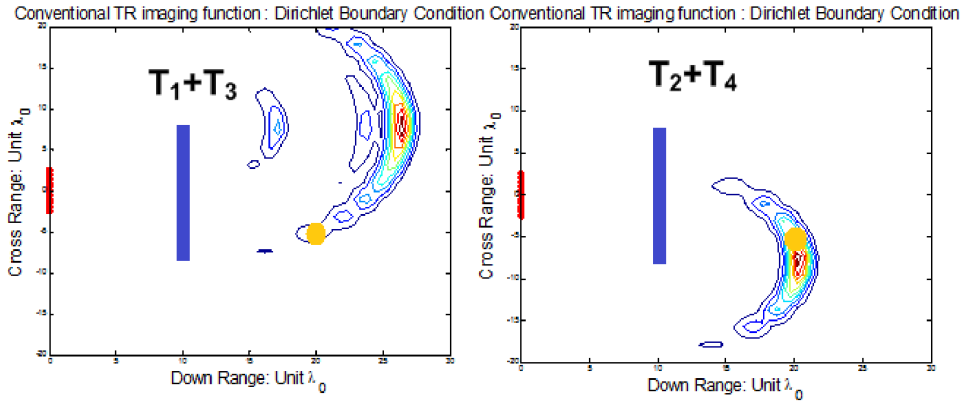

Figure 3.8: Image due to each terms for array antenna under Dirichlet boundary condition: Left figure is showing $T_1 + T_3$, and Right figure is showing $T_2 + T_4$ for array antenna.

the advantages of the use of the array. As shown in Fig. 3.10, a single antenna produces significant spurious images, but the array antenna, as shown in Fig. 3.12, average out the undesirable terms so that we can have one clear image at the intersection between two desirable terms.

In summary, the imaging process using modified time-reversal method can be stated as follows. We first conduct an experiment to obtain multi-static data matrix, eigenvector, and eigenvalue. We then construct the steering vector based on the position of the hard wall. We form the imaging function as stated in (3.19) rather than the conventional imaging function (3.18). Examples in Fig. 3.11 (conventional) and Fig. 3.12 (modified time-reversal) show the effectiveness of this method.

This chapter presents the basic ideas of hard wall imaging. However, studies of several key problems are being conducted at the present and are not included in this chapter. They include the choice of bandwidth and the array, which will affect the range of validity of the target locations. Numerical and experimental verifications of this proposed hard wall imaging technique will be presented in subsequent studies.

If there are M targets, the multi-static data matrix $\mathbf{K}$ in (3.1) becomes a series of M matrices, each of which is $N \times N$ matrix. There may be M_1 independent targets which

may be called "well resolved". [22] The imaging function for these M_1 targets is a sum of the images of each target. However, if there are M_2 targets which are not independent, the imaging function needs to include the correlations between the targets. The complete imaging function is the sum of the images of the well-resolved targets and the correlated targets. Further study on multiple targets is under way.

3.6 Conclusion

This chapter shows a method of obtaining the image of a point target behind the non-penetrating hard wall. It makes use of the modified time-reversal method and GTD to form imaging function based on the multistatic data matrix, eigenvectors and steering vectors. In particular, it makes use of signal processing multiplication time-reversal method shown in (3.19) and Fig.3.12 to eliminate extraneous images of the conventional method given in (3.18) and Fig.3.11 to form clear images of a point target behind hard-wall.

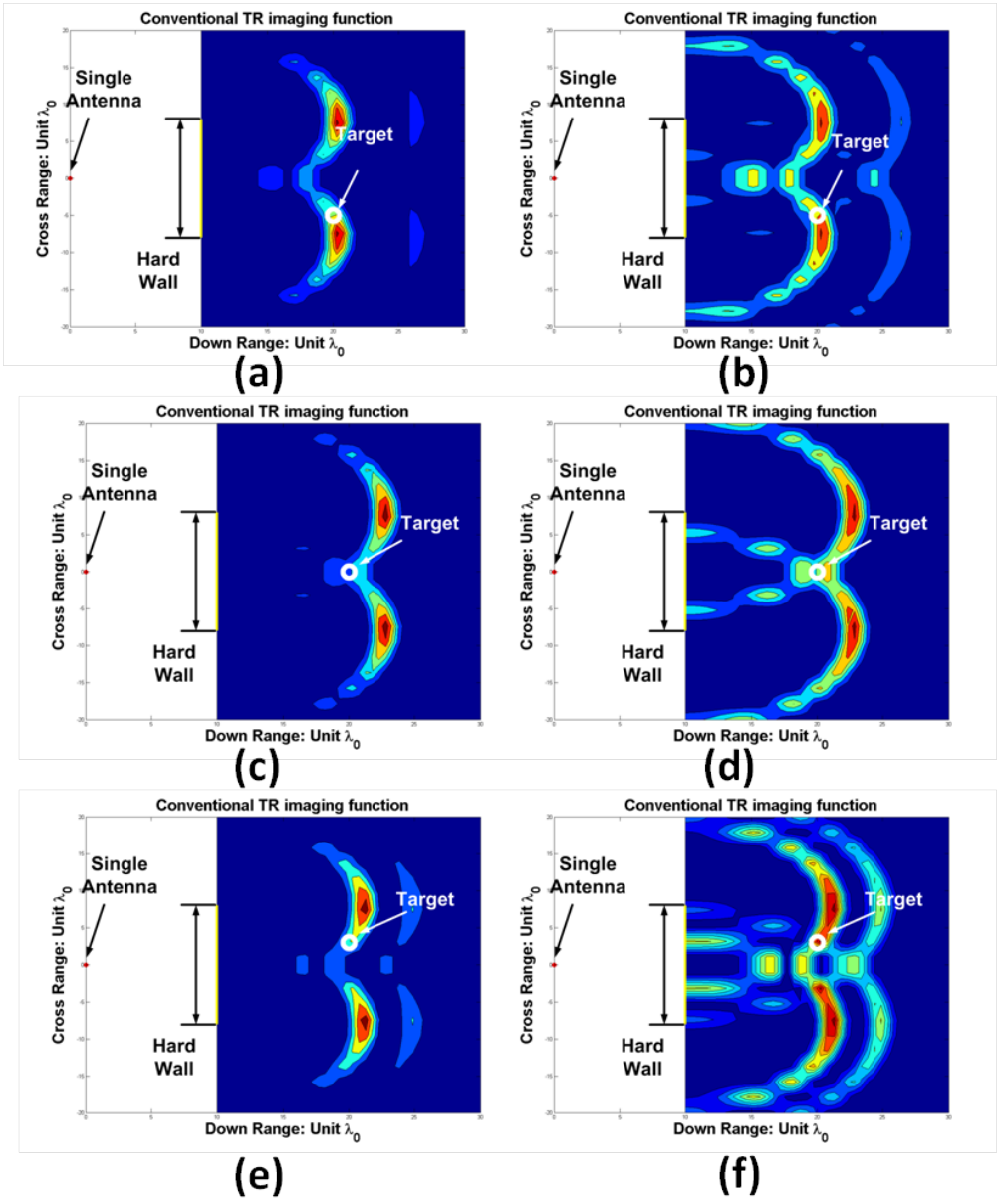

Figure 3.9: Conventional Time-Reversal imaging of a point target: Dirichlet boundary condition: (a)(c)(e) Neumann boundary condition (b)(d)(f) for single antenna

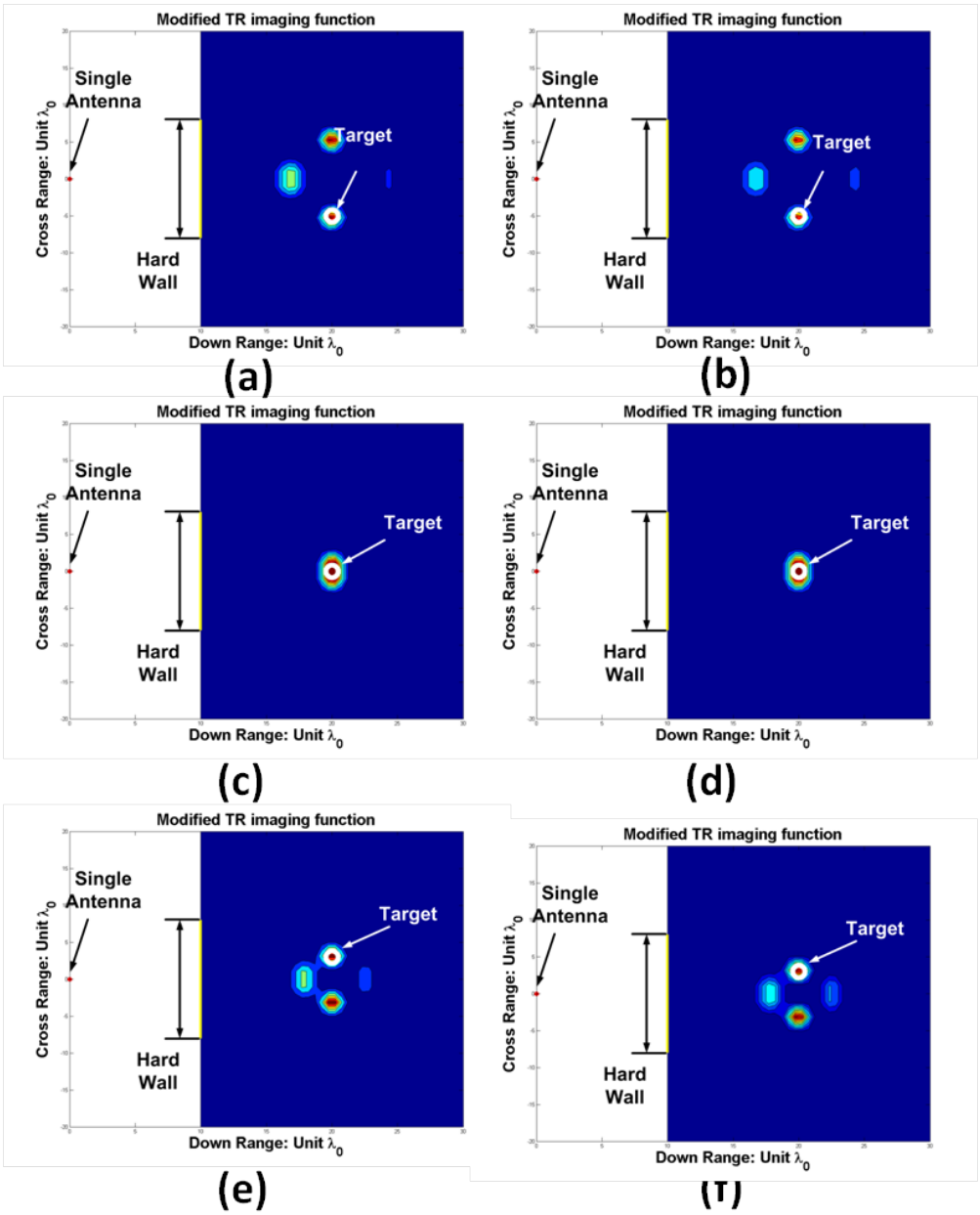

Figure 3.10: New Modified Time-Reversal imaging of a point target under the same condition as in Fig.7: Dirichlet boundary condition: (a)(c)(e) Neumann boundary condition (b)(d)(f) for single antenna

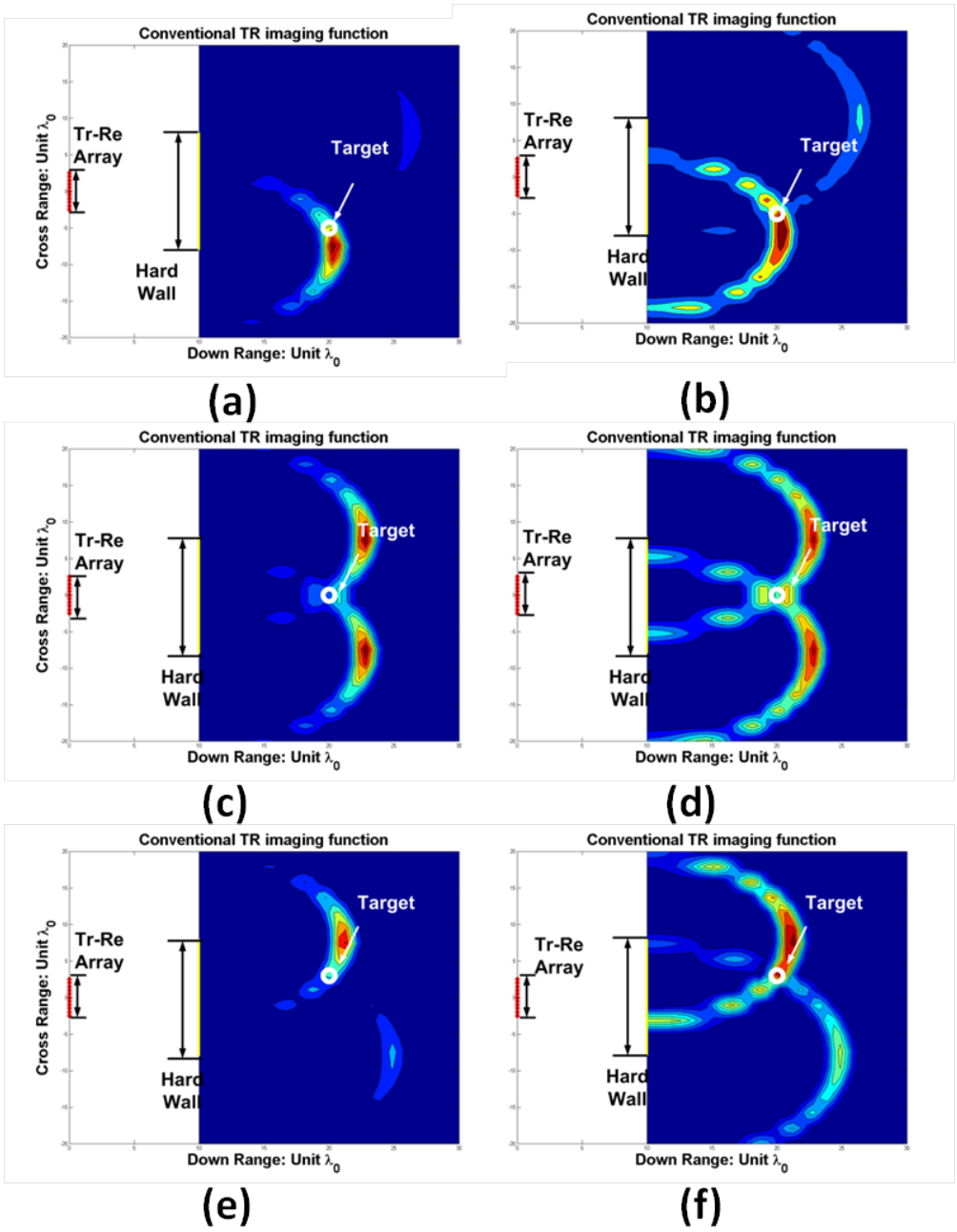

Figure 3.11: Conventional Time-Reversal imaging of a point target behind a hard wall: Dirichlet boundary condition: (a)(c)(e) Neumann boundary condition: (b)(d)(f) for array antenna

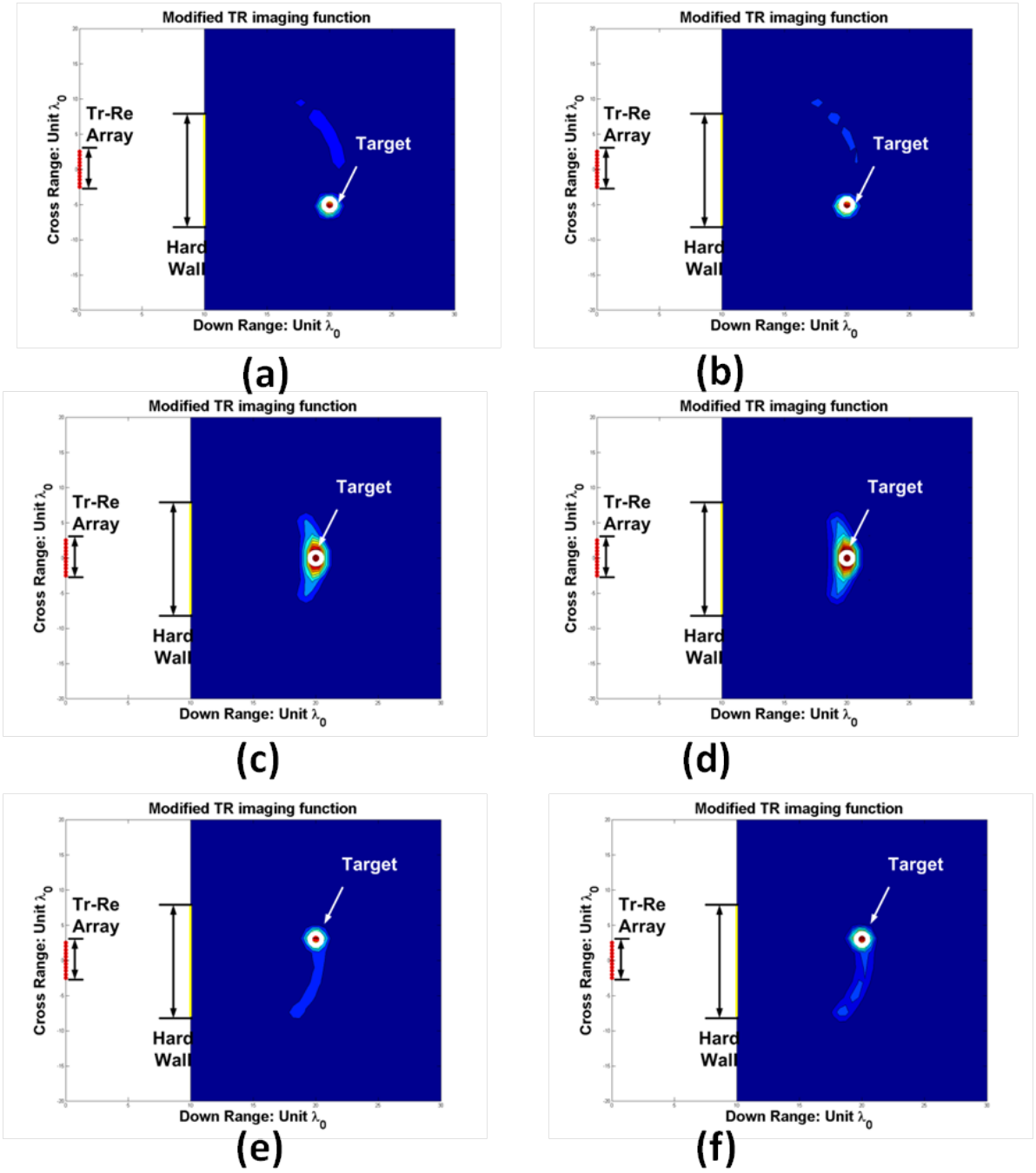

Figure 3.12: New Modified Time-Reversal imaging of a point target under the same condition as in Fig.9: Dirichlet boundary condition: (a)(c)(e) Neumann boundary condition (b)(d)(f) for array antenna

Chapter 4

HARD WALL RADAR IMAGING: LOCALIZATION OF OBJECTS SHADOWED BY METALLIC WALLS WITH DISTRIBUTED MIMO

The technology of "Through-the-Wall Radar Imaging" enables us to see through the walls by reconstructing the image based on the backscattered waves passing through the optically opaque dielectric wall. However, when the electromagnetic waves cannot penetrate the shielding walls (such as metallic walls), a new problem called "Hard-Wall Radar Imaging" (HWRI) has been proposed. As the objects are located in the shadow region in this problem, where only diffracted field can be reflected back via edges, the conventional imaging techniques are not applicable. The HWRI problem is an imaging scenario with intrinsic multipath of signal propagation, so it has been previously resolved numerically and experimentally with a model based time reversal DORT (Decomposition of Time-Reversal Operator) imaging algorithm. In this chapter, a new imaging algorithm with distributed transmitting and receiving array is proposed as a robust method to resolve the problem of the low signal-to-clutter ratio (SCR) in time-reversal imaging. In this algorithm, the interelement response matrix is collected for the construction of covariance matrix, from which the geometry of hard wall is determined from the Direction of Arrival (DoA) by MUSIC (multiple signal classification) techniques. Next, the adaptive nulling technique is applied to suppress the interference terms in the image function due to the multipath of backscattering. The experimental results have been obtained from a distributed MIMO radar system and show that this new algorithm is useful for not only the detection of weak object echo but also the localization of multiple targets hidden behind the wall.

4.1 Introduction

Electromagnetic waves at microwave frequency can propagate through the common building walls including the concrete and composite walls, which are multi-layered dielectric structures. The backscattered waves from objects shielded by walls are collected by sensors situated at a stand-off range outside the buildings and processed to localize/image the objects. This technology has been called as Through-the-Wall Radar Imaging (TWRI) [3, 7, 59, 83, 94, 104, 106], and has important applications in sensing military personnel and weapons in the battlefield. In recent years, there has been a variety of radar imaging system developed to resolve this research problem.

If the dielectric walls are replaced by conducting shield, the conventional TWRI algorithm is not applicable to give any information about the objects inside the building because the electromagnetic waves are mostly reflected backward. For this reason, a new research topic has been proposed in [42, 101] and is defined as Hard-Wall Radar Imaging (HWRI). In [42] and [101], the HWRI problem has been studied using a modified time reversal DORT (Decomposition of Time-Reversal Operator) imaging algorithm because the HWRI has intrinsic multipath wave propagation. Although the DORT algorithm has the advantages of achieving a good image resolution in a multipath environment, it has been found that the time-reversal imaging technique is susceptible to noise and clutter response in real HWRI application. As the observed field at receiving array experiences the edge diffraction for twice, the observed object echo is very weak and hard to be differentiated from clutter reflections. To enable HWRI system in the open field, the transmitting and receiving array are separated as what is used in distributed MIMO radar system. The highly directional antenna is used as illumination antenna while the wide beamwidth antenna is used for wide observation angle. In our lab measurement, the signal-to-noise ratio (SNR) and signal-to-clutter ratio (SCR) have been improved significantly with this new radar system,

In this chapter, we propose to utilize the MIMO radar configuration and modify the imaging algorithm proposed in [42] and [101] accordingly. In the experiment, it has been shown

that both SNR and SCR have been improved greatly. The details of this new system including hardware signal processing and analysis will be presented in this chapter. The chapter is organized as follows. In Section 4.2, the principle of electromagnetic wave diffraction will be recapped and its application in our imaging scenario will be discussed. In this section, the HWRI is compared with the TWRI with the discussion about its challenges and modeling of wave propagation. Section 4.3 briefly presents our initial multistatic radar system with time reversal DORT algorithm in the experiment. In Section 4.4, the radar system is categorized into three parts: antenna array, radar front end, and data acquisition unit. In Section 4.5, the signal is formulated in terms of Green's functions and the imaging algorithm is presented step by step. In Section 4.6, the experiment results are presented, and the limitations of the proposed algorithm are also discussed.

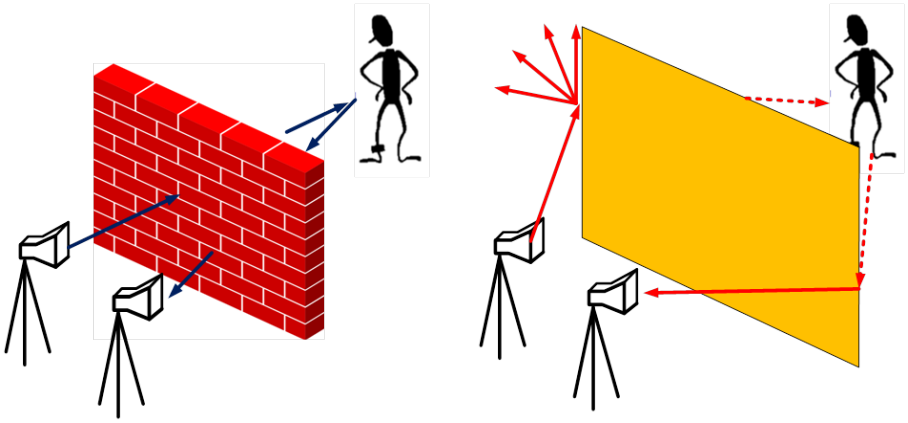

Figure 4.1: Through-the-Wall Radar Imaging (left) vs Hard Wall Radar Imaging (right)

4.2 Background of Hard Wall Imaging

In the past decade, the interest in "seeing" through the walls has been increasingly growing in the urban sensing since this technology enables us to detect, localize and track humans and moving objects inside the buildings. As shown in Fig.4.1, the electromagnetic waves penetrate through the thick lossy walls, so the wave propagation through the multilayered

material is a most critical area of study, which has a direct impact on the accuracy and resolution of imaging. The experimental study on its dielectric properties has been carried out in both frequency domain and time domain with the focus on phase distortions/time delay and amplitude attenuation and, meanwhile, the numerical modeling has also been under study with multi-layered Green's function [53] and ABCD matrix [104].

Nevertheless, the extensive studies on wave propagation through dielectric walls turn out to be invalid if the "anti-imaging" wall (hard wall) with the metallic layer is devised to shield the building interior as shown in Fig.4.1. It looks "impossible" to detect the objects behind the hard wall if this shielding approach is taken. However, it is may not be true if we pay special attention to the phenomenon of "diffraction", which is normally neglected in geometric optics. In fact, a small portion of electromagnetic energy is deflected towards the "seemingly" shadow region, where the objects of interest are located. Thanks to the diffraction phenomenon, the objects in shadow are illuminated, and the backscattered waves from the object behind the hard wall are observable. In the next subsection, the diffraction is modeled and discussed before formulating the imaging system.

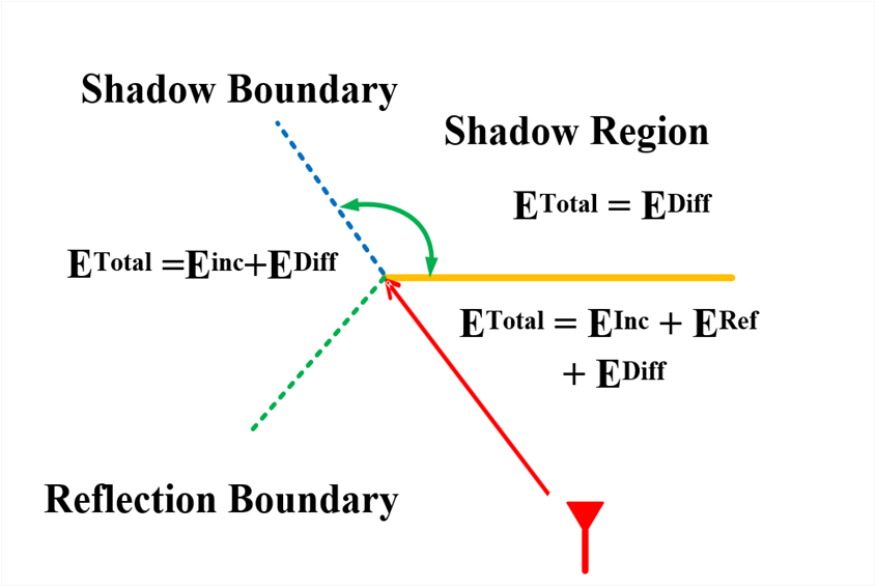

Figure 4.2: Sharp planar edge diffraction

4.2.1 Revisit of Electromagnetic Wave Diffraction

The old geometrical optics theory had been widely used for many years, but its failure of modeling the phenomenon of diffraction was unresolvable until the introduction of the geometric theory of diffraction (GTD) was proposed by J.B. Keller in 1962 [48]. From the theory of GTD, the diffracted field along the diffracted rays due to local plane wave is numerically modeled by noting the fact that caustics of the diffracted the are formed by an edge. In the case of HWRI, the hard/metallic wall can be modeled as sharp planar edge using two-dimensional simplification and the edge diffraction with planar wave incident can be illustrated as in Fig.4.2. By GTD, the electromagnetic wave shielding casts a shadow on the objects located in the diffraction-only region so the only field we can make use of is diffracted field.

In [39], the diffracted field is related to the incident field by using complex diffraction coefficient in Eq.(4.1).

$$D(\theta_s, \theta_i) = \frac{-\exp(\frac{i\pi}{4})}{2\sqrt{2\pi k_0}}[\frac{1}{\cos\frac{\theta_s-\theta_i}{2}} \pm \frac{1}{\cos\frac{\theta_s+\theta_i}{2}}] \tag{4.1}$$

where + is for Neumman Boundary Condition and - is for Dirichlet Boundary Condition .

However, near the incident and reflected shadow boundaries, the GTD formulation yields singular results due to the asymptotic approximation of the Sommerfeld half plane solution. To overcome the drawbacks of GTD, several theories have been devised by researchers such as uniform theory of diffraction (UTD), uniform asymptotic theory (UAT) and Spectral Theory of Diffraction (STD). These theories improve the accuracy of analytical computation of total field in the applications with diffraction involved like antenna and scattering at the cost of computation load. Now the UTD and GTD are compared to check whether the GTD is sufficient in the hard wall imaging. In [39], the UTD is also used to obtain the diffraction coefficient as in Eq.(4.2)

$$D(\theta_s, \theta_i) = D(\theta_s - \theta_i) \pm D(\theta_s + \theta_i) \tag{4.2}$$

where + is for Neumman Boundary Condition and - is for Dirichlet Boundary Condition. θ_s is the diffraction angle and θ_i is the incident angle .

$$D(\beta) = e^{j\frac{\pi}{4}}\sqrt{\frac{L}{\pi}}e^{jX}F(\sqrt{X})sgn(\beta-\pi) \tag{4.3}$$

$$X = 2kL\cos^2(\beta/2) \tag{4.4}$$

$$\sqrt{X} = \sqrt{2kL}|\cos(\beta/2)| \tag{4.5}$$

$$F(a) = \int_a^\infty d\tau \exp(-j\tau^2) \tag{4.6}$$

$$= \int_a^\infty d\tau \cos(\tau^2) - j\int_a^\infty d\tau \sin(\tau^2) \tag{4.7}$$

Next, the error of GTD coefficient near the diffraction boundary is compared with the diffraction coefficient given by UTD as shown in Fig.4.3. This will determine the range of applicability of GTD in the hard wall imaging. Given the target at angle 315^o, the phase of diffraction coefficient is plotted by scanning incident angle from 45^o to 135^o. The phase error between GTD and UTD is small as long as the incident angle is less than 90^o. It means that, as long as the incident angle is not so large that target is close to shadow boundary (Fig.4.2), the GTD diffraction coefficient has a small phase error. In the HWRI problem, transmitting/receiving antenna array is assumed to be placed with incident angle smaller than 90^o. Thus, the impact of phase error is not significant in most cases and the GTD approximation is sufficiently accurate for modeling wave propagation.

Furthermore, the study on the total field in edge diffraction is carried out to give more insights into the limitations of imaging problem [25]. The total electric field is simulated with FDTD algorithm and the snapshots of the field distribution at steady state are presented in Fig.4.4. The field distribution in the shadow region of the wall looks like the distribution excited by the new source at the location of the sharp plane edge. In another word, no matter how many antenna elements are placed in front of the hard wall, the illumination of the objects behind the wall is equivalent to the case with two antenna elements. The placement of more antenna elements does not introduce the same additional benefit as a

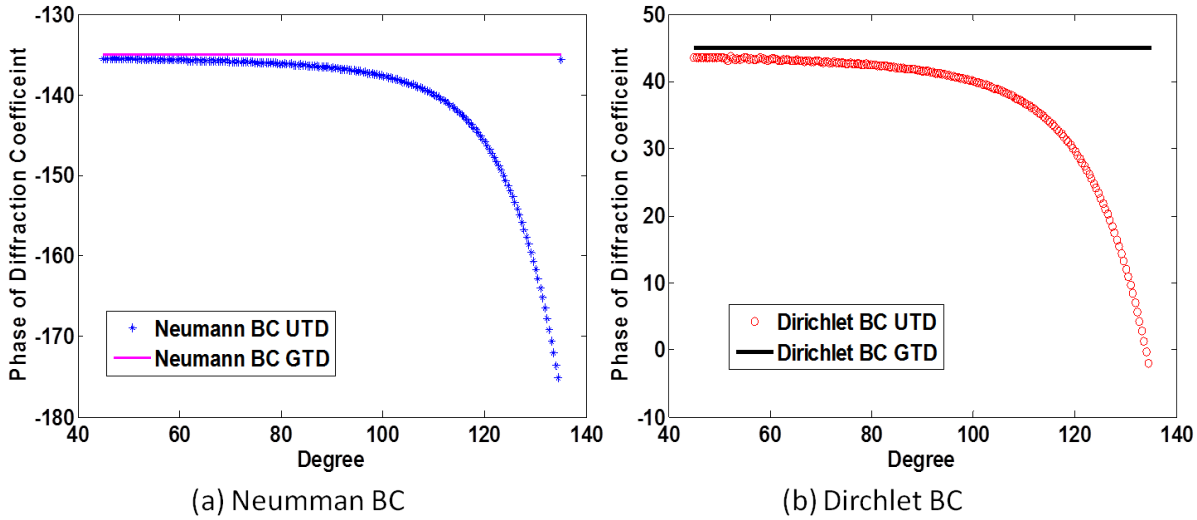

Figure 4.3: Phase of diffraction coefficient vs. incident angle: (a) Neumann Boundary (b) Dirichlet Boundary

normal scenario. The field distribution also implies that the number of incident waves onto objects depends on the number of edges instead of the number of array elements, while the number of incident wave directly determines the resolution of objects. Its impact on imaging algorithms will be discussed in the following sections.

4.2.2 Discussions on Time-Reversal DORT and MIMO Imaging System

In previous studies [42] and [101], time reversal imaging technique DORT (Decomposition of Time-Reversal Operator) was utilized with the new multiplicative array processing and entropy focusing technique. The time-reversal DORT imaging is developed to overcome the multipath propagation and achieve selective focusing on the target. The time reversal operator is obtained from multistatic data matrix (MDM), which is the round-trip interelement response between two array elements. The eigenvalue decomposition of time reversal operator gives the signal subspace corresponding to each target in image space. The study of HWRI starts with time reversal DORT, and the details will be presented in the Section 4.3.

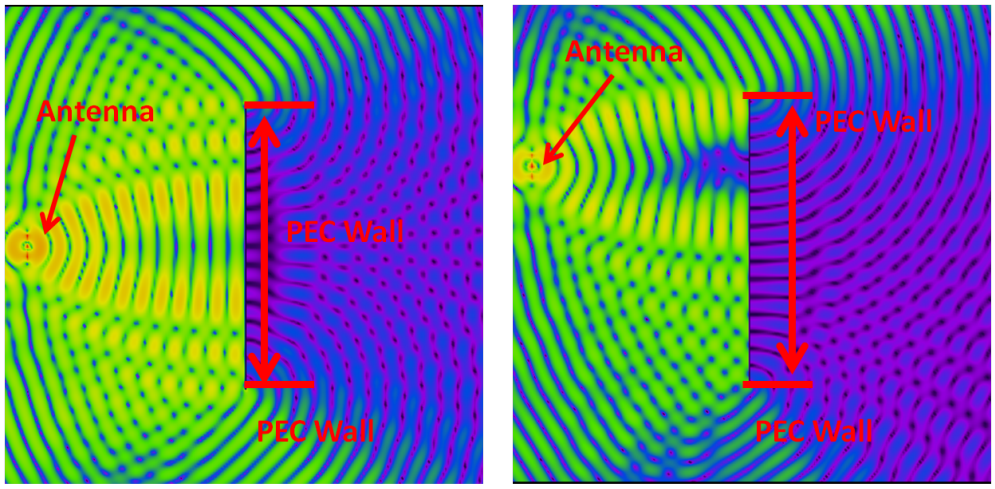

(a) Antenna at Center (b) Antenna off Center

Figure 4.4: Field Distribution Excited by Antenna Element Located (a) At the Symmetric Axis of The Wall (b) Off the Symmetric Axis of The Wall

The collection of MDM requires simultaneous transmit/receive operation of antenna elements and the omnidirectional antenna radiation pattern. The low gain of antenna element leads to the mixing of target responses with the responses of clutters at the same range. Also, as the signal of interest experiences the edge diffraction twice, the signal is greatly attenuated by diffraction and the signal-to-clutter ratio (SCR) is exacerbated furthermore. For this reason, although the DORT technique works for imaging targets in complex medium, it is not robust for HWRI with inescapable low SCR.

For the aforementioned reasons, the transmitting antenna and receiving antenna are to be separated to have different radiation pattern for reception and probing: the transmitting antenna should have higher gain and narrow beamwidth while receiving antenna should have low gain and wide beamwidth. This configuration is similar to the distributed MIMO radar (widely separated MIMO bistatic radar). In this configuration, the transmitting antennas of MIMO radar are widely separated to obtain the spatial diversity of the target's radar cross section (RCS), as the transmitting antennas in such system are spaced distantly such that each of them views a different aspect (RCS) of the target. The well-studied distributed

MIMO radar emits the energy isotropically in space and achieves the directivity at the stage of signal processing, rather than the energy focusing onto targets, whereas, in our system, the high gain transmitting antenna is exploited to deliver more energy incident onto the targets behind the hard wall. Besides, the conventional MIMO system radiates the linear independent (orthogonal) waveforms at transmitting array, while, in our system, this orthogonal waveform is not exploited as the radar system operates with probing pulse of stepped sweeping frequency.

4.2.3 Wave Propagation Model

In this chapter, the hard wall imaging is simplified into a 2D problem as in Fig.4.5 It will be shown that the 2D simplification turns the vector field into the scalar field and results in the fast computation of diffraction coefficient. The experimental results imply that the 2D assumption preserves a good accuracy in localizing the objects. The multiple targets detection is explored and the Fig.4.5 illustrates the two target imaging case. Two high gain transmitting antenna has its main beam pointing at the edge of a hard wall. This design choice maximizes the signal strength incident on the objects at the given output power at the transmitter. It is noted that because of high antenna gain, the signal out of transmitter is diffracted via one edge at each time.

The backscattered signal received at $\vec{r}_n$ due to the transmitting antenna at location $\vec{r}_n$ is normalized to probing wave at frequency of ω and expressed as in Eq(4.8).

$$s_{nm}(\omega) = \sum_{d=1}^{D} g(\vec{r}_n, \vec{r}_d, \omega) x_d(\omega) g(\vec{r}_m, \vec{r}_d, \omega) + n(\omega) \tag{4.8}$$

where x_d is the scattering coefficient due to d_{th} target (assuming isotropic scattering coefficient) and $g(\vec{r}_n, \vec{r}_d)$ and $g(\vec{r}_m, \vec{r}_d)$ are the Green's functions (diffraction and multiple return path effects are both included) from the n_{th} transmitting antenna to d_{th} target and m_{th} receiving antenna to d_{th} target, respectively. $n(\omega)$ is the Gaussian white noise. If the geomety of imaging scenario in Fig.4.5 are used for modeling, the forward transmission propagation can be decomposed into the product of free space Green's function, diffraction

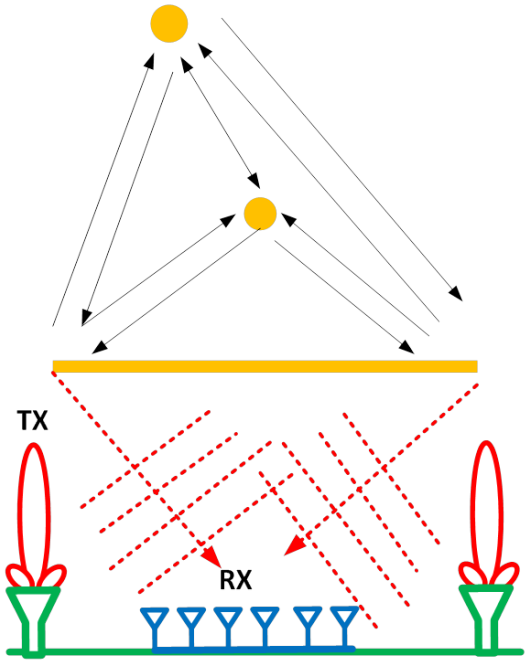

Figure 4.5: Hard Wall Imaging imaging Scenario scenario with Distributed distributed MIMO Radar radar Configurationconfiguration

coefficient and diverging factor. Eq.(4.9) and (4.10) show the forward propagation from transmitting antenna 1 and 2, respectively.

$$g(\vec{r}_1, \vec{r}_d) = \frac{\mathrm{e}^{-jkl_{i1}}\mathrm{e}^{-jkl_{t1}}}{4\pi l_{i1}} D(\theta_{t1}, \theta_{i1}) \sqrt{\frac{l_{i1}}{l_{t1}(l_{t1}+l_{i1})}} \tag{4.9}$$

$$g(\vec{r}_2, \vec{r}_d) = \frac{\mathrm{e}^{-jkl_{i2}}\mathrm{e}^{-jkl_{t2}}}{4\pi l_{i2}} D(\theta_{t2}, \theta_{i2}) \sqrt{\frac{l_{i2}}{l_{t2}(l_{t2}+l_{i2})}} \tag{4.10}$$

Similarly, the backscattered wave propagation can also be modelled with two return paths.

$$g(\vec{r}_m, \vec{r}_d) = \frac{\mathrm{e}^{-jkl_{i1}}\mathrm{e}^{-jkl_{t1}}}{4\pi l_{i1}} D(\theta_{t1}, \theta_{i1}) \sqrt{\frac{l_{i1}}{l_{t1}(l_{t1}+l_{i1})}} + \frac{\mathrm{e}^{-jkl_{i2}}\mathrm{e}^{-jkl_{t2}}}{4\pi l_{t2}} D(\theta_{t2}, \theta_{i2}) \sqrt{\frac{l_{i2}}{l_{t2}(l_{t2}+l_{i2})}} \tag{4.11}$$

where the operator D is the equation of diffraction coefficeicnt. Fig.4.6 denotes the parameters in the above equations. The angles θ_{t1} and θ_{t2} are diffraction angle observed at the

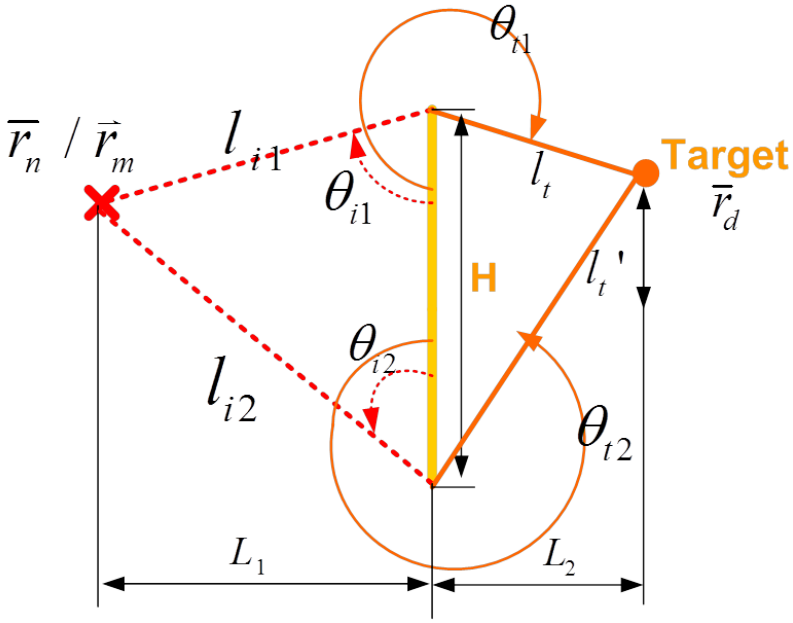

Figure 4.6: Illustration of Two Dimensional Geometry of HWRI Problem

target corresponding to edge 1 and edge 2, respectively. The angles θ_{i1} and θ_{i2} are the incident angle from the antenna to the sharp planar edge corresponding to edge 1 and edge 2, respectively. The distance l_{i1} and l_{i2} are the distance between antenna and the edge 1 and edge 2, respectively. The distance l_{t1} and l_{t2} are distance between the target and the edge 1 and edge 2, respectively. The wave propagation model gives us the insights into hard wall radar imaging and is especially useful in the future construction of steering vector.

4.3 Initial Study with Time Reversal DORT Imaging

The study of HWRI problem is carried out with modified time reversal DORT method in [42]. In this section, the imaging process is briefly described with the emphasis on the difference between experimental and analytical methods. Then experimental results will be presented in the following subsection.

4.3.1 Imaging Process of Modified Time Reversal DORT Imaging

The time reversal DORT Imaging is based on the collection of multistatic data matrix(MDM) **K**. **K** is a symmetric matrix and its entry k_{ij} is the signal received at the i_{th} antenna where the signal is emitted from the j_{th} antenna and reflected by the target. Since the propagation medium is reciprocal, the round-trip propagation response can be decomposed into the one-way response by taking singular value decomposition (SVD) of MDM or eigenvalue decomposition of time reversal matrix. The time reversal matrix is given as follows.

$$\mathbf{T} = \mathbf{K^H K} \tag{4.12}$$

The subspace decomposition of **T** gives the signal subspace $\vec{v}_s$ and noise subspace $\vec{v}_n$. In time reversal DORT, the signal subspace $\vec{v}_s$ is used for selective focusing on the target by choosing the corresponding eigenvector. In our experiment, only one target is placed behind the wall, so the signal subspace has only one eigenvector, which is corresponding to the largest eigenvalue $\vec{v}_1$ and called dominant eigenvector.

Once we obtain the eigenvector and the eigenvalue, we can then obtain the image by using the steering vector $\vec{g_s}$, focused on the search point $\vec{r}_s$. If the steering vector is Green's function for the problem, then the wave will be focused on the target. In general, however, we may not know the exact Green's function without some knowledge of the problem. The steering vector is obtained using the knowledge of experiment geometry similarly as what has been done in wave propagation modeling. In simplified 2D problem, there are two steering vectors: one is for left diffraction edge ($\vec{g}_{s,left}$) and the other is for right diffraction edge ($\vec{g}_{s,right}$).

In conventional TR-DORT imaging, we first obtain the multistatic data matrix and the eigenvector without the knowledge of the geometry of the problem. Then we construct the steering vector based on the prior knowledge of the problem. With the eigenvector $\vec{v}$ and the steering vector g_s, we construct the imaging function Ψ, which is equivalent to numerical

back-propagation of electromagnetic waves.

$$\Psi(\vec{r}_s) = \frac{1}{2\pi} \int_{\Delta\omega} d\omega U(\omega) < \mathbf{g_s}(\vec{r}_s, \omega), \mathbf{v}_1(\omega) > \tag{4.13}$$

However, the image function doesn't give a maximum at the location of target as we expect because of the phase ambiguity of eigenvector. In numerical eigenvalue decomposition, the complex eigenvector is not equal to the desirable one-way response between array element and target due to the introduction of the arbitrary phase term [20,96,101]. The consequence of this term is that the image function does not focus at the location of target. The phase term is dependent on the initial guess of numerical iteration and is impossible to be estimated.

$$\mathbf{v}_1 = \mathbf{v}_{ideal} e^{-j\omega T_0} \tag{4.14}$$

The solution to this method arises from the observation of physics of wave propagation. From Eq.(4.15), we can find that the expression of time reversal image function is actually the time instant of numerical backpropagate electric field at t=0 since $I(\omega)$ is the numerical backpropagate electric field at frequency domain.

$$i(t)|_{t=0} = \int d\omega e^{i\omega t} I(\omega)|_{t=0} = IFT\{I(\omega)\}|_{t=0} \tag{4.15}$$

where $I(\omega) = U(\omega) < \mathbf{v_1}, \mathbf{g_s} >$.

The impact of arbitrary phase term from numerical decomposition is the shift of focused electric field image to an unknown time instant T_0. Now the problem is how to find out the shifted time frame. Based on the time reversal principle, the electric field will focus at the location of the target as demonstrated in [20]. This chapter demonstrates a way to find out the time frame in which the energy of electric filed is concentrated at the location where the target is. In this minimum-entropy method, the value of image function at each search point is the value of a pixel in the time domain snapshots of the electric field. The wave focusing is equivalent to a "well-ordered" image that is the image entropy is minimized. The well-ordered image is taken as the desirable image with a maximum value at the location of

the target.

$$H(t) = -\sum_{All(x_s,y_s)} p(x_s, y_s, t)\ln(p(x_s, y_s, t)) \tag{4.16}$$

where $p(x_s, y_s, t) = \psi(\vec{r}_s, t)/\max(\psi(\vec{r}_s, t))$ and ln denotes the natural log operator.

Moreover, the image function has to be modified to improve the resolution by using multiplicative array technique as discussed in our previous chapter [101]. But there is a difference between experimental method and analytical method. The multiplication will be done in time domain instead of the operation of image function as follows.

$$\Psi_{right}(\mathbf{v}_1, \omega) =< \mathbf{v}_1, \mathbf{g}_{si,right} > \xrightarrow{IFT} \psi_{right}(\vec{r}_s, t) \tag{4.17}$$

$$\Psi_{left}(\mathbf{v}_1, \omega) =< \mathbf{v}_1, \mathbf{g}_{si,left} > \xrightarrow{IFT} \psi_{right}(\vec{r}_s, t) \tag{4.18}$$

$$\psi(\vec{r}_s, t) = \psi_{right}(\vec{r}_s, t) * \psi_{right}(\vec{r}_s, t) \tag{4.19}$$

It is noted that, although the modified image function in time domain is not numerical backpropagate field anymore, the entropy law still preserves according to our extensive observations. As shown in Fig.4.7(a) and (b), at t=0, the image is disordered while at $t = T_0$, $H(t)$ is minimized and the image shows that the electric field focused at the target.

4.3.2 Experimental Results of Initial Study

The TR-DORT imaging system is built with Bowtie slot array as transmit/receive array in an anechoic chamber. The MDMs in the frequency domain of two cases (with the target and without target) are downloaded from the network analyzer. The subtraction of two cases suppresses the clutter reflections and keeps the target scattering only. Since the antenna array is oriented as a 1D linear array, the problem is simplified to the 2D problem. Then the time-gating function is used to further gate out the subtraction residue of the wall. The remaining is the response due to diffracted backscattering field and clutters close to target. The eigenvalue decomposition is applied to the gated multistatic matrix, and this further removes noise and clutters. The image functions in time domain can be obtained from Eq.(4.19). It is found that the initial time frame gives a disordered image, which is the same

as the result from conventional image function in frequency domain. If the image entropy along possible ranges is plotted as in Fig.4.7(c), the minimum can be found at $t = T_0$.

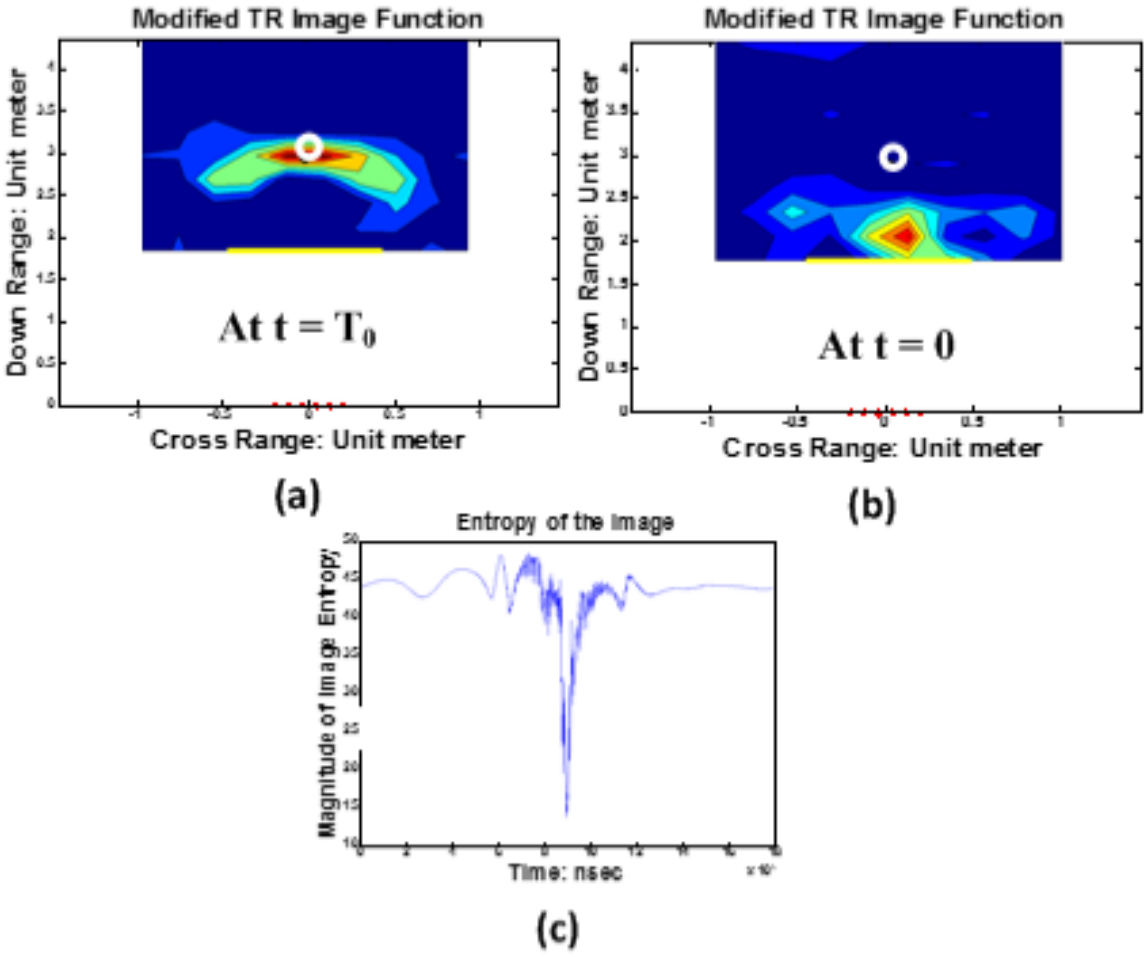

Figure 4.7: (a)Time Domain Image at t=T_0 (b)Time Domain Image at t=0 (c)Image Entropy

Furthermore, the modified TR-DORT based imaging algorithm is applied to two cases with a target at a different location. Fig.4.8 shows that the target location is correctly localized. However, the resolution of the image is poor because noise and clutter response cannot be sufficiently suppressed with subspace decomposition and time gating. To achieve a better estimation of signal subspace, the SCR and SNR have to be sufficiently improved with high gain transmitting antenna array. This leads to our further improvement of imaging

system into distributed MIMO configuration in the following sections.

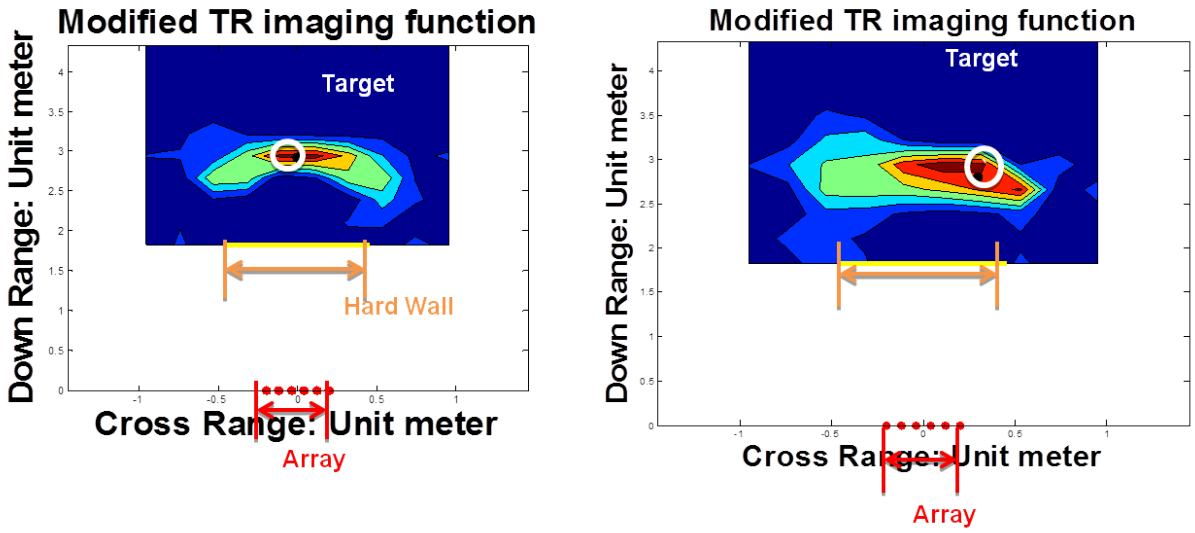

Figure 4.8: Imaging Result (a)Target at (x, y)=(0,2.75m)(b)Target at (x, y)=(-0.32m, 2.81m)

4.4 MIMO Radar Imaging System

The radar system can be described in three parts: the RF hardware, the antenna array, and the data acquisition unit. The block diagram of the MIMO radar system is developed based on the Vector Network Analyzer as shown in Fig.4.9. The core of this system is a range-gated Stepped Frequency Continuous Wave (SFCW) radar device that transmits stepped frequency from 1.5 to 3.5 GHz with an output power of 20 dBm.

4.4.1 Antenna Array

In this distributed MIMO radar configuration, transmitting antenna and receiving antenna array are separated. The illuminating antenna is made of WR430 Horn antenna as a high gain antenna. The transmitting antenna array is widely separated traverse to the hard wall, and the main beam of each element is pointing towards each edge of the hard wall.

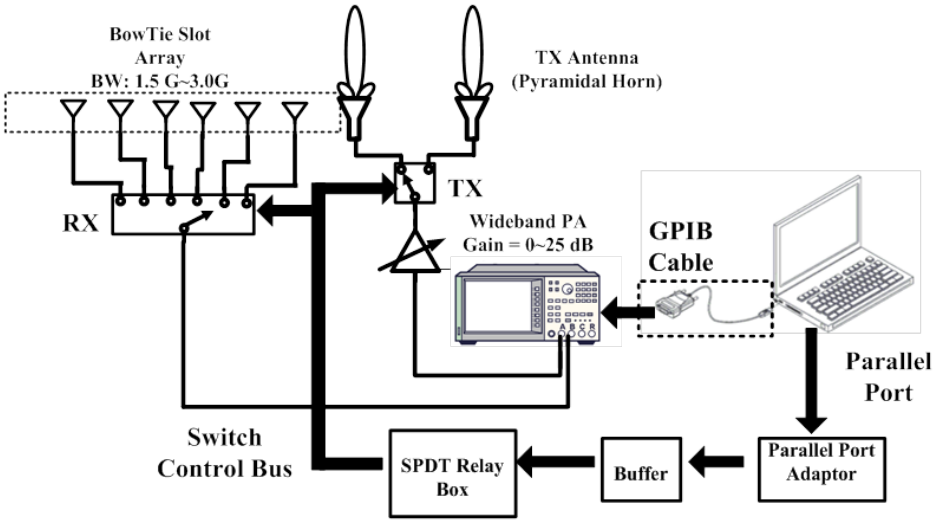

Figure 4.9: Distributed MIMO Radar Imaging System based on Vector Network Analyzer

On the receiver side, the Bowtie slot antenna is chosen as an omnidirectional element and closely spaced. A double layer PCB (IS640) is used to fabricate antenna array as shown in Fig.4.9. The center-to-center spacing of antenna element is 65mm, $0.65\lambda_h$ of the highest frequency. The antenna element is placed on an absorber layer to suppress the radiation to the backside without the degradation of the radiation pattern.

The performance of this Bowtie slot array is shown as in Fig.4.11. The radiation patterns in E plane and H plane have broad beam while the gain over frequency is flat enough to operate from 1.5 GHz to 3 GHz.

4.4.2 RF Hardware and Data Acquisition

Our radar imaging system is based on the vector network analyzer(VNA), which can generate the stepped frequency continuous wave (SFCW). The tones (single frequency) from 1.5 GHz to 3 GHz are scanned one by one. This imaging system gives the frequency domain complex interelement matrix in Eq.(4.9) in the scanned frequency range. In free space, the down range resolution is determined by the bandwidth of the scanned frequency range and estimated as $\Delta r_d \cong \frac{c}{2B} = 0.1m$ while the conventional estimation cross range resolution from

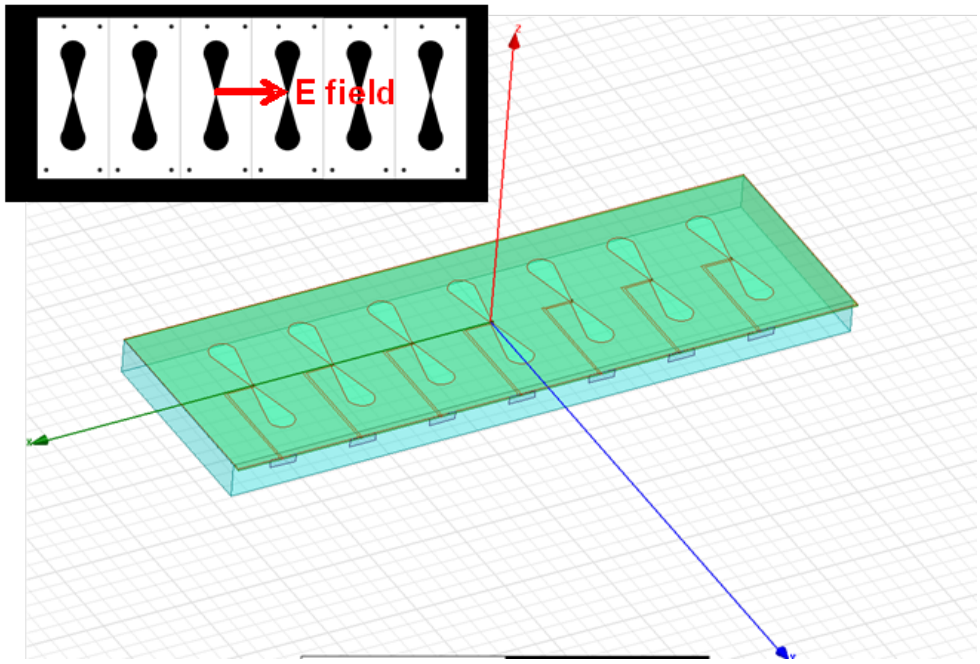

Figure 4.10: Bowtie Slot Antenna Array

beamwidth is not applicable in our imaging scenario. The frequency step usually determines the maximum unambiguous range in free space, while, in our problem, the magnitude of diffraction signal is the factor that limits the maximum range of detection.

The network analyzer is configured to the measurement of S21 and the directional coupler at the port two is bypassed to improve the noise figure as it is not used in the S21 measurement. The output from this VNA system is complex frequency response at RF frequency instead of the baseband signal in normal radar. The complex response is downloaded to PC for signal processing via GPIB cable. The microwave multiplexing switches are driven by the computer program via digital control units and enable us to select the elements of transmitting and receiving array.

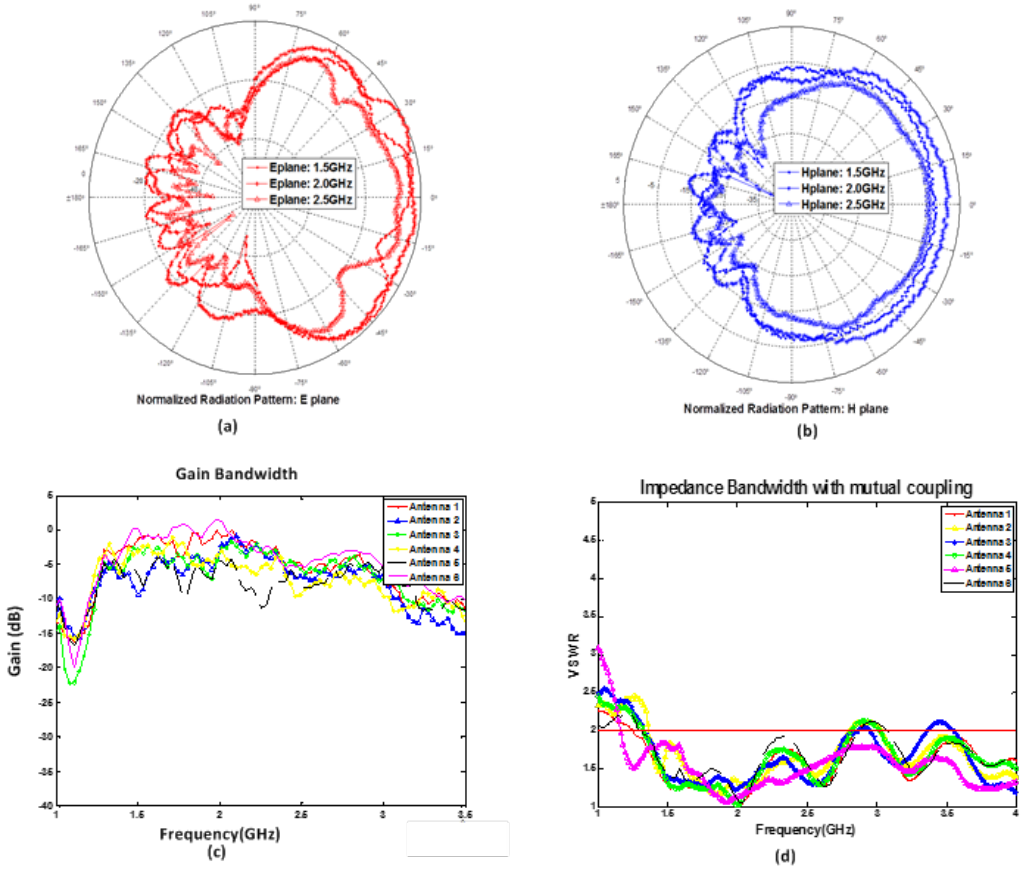

Figure 4.11: Bowtie Slot Antenna Array Performance with absorbing material as substrate (a) E plane Pattern (b) H plane Pattern (c) Gain bandwidth (d) Impedance bandwidth (VSWR)

4.5 MIMO Radar Imaging Algorithm

The MIMO radar system has been studied extensively and proposed to localize the targets as a more powerful system. Distributed MIMO radar system has transmitters and receivers widely separated to view different aspects of targets. The Direction of Departure (DoD) and Direction of Arrival (DoA) can be estimated from the same set of measurements. The geometry relationship given by DoD and DoA gives the location of targets. Moreover, the time of arrival (ToA) is also useful to find the range of targets and further identify the location of

targets. However, this method is not useful in HWRI problem as the DoA of all targets is determined by the direction of edges. For this reason, we have to modify the algorithm for MIMO radar imaging as follows.

The interelement response matrix is collected on each sensor array element, which gives the covariance matrix. Firstly, the DoA estimation from covariance matrix is achieved MUSIC(multiple signal classification) technique and, as a result, the geometry of hard wall is determined for the construction of steering vector. Secondly, the adaptive cancellation technique is applied to suppress the interference terms in the image function due to the multipath of backscattering. Finally, after having obtained the round-trip steering vector from the estimated geometry of imaging scenario and geometric theory of diffraction (GTD), the model-based image function is re-formularized to a bistatic mode for outputs of adaptive nulling receive array.

4.5.1 Direction of Arrival Estimation

In the two-dimensional simplified HWRI system, the backscattered wave from multiple objects arrives at the receive array from two deterministic directions as shown in Fig.4.12. The estimated DoA determines the geometry of conducting wall is critical for adaptive receive array pattern formation to suppress the interference from multiple path backscattering.

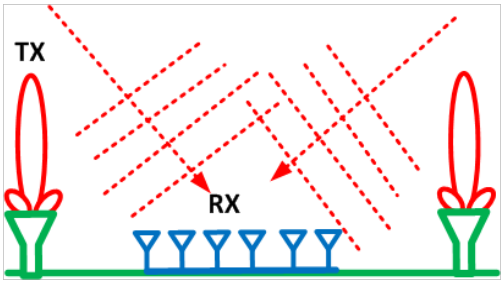

Figure 4.12: Direction of Arrival Estimation

$$\mathbf{Y}(\omega) = \begin{bmatrix} s_{11} & s_{12} \\ s_{21} & s_{22} \\ \cdots & \cdots \\ s_{61} & s_{62} \end{bmatrix} \tag{4.20}$$

$$\mathbf{R}_Y(\omega) = \mathbf{Y}\mathbf{Y}^H \tag{4.21}$$

$$f(\theta) = \frac{1}{\mathbf{a}^H(\theta)\mathbf{V}_N\mathbf{V}_N{}^H\mathbf{a}(\theta)} \tag{4.22}$$

where $\mathbf{a}(\theta) = [1, e^{-jkd\sin\theta}, ..., e^{-jk(N-1)d\sin\theta}]$ The covariance matrix $\mathbf{R}_Y$has been com-

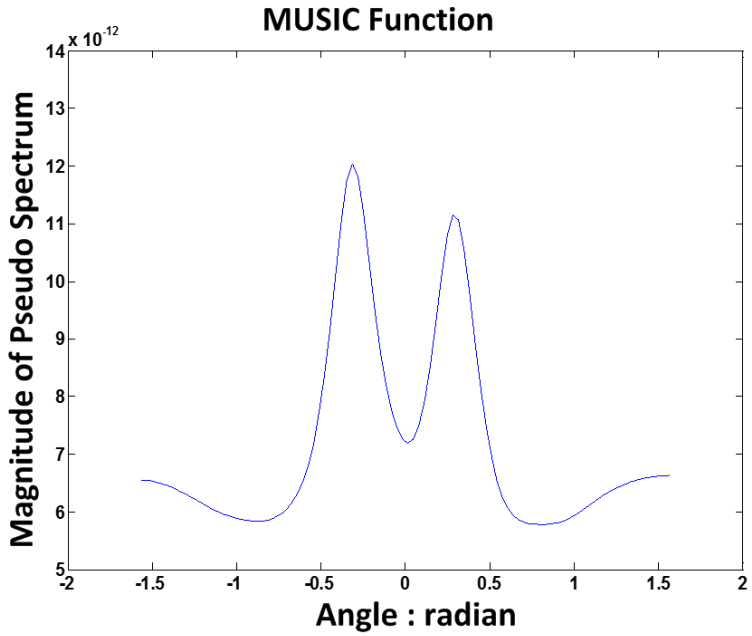

Figure 4.13: Direction of Arrival Estimation

puted from collected data , and MUSIC is applied to give the two arrival angle of incoming waves. Then the eigenvalue decomposition is applied to the covariance matrix to obtain the null space, and the null space is substituted into the pseudo spectrum function in Eq.(4.22). The plot of $f(\theta)$ in Fig.4.13 over the angle of $-\pi/2$ to $\pi/2$ gives two peaks which corresponds to the two directions of arrival (DoA).

4.5.2 Adaptive Receive Array for Interference Suppression

As discussed in [42], the image function is the integral of the inner product between steering vector and signal subspace. In this chapter, it is analytically shown that the inner product gives an interference term due two propagation paths. However, the interference terms will be increasingly complicated if multiple targets are to be imaged. For this reason, the adaptive nulling technique is employed in this subsection to enable the receiving array "see" the signal from only one direction of arrival at each time as in Fig.4.14. The weight of each received signal is adjusted, and the weighted outputs are summed to give a steered beam pattern. The inset of Fig.4.14 shows that the receive gain over varying incoming directions given by time delayed receiving phased array beamforming technique in Eq.(4.25). For the incoming wave

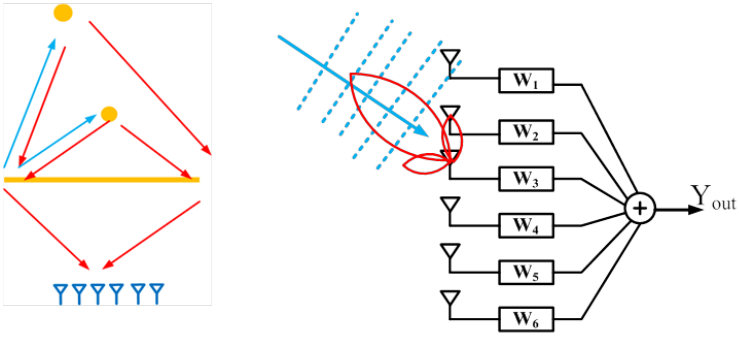

Figure 4.14: (a) Illustration of two return path (b) adaptive receive phased array

from first DoA, the wave from the second DoA leads to interference effets. The weighting vector is given by the time delay at each array elements. For example, if the first column of measured data matrix is used and the summed output that has only backscattered wave from one direction is obtained as in Eq.(4.25).

$$s_{out1}(\omega) = \sum_{n=1}^{N} S(n,1;\omega) w_{n1}(\omega) \tag{4.23}$$

$$w_{n1} = \exp(j\omega\tau_{n1}) = \exp[jk(n-1)d\sin(\theta_{DOA,1})] \tag{4.24}$$

$$\tau_{n1} = (n-1)d\sin(\theta_{DOA,1})/c_0 \tag{4.25}$$

Similarly, the second column can be weighted to cancel the interference term and amplify the desirable term. The Fig.4.15 shows a group of time domain analytical data with backscattering from two targets. It illustrates that original data has incoming waves from two directions and generates two peaks of arrivals corresponding one target. In conventional imaging technique, these two peaks will be treated as backscattering of two targets and results in ghost image. It has been shown that only signal from one desirable direction remains after interference cancellation, in Fig.4.15. Then the weighted output can be employed for image reconstruction using image function.

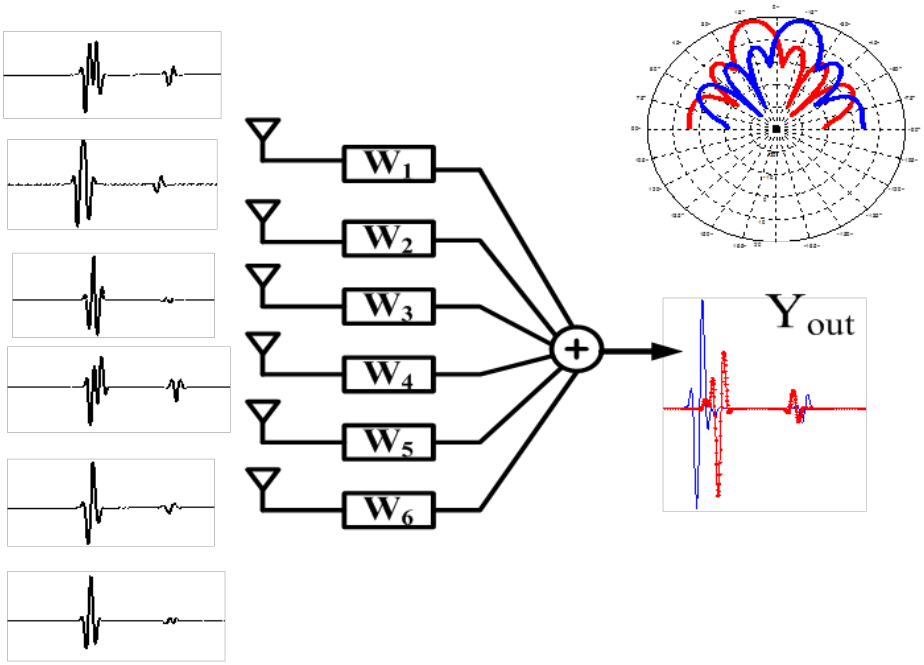

Figure 4.15: Illustration of adaptive cancellation: The received signal at each element is weighted to steer the beam towards the direction of one diffraction edge and suppress the signal from the other direction. The inset polar plot shows the synthesized power pattern of the output with different weights from Eq.(4.25. The red output corresponds to the pattern (red) pointing at the direction of -18^o while the blue output corresponds to the pattern (blue) pointing at the direction of 16^o

4.5.3 Localization on with Multiplicative Array Signal Processing

The measured data is time gated to remove the subtraction residue of wall so that the remaining is the response due to diffracted backscattering field and residues of clutters. The wave propagation model is exploited to construct steering vectors used in image function in (4.29) and (4.30). The element in steering vector $g_s(\vec{r}_m, \vec{r}_n, \vec{r}_s)$ represents the response between the transmitting element at $\vec{r}_n$ and receiving element at $\vec{r}_m$ with reference to the search point at $\vec{r}_s$. The expression of steering terms for transmitting path ($g_{st}(\vec{r}_n, \vec{r}_s)$)and receiving path ($g_{sr}(\vec{r}_0, \vec{r}_s)$) are demonstrated in (4.26) and (4.27) respectively while the round trip steering terms are the product of receiving and transmitting steering terms as in (4.28). It is noted that the output of phased array is the weighted sum of observed signals at all receiving elements ($\vec{r}_n$) so the receiver location used in receiving terms is replaced with the geometric center of receiving array ($\vec{r}_0$). This effective receiver location gives a very good focused image at target location as shown in Fig.4.16.

$$g_{st}(\vec{r}_n, \vec{r}_s) = \frac{e^{-jkl_{in}} e^{-jkl_{sn}}}{4\pi l_{in}} D(\theta_{sn}, \theta_{in}) \sqrt{\frac{l_{in}}{l_{s1}(l_{sn} + l_{in})}} \tag{4.26}$$

where n = 1 or 2

$$\begin{aligned} g_{sr}(\vec{r}_0, \vec{r}_s) = & \frac{e^{-jkl_{i1}} e^{-jkl_{s1}}}{4\pi l_{i1}} D(\theta_{s1}, \theta_{i1}) \sqrt{\frac{l_{i1}}{l_{s1}(l_{s1} + l_{i1})}} \\ & + \frac{e^{-jkl_{i2}} e^{-jkl_{s2}}}{4\pi l_{i2}} D(\theta_{s2}, \theta_{i2}) \sqrt{\frac{l_{i2}}{l_{s2}(l_{s2} + l_{i2})}} \end{aligned} \tag{4.27}$$

$$g_s(\vec{r}_0, \vec{r}_n, \vec{r}_s) = g_{st}(\vec{r}_n, \vec{r}_s) g_{sr}(\vec{r}_0, \vec{r}_s) \tag{4.28}$$

The inner product between the two columns of measured data, which are corresponding to the received signal from each transmitting antenna, and the two entries of steering vector are integrated over frequency span and the integrals yield two image functions (4.29 and

4.30).

$$\begin{aligned}\psi_1(\vec{r}_s) &= \int_{\Delta\omega} d\omega[g_s^*(\vec{r}_0, \vec{r}_1, \vec{r}_s)s_{out1}(\omega)] \\ &= \int_{\Delta\omega} d\omega[g_s^*(\vec{r}_0, \vec{r}_1, \vec{r}_s)\sum_{n=1}^{N} s(n,1;\omega)w_{n1}(\omega)\end{aligned} \tag{4.29}$$

$$\begin{aligned}\psi_2(\vec{r}_s) &= \int_{\Delta\omega} d\omega[g_s^*(\vec{r}_0, \vec{r}_2, \vec{r}_s)s_{out2}(\omega)] \\ &= \int_{\Delta\omega} d\omega[g_s^*(\vec{r}_0, \vec{r}_2, \vec{r}_s)\sum_{n=1}^{N} s(n,2;\omega)w_{n2}(\omega)\end{aligned} \tag{4.30}$$

where the angles θ_{s1} and θ_{s2} are diffraction angle observed at the search point corresponding to edge 1 and edge 2, respectively. The distance l_{s1} and l_{s2} are distance between the target and the edge 1 and edge 2, respectively.

As discussed in [42], these two image functions (4.29) and (4.30) yield two semi-circles with two edge points as their own centers. Because the electric field is distributed as a cylindrical wave excited at the edge point, this is equivalent to the range detection with single UWB wide beamwidth antenna, which has a good down range resolution but poor cross range resolution. The conventional radar system improves the cross range resolution by the use of phased array with beam scanning and the conventional multistatic imaging system achieves image focusing by superimposing multiple circles with slight phase shift given by multiple receiving elements. However, both of these techniques are not applicable to HWRI problem. For this reason, the multiplicative array signal processing is applied to the two images and gives a focused image on the targets [42].

$$\psi(\vec{r}_s) = \psi_1(\vec{r}_s) \times \psi_2(\vec{r}_s) \tag{4.31}$$

When it comes with the multiple targets detection, each target corresponds to one semi-circle. So there will be more than one semi-circle in each sub-image as shown in Fig.4.16(a) and (b). The range gating technique can be applied to selectively focus at the targets falling into desired detection range as in Fig.4.16(c) and (d).

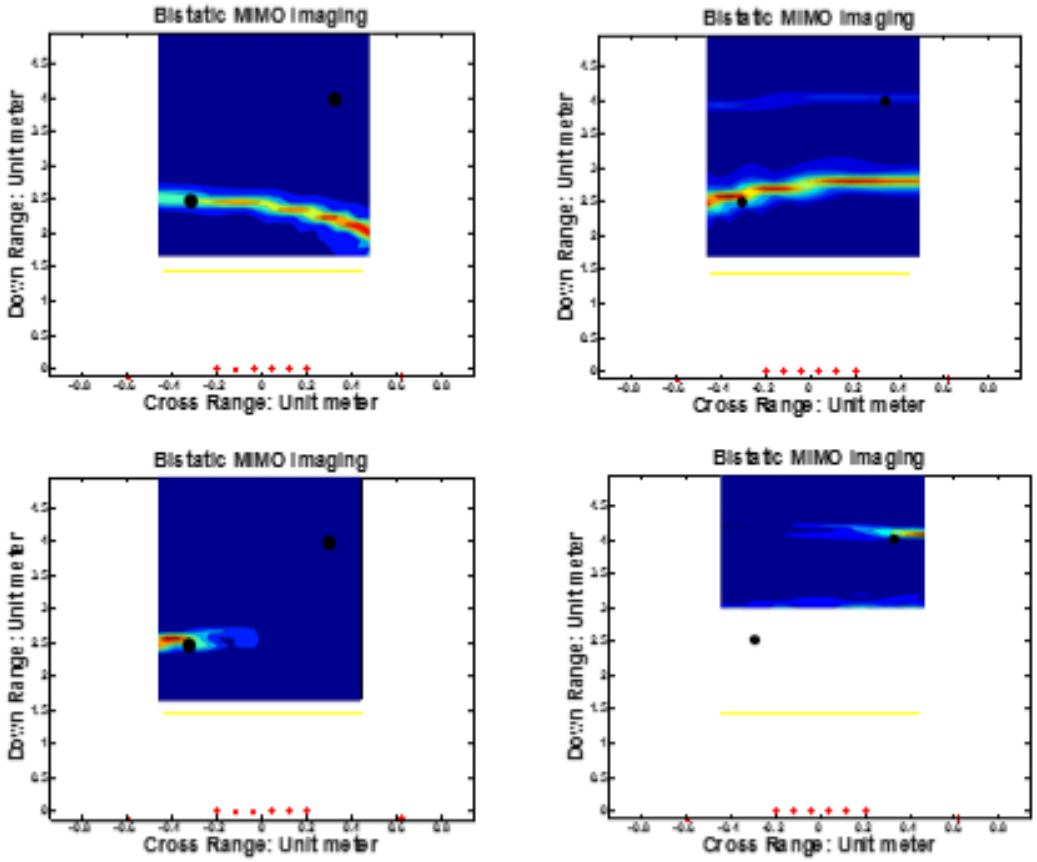

Figure 4.16: Numerical example: (a) image from (4.29), (b) image from (4.30), (c) range gated image from (4.31), (d) range gated image from (4.31). Note: the image of farther target is overridden by the image of closer target in (a) and (b). The total image is range gated over the possible range of each target to focus at the targets in the gating range.

4.6 Discussion and Experiment Results

The analytical and numerical results have demonstrated a good performance of our imaging algorithm in HWRI. To study more practical effects, the experiment has been carried out in Anechoic Chamber. The experiment procedures and results will be presented following with some discussions on findings in this section.

The hard wall is made with a double layer PCB placed on a platform, whose supporting pod is shielded by absorber and the two targets are two metallic cylinders to generate Mie

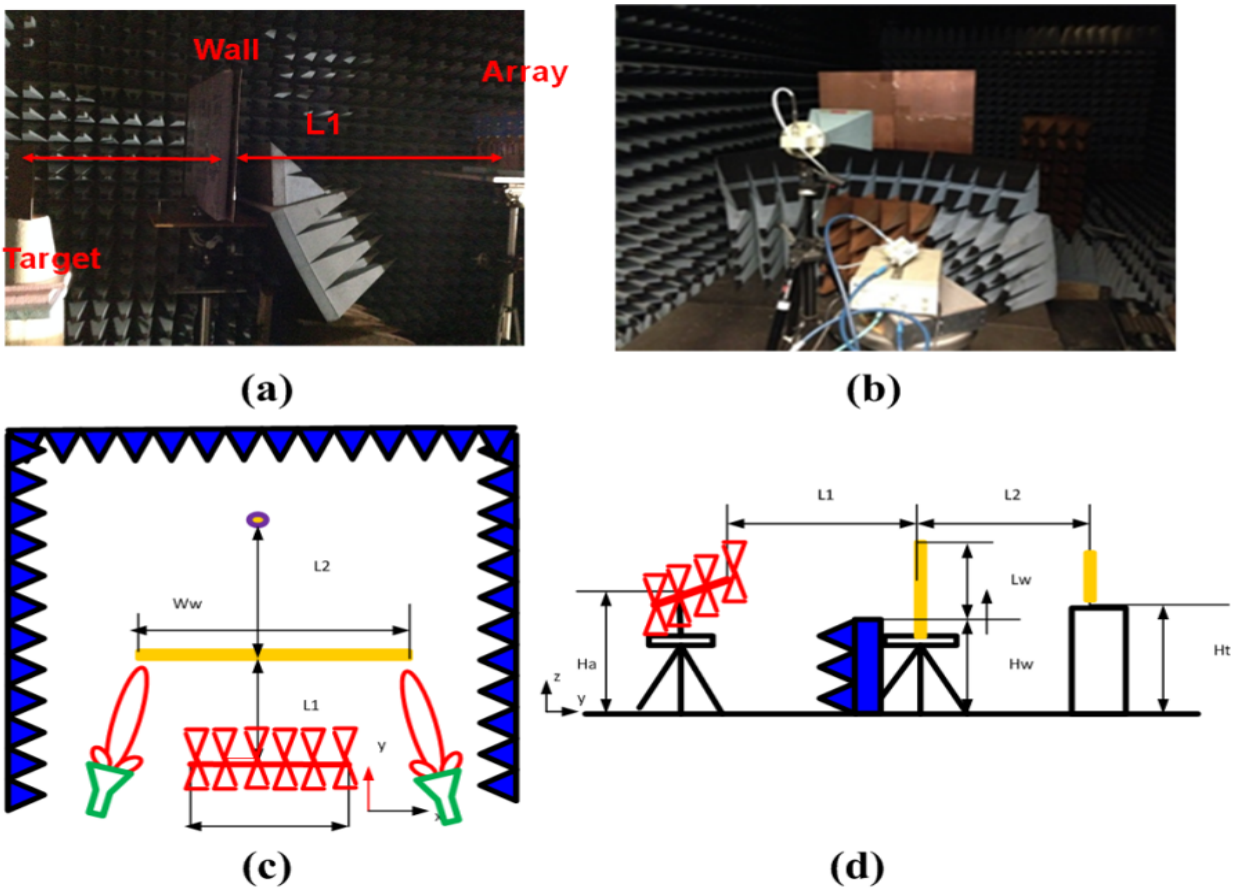

Figure 4.17: (a)Experiment in anechoic chamber (b)Top view of experiment (c)Side view of experiment

scattering at this frequency.

4.6.1 Experiment Procedures

The signal processing flow has been summarized in Fig.4.18. Prior to the start of measurement with targets, the step of calibration has to be carried out to shift the initial time or phase origin to the phase center of radiation and reception. The aluminum sphere is placed at a known location without hard wall or any other obstacles. The differential measurement is taken and the interelement matrix is recorded. The calibration matrix is obtained by using the knowledge of target location and stored for future calibration in hard wall imaging

experiment as in (4.32), (4.33) and (4.34).

$$\begin{aligned}
\mathbf{S}_{cal,total}(\omega) &= \begin{bmatrix} s_{11,tot} & \cdots & s_{16,tot} \\ s_{21,tot} & \cdots & s_{26,tot} \end{bmatrix} \\
\mathbf{S}_{cal,inc}(\omega) &= \begin{bmatrix} s_{11,inc} & \cdots & s_{16,inc} \\ s_{21,inc} & \cdots & s_{26,inc} \end{bmatrix} \\
\mathbf{S}_{cal,diff}(\omega) &= \mathbf{S}_{cal,total} - \mathbf{S}_{cal,inc} \\
&= \begin{bmatrix} s_{11,diff} & \cdots & s_{16,diff} \\ s_{21,diff} & \cdots & s_{26,diff} \end{bmatrix}
\end{aligned} \tag{4.32}$$

As we are operating in bistatic mode, the antenna coupling can be neglected if the time gating is used. We can predict the expected response ( ) using Green's function.

$$\begin{aligned}
s_{cal,diff,mn}(\omega) &= s_{TX,mn}(\omega) s_{exp,mn}(\omega) s_{RX,mn}(\omega) \\
&= s_{TXRX,mn}(\omega) \frac{\exp(-jk(l_m + l_n)}{(4\pi)^2 (l_m + l_n)}
\end{aligned} \tag{4.33}$$

The calibration matrix is computed as in (4.34).

$$s_{TXRX,mn}(\omega) = \frac{s_{cal,diff,mn}(\omega)}{s_{tar,mn}(\omega)} \tag{4.34}$$

After the calibration, the hard wall is placed in between the target and TX/RX array without the presence of targets, and the background interelement matrix is measured in the frequency domain. Next, the hard wall imaging measurement is carried out with the targets placed behind the wall, and the difference of the cases with and without target gives the differential matrix. In this way, the weak diffracted signal can stand out of the clutter response. However, the residues of subtraction still contaminate the measurement a lot. For this reason, the time gating technique is implemented to gate out not only the subtraction residues but also the multiple scatterings as (4.35) and (4.36).

Firstly, a gating since function is convolved with calibrated data and then first (Nf-1)/2

and the last (Nf-1)/2 elements in convolved result are dropped.

$$
\begin{aligned}
&s_{diff,gated,initial}(\omega) = s_{diff,cal}(\omega) \otimes G_1(\omega) \\
&G_1(\omega) = \frac{N_f * t_{span}}{t_{\max}} sinc(\frac{(\omega - \omega_c) * t_{span}}{2}) e^{(} - j\omega t_c) \\
&\omega = 2\pi f \text{ (Frequency is from 1.5GHz to 3GHz)} \\
&t_{span} = \text{span of gating time} \\
&t_c = \text{center of gating time} \\
&t_{max} = \frac{N_f - 1}{BW} \\
&N_f\text{: number of frequency points}
\end{aligned}
\tag{4.35}
$$

Secondly, the post-normalization technique is used to compensate the initial gated result due to sharp frequency transition.

$$
s_{diff,gated}(\omega) = \frac{s_{diff,gated,initial}(\omega)}{U_{gated1}(\omega)} \tag{4.36}
$$

where $U_{gated1}(\omega) = U(\omega) \otimes G_1(\omega)$ $U(\omega)$ is a unit vector with the same length as initial measurement data.

The time gating function is used instead of time windowing because it is operating in frequency domain so that it does not introduce ripples in the frequency domain responses. In addition to these pre-processing steps, the imaging algorithm can be applied to the data for post-processing and the imaging results are presented in next subsection.

4.6.2 Experimental Results

The experimental results are presented in Fig.4.19 and can be compared with the numerical results. We can find that the image from experimental measurement has some ghost spots The ghost spots in the total image $\psi(\vec{r}_s)$arise from the blurred image in $\psi_1(\vec{r}_s)$ and $\psi_2(\vec{r}_s)$. The blurred images of $\psi_1(\vec{r}_s)$ and $\psi_2(\vec{r}_s)$ shows the ripples in between two targets as shown in Fig.4.19(a) and (b). These ripples in 2D image are also shown in the range profile as in Fig.4.21. As discussed in the next subsection, these ripples result from the multiple scatterings between two targets, which are impossible to be eliminated.

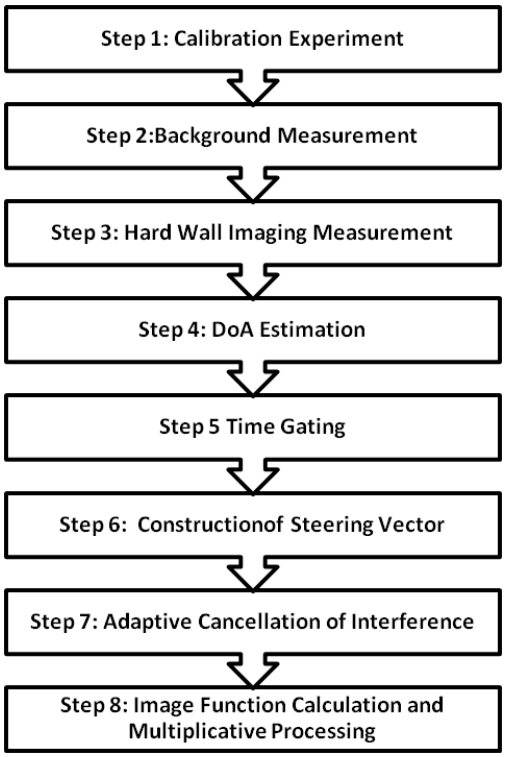

Figure 4.18: Flow chart of signal processing

The multiple scatterings between wall and targets limit the minimum distance between them because of two reasons. If the targets are too close to the wall, the incident angle of direction is small and thus the diffraction coefficient is weak. Besides, the targets echoes will be overlapped by the responses from multiple scatterings. The multiple scattering between two targets limits the minimum resolvable distance between two targets. If the two targets are too close to each other, the multiple scatterings overlap with the target echoes and leads to the false detection as shown in Fig.4.21(a). In contrast, Fig.4.21(b) presents the well-resolvable case that the distance between two targets and the distance between wall and targets are sufficiently large so that they are separable in the time domain.

In our proposed method of the multiplicative array, the two sub-images are multiplied with each other to generate the image of targets. The operation of multiplicative is possible to make the blurred region of two sub-images stand out as shown in Fig.4.19(c) than

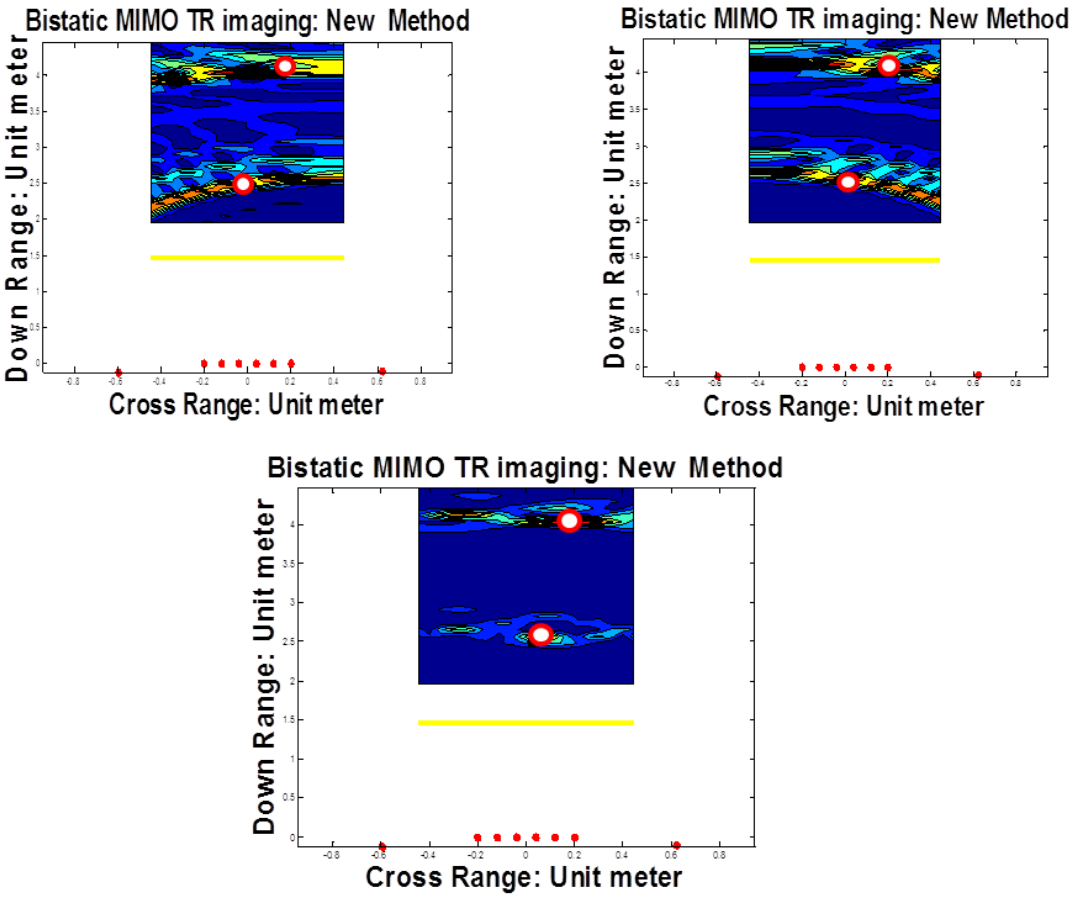

Figure 4.19: Experimental Results: (a) image using Eq.(4.29) (b) image using Eq.(4.30) (c) image from Eq.(4.31). The multiple scatterings arise from two sources: (1) the multiple scatterings between two targets and (2) the multiple scatterings between the two targets and hard wall as shown in Fig.4.21

conventional image function with the operation of summation. Therefore, the range gating is required to remove the multiple scattering between targets and hard walls. However, if two targets are two close to each other, the ripples from multiple scatterings leads to the several ghost spots and the location of true targets is impossible to be found. In the case with well-resolvable targets, this magnitude of the multiple scatterings will be much smaller than the backscattering from targets and our imaging algorithm provides a very accurate localization of targets with low possibility of false detection.

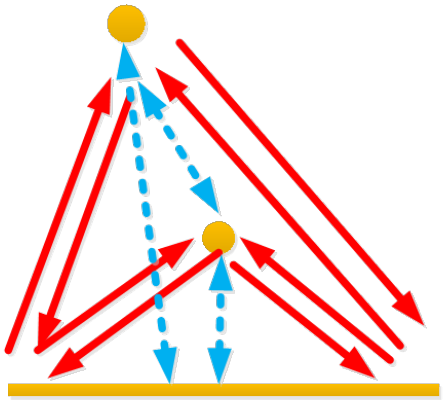

Figure 4.20: Multiple scatterings in experiment: dashed lines denote multiple scatterings, solid lines denote backscattering to be processed for image reconstruction

4.6.3 Future Improvements

In 2D case, we are facing the problem of the false pair. In Fig.4.22, we can readily find that the observed echo given by real targets at A and B is the same as the two false targets at the location of C and D. Generally, apart from the true locations, N*(N-1) possible target locations are false alarm at most for an N target detection case. For this reason, for multiple target case, the other dimension of information is required to exclude the false pair. For example, the receiving array is made into a 2D array to make use of the diffraction from top/bottom edge. This leads to our future research direction of HWRI with 2D receiving array. Furthermore, the multipath propagation, such as the reflection from clutters or boundary, is helping to improve the detection of objects. Nevertheless, the complexity of constructing analytical Green's function is more and more challenging with the introduction of irregularly shaped objects in the image space. The numerical simulation tools are one possible way to approach the Green's function by including all major objects in the image space.

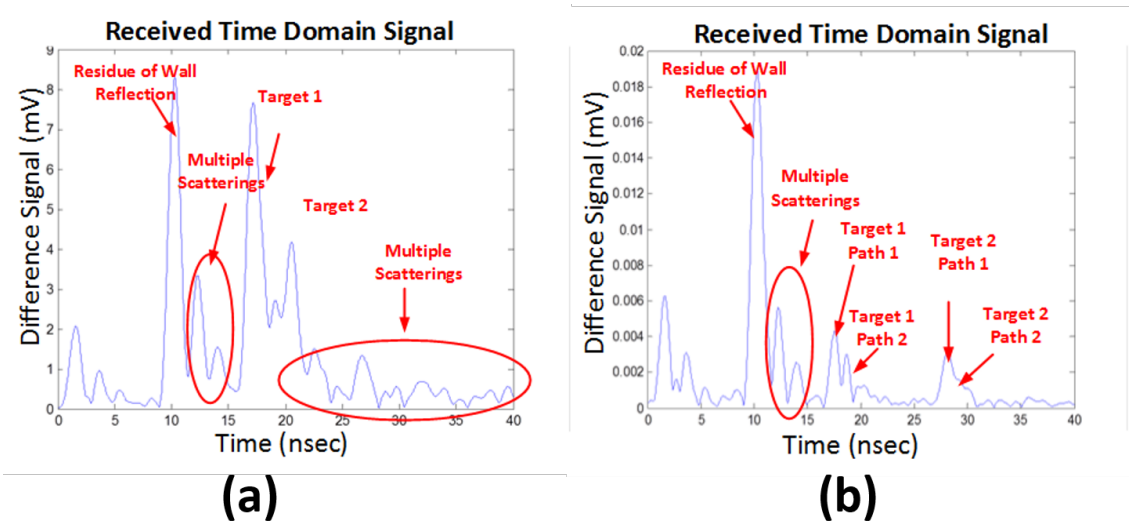

Figure 4.21: Measurement in time domain:(a) unresolvable targets (b) resolvable targets

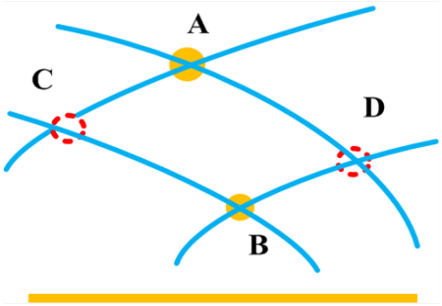

Figure 4.22: Illustration of false pair problem

4.7 Conclusion

This chapter presents a new radar imaging problem called Hard Wall Radar Imaging (HWRI) in contrast with the conventional Through-the-Wall Radar Imaging(TWRI). The research starts with time reversal DORT(Decomposition of Operator) imaging algorithm, which is powerful in a multipath problem like HWRI. Through the experimental study on TR-DORT, it has been found that this algorithm is limited by the huge difference between experiment environment and numerical study. The observed signal by multistatic radar is highly cor-

rupted by the noise and clutter reflections.

For this reason, the signal-to-clutter and signal-to-noise problem of HWRI are resolved by improving our microwave imaging system. The distributed MIMO configuration is used with two pyramidal horn antenna as an illuminator and a six element linear-polarized planar Bowtie slot array as observers. The interelement response matrix is collected by controlling microwave multiplexing circuits, and the covariance matrix is thus constructed to obtain the Direction of Arrival (DoA) and the geometry of hard wall using MUSIC(multiple signal classification) technique. Next, the adaptive nulling technique is applied to suppress the interference terms in image function due to the multipath of backscattering. After having obtained the round-trip steering vector from the estimated geometry of imaging scenario and geometric theory of diffraction (GTD), the model-based image function is re-formularized to distributed configuration for outputs of the adaptive nulling receiving array. It has been shown that two resolvable point targets can be clearly localized for several cases. Moreover, the range resolution, the minimum distance between objects, and physical limitations of classifying object shapes are analyzed for this imaging scenario in addition to imaging results.

Chapter 5

A UNIDIRECTIONAL STACKED CROSS DIPOLE ARRAY FOR UWB MICROWAVE IMAGING APPLICATIONS

Two types of coplanar waveguide (CPW) fed wideband Bowtie slot antennas are designed for radar imaging using the array signal processing. The proposed antenna contains one crossed electric dipole layer stacking on the top of Bowtie layer, which cancels the back radiation by slot antenna. The layered stack-up enables the broadside flat panel array, which is favorable in the large volume manufacturing and production. Because of the wideband cancellation, the conducting reflector can be placed at the bottom to achieve the ultra-wideband (UWB) unidirectional radiation without degradation of an antenna performance. The measurement of V-pol antenna shows that a unit element has a return loss below -10dB from 1 GHz to 2.75 GHz and a 3dB gain bandwidth of 1.7 GHz. The cross-polarization level is measured to be below -20 dB for the whole operating band and the front to back ratio is better than 20dB depending on the size of the reflector. The 3dB beamwidth is more than 30^o to allow the observation of signal from a wider angle. By combining V-pol and H-pol antennas, we can create an antenna array for a polarimetric radar imaging.

5.1 Introduction

The electromagnetic wave (EM) at the low GHz range has unique advantages for microwave imaging including a lower attenuation in most media and a large diffracted waves caused by edges [101]. To create a sharp image. However, the radar system must have a large array size and a large bandwidth which may be difficult to obtain at a low frequency due to antenna limitation. The dispersive effects, such as a constant phase center and a smaller gain variation, have to be minimized to reduce its impact on radar imaging [89]. For this reason,

the design of UWB antenna array is the first challenge to implement a high-performance microwave imaging system.

There are several candidates for UWB antenna design as reviewed in [1]. Among these antenna structures, the Vivaldi and Bowtie antennas are known for their high polarization purity and low fabrication cost. The Bowtie antenna is suited for receive element due to its lower directivity [50]. The Bowtie slot antenna is complementary to Bowtie structure and can be modified to a single layer broadside radiator with coplanar waveguide [63]. However, the back radiation usually leads to the higher signal-to-clutter ratio as the signal from the backside is scattered by the clutters and electronic equipment. The conventional technique of placing a conducting reflector at a quarter-wave distance from the antenna will not work over a wide bandwidth.

The magneto-electric(M-E) design was initially proposed in [18] and improved to broadband unidirectional radiation in [58, 91] due to the back radiation cancellation (Fig.5.1). The formation of magnetic current in different structures has been demonstrated in several UWB antenna design [54, 92]. However, these UWB crossed dipole antennas achieve high performance at the expense of costly manufacturing and volumetric space [54]. Therefore, such design may not be suited for the low-cost radar imaging array antenna, which requires a uniform element performance, a simple manufacturing and a small unit spacing for beamforming. This paper presents a low-cost flat panel array design for microwave imaging applications based on similar M-E dipole principle.

5.2 Antenna Element Design

The antenna element design starts with the Bowtie slot antenna element without any M-E dipole technique. The Bowtie slot is similar to the CPW Bowtie slot [63] with rounded end [46], which provides a smaller in-band impedance variation and the consequent bandwidth extension. The slot antenna is fabricated on the high dielectric constant substrate Rogers Duroid 6006 ($\epsilon_r = 6.16$, thickness = 1.27mm). Since the lower frequency bound is

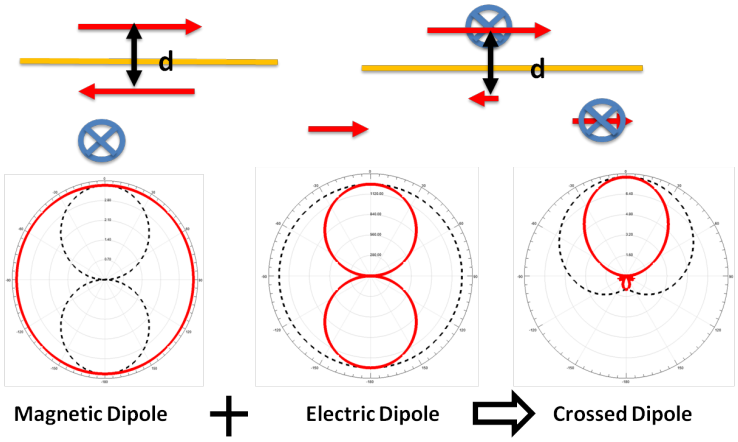

Figure 5.1: Illustration of M-E dipole cancellation: cross denotes magnetic dipole; arrow denotes electric dipole

determined by the length of Bowtie arm, the shorter guided wavelength in such a substrate can achieve the minimum frequency of 1GHz with limited unit size.

The unidirectional broadside radiation is also desirable for the imaging applications because the backward radiation often introduces a scattering from the unwanted clutters. Normally, a conducting reflector is placed at a distance of $\lambda_o/4$ (λ_o is the free space wavelength at the center frequency) from the radiating structure and results in a constructive interference in the boresight. However, this technique only works for the narrowband application because the reflector degrades the input matching over a wide bandwidth. This will be demonstrated in S11 data. Also, the gain bandwidth is degraded, because the constructive interference due to a reflector can only form at the center frequency. The standing wave formed between the reflector and the radiating structure is the culprit of the degradation of both gain and impedance bandwidth.

A remedy is proposed as M-E dipole technique [1, 58], which cancels the back radiation due to the two electric fields generated by the electric and the magnetic dipoles which are in phase on the front side and out of phase on the back side. It is well known that the slot structure can be modeled as a magnetic dipole. By stacking an orthogonal electric dipole on the magnetic dipole, the impact of the reflector can be minimized. The antenna structure is

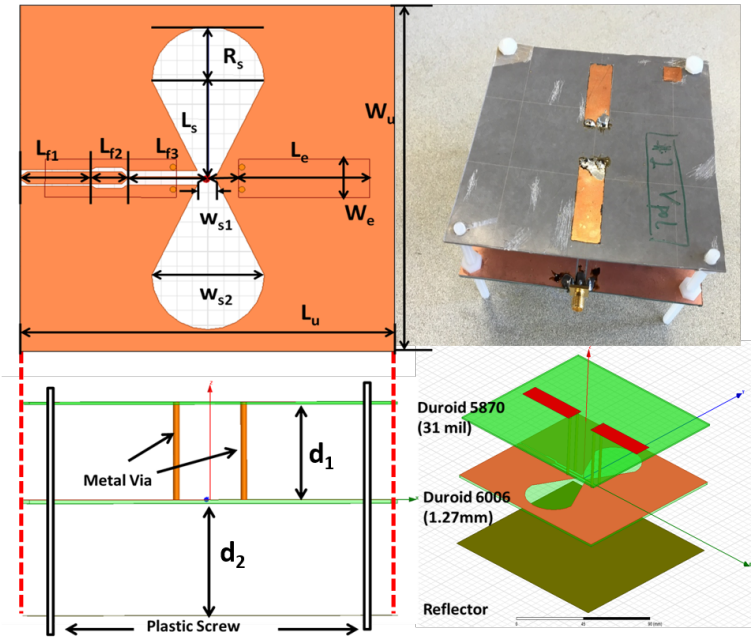

Figure 5.2: Geometry of proposed antenna element (V-pol) and layer stack-up

shown in Fig.5.2. The electric dipole is implemented on a low dielectric constant substrate Rogers Duroid 5870 ($\epsilon_r = 2.33$, Thickness = 31 mil). The electric dipole is made to be planar "fat" dipole with a length of 38 mm and a width of 13 mm, which ensures its broadband operation across the bandwidth. The two dipole arms are electrically connected to the bottom slot ground plane using metal wires and the two substrates are mechanically connected to the copper reflector plane of the same size using plastic screws at the four corners as in Fig.5.2.

The prototype of the V-pol antenna element is illustrated in Fig.5.2 with annotated design parameters. These design parameters are $W_{s1} = 2$ mm, $W_{s2} = 36$ mm, $R_s = 7$ mm, $L_s = 30$ mm, $L_e = 38$ mm, $W_e = 13$ mm, $L_u = 120$ mm and $W_u = 120$ mm. It is noted that the input SMA connector is fed to a slot through three sections of transmission lines(TL). The first CPW feed line is a 50 ohm TL with a length of 22.6 mm (L_{f1}), a width of 4 mm and a spacing of 0.8mm. The second CPW line is a quarter-wave transformer with a length

of 11.4 mm (L_{f2}), a width of 4 mm and a spacing of 1.5 mm. The third CPW line has a length of 22.54 mm (L_{f3}), a width of 0.8mm and a spacing of 2 mm. The vertices of Bowtie slot are rounded to minimize the in-band impedance fluctuation.

The dipole current will be canceled by the ground current if it is too close to the ground plane, while the current intensity on the dipole is too weak if it is too far away from the ground plane. So the distance between the electric dipole and the slot ground is optimized to be $d_1 = 32$mm. The distance between the slot ground and the reflector is around a quarter-wavelength of the center frequency ($d_2 = 37.5$mm) as commonly used for reflector placement.

5.3 Experimental Results and Discussions

The prototype of the proposed antenna structure is simulated by using the commercial EM simulator ANSYS HFSS. The V-pol antenna element has been fabricated with a laser milling machine and measured in a far field antenna measurement system. The measurement system downloads the results from vector network analyzer and is controlled by the automated positioning system in the anechoic chamber.

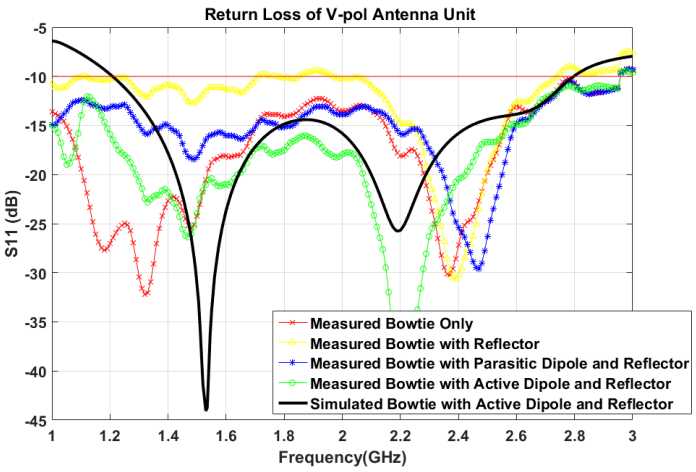

Figure 5.3: Measured and simulated S11 of V-pol antenna element in different conditions

5.3.1 Frequency Domain Results

Fig.5.3 shows the return loss (S11) of the designed Bowtie slot antenna element. Four different cases are shown to demonstrate the bandwidth extension due to the M-E dipole. The Bowtie slot antenna alone presents return loss lower than -10dB for the entire bandwidth from 1 GHz to 3 GHz (Bowtie Only in Fig.5.3). However, the placement of a reflector leads to the sharp peaking in the impedance and the consequent degradation of S11 (with Reflector in Fig.5.3). If the top single-layered planar dipole is placed without wiring to the bottom slot antenna, the electric dipole is weakly coupled to the slot antenna and results in the cancellation of the back radiation to some extent. Therefore, the parasitic dipole improves the impedance bandwidth (with Parasitic Dipole and Reflector in Fig.5.3). When the dipole is wired to CPW ground plane through four metal vias, the ground current flows to the electric dipole, which generates more radiation for back radiation cancellation (with Active Dipole and Reflector in Fig.5.3). As shown in Fig.5.3, the experimental data agrees with HFSS simulations. The comparison of the four cases demonstrates the principles of M-E dipole and how it improves the performance of Bowtie antenna. The boresight radiation over the operating frequency band is shown in Fig.5.4. The cross-polarization isolation is over 20dB for most of the operating frequency.

5.3.2 Time Domain Results

For some applications, the dispersion caused by a wideband antenna must be minimized. This is particularly true when a wideband antenna is used for the time-domain applications. The ultra-fast time-domain antenna measurement is still a challenging task. Because our lab does not have a calibrated time-domain measurement system, the time domain performance is simulated in HFSS transient, which is based on the Discontinuous Galerkin Time Domain methods. The excitation is a Gaussian pulse with a bandwidth of 1.5GHz to 3GHz. The time domain radiated electric field is observed in the far field at different angles in both E- and H-planes (Fig.5.6 (a) and (b)).

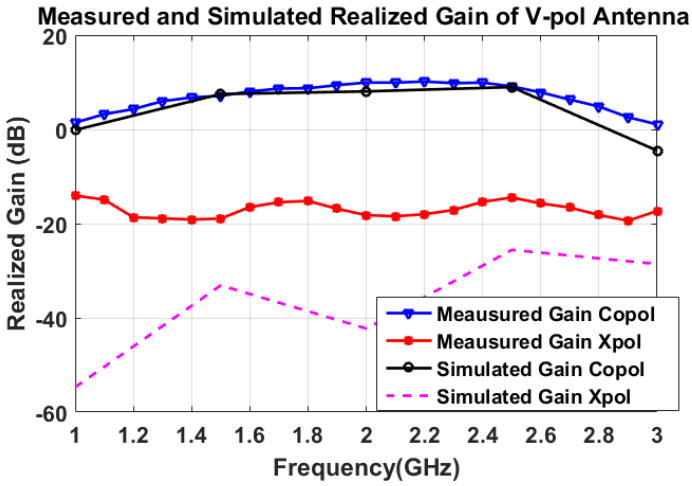

Figure 5.4: Measured gain of antenna element (V-pol) vs frequency

The fidelity factor (ρ) is a useful parameter to evaluate the distortion of the antenna. The fidelity factor is defined in Eq.5.1. The input signal is convolved with the far field radiated electric field after normalization. The fidelity factor is between 0 and one after normalization. The value 1 implies perfect electric field conversion without dispersion. The high fidelity factor is important in microwave imaging as the dispersive transducer results in the degradation of image resolution. Fig.5.7(a) shows the simulated results of fidelity factor at different angles in two orthogonal planes. It is noted that the magnitude of fidelity factor is greater than 0.85 for $-50^o < \theta < 50^o$ in both $\phi = 90^o$ and $\phi = -90^o$ planes.

$$\rho(\theta, \phi) = \max_{\tau} \int_{-\infty}^{\infty} \hat{s}(t)\hat{r}(t + \tau; \theta, \phi)dt \tag{5.1}$$

where $\hat{s}(t) = s(t)/(\int_{-\infty}^{\infty} |s(t)|^2 dt)^{1/2}$ and $\hat{r}(t) = r(t)/(\int_{-\infty}^{\infty} |r(t)|^2 dt)^{1/2}$. $s(t)$ is the input excitation signal of antenna and $r(t; \theta, \phi)$ is the radiated electric field at the angle of (θ, ϕ).

The group delay is another parameter that can be used for the evaluation of the time-domain performance. The group delay of the designed antenna is computed from the impulse response between input excitation and radiated electric field. From 1.5GHz to 3 GHz, the variation of the group delay is about 2 nsec as Fig.5.7(b).

5.3.3 H-pol Antenna Element Results

The H-pol antenna element is implemented by bending the feed line of the CPW antenna element (Fig.5.8(a)). This routing is required to create a unit cell with both the V-pol and the H-pol elements (Fig.5.9). Unfortunately, the discontinuity of the CPW feed results in spurious radiation at upper frequency. To mitigate this effect, the microstrip line is used as a feed line to connect to the SMA connector. The H-pol element has a worse impedance matching at the lower band due to the dispersion of the transition.

5.4 UWB Array and Microwave Imaging System

By combining the V-pol and H-pol antennas as one receive unit, a dual-polarized wideband imaging array system can be created. Fig.5.9 shows the proposed layout of the transmit and the receive array. The transmit array is built with the Antipodal Vivaldi antenna to illuminate the object in the image space. The decomposition of the observed EM field into two orthogonal components leads to a better classification of the object to be detected [97].

5.5 Conclusion

In this chapter, a stacked M-E dipole antenna element is presented and discussed for the microwave imaging application. This antenna element has a high cross polarization isolation and a wide bandwidth to enable the high-resolution polarimetric imaging algorithm. The CPW-fed Bowtie slot antenna element is stacked with the crossed electric dipole stacking on the top of Bowtie, to enable the conducting back reflector without affecting the antenna performance. The absence of the backside radiation will improve the signal-to-clutter ratio since the signal from the backside is often scattered by the walls and instrument. The stacking structure enables the flat panel array, which is desirable in the manufacturing and the production of the massive array.

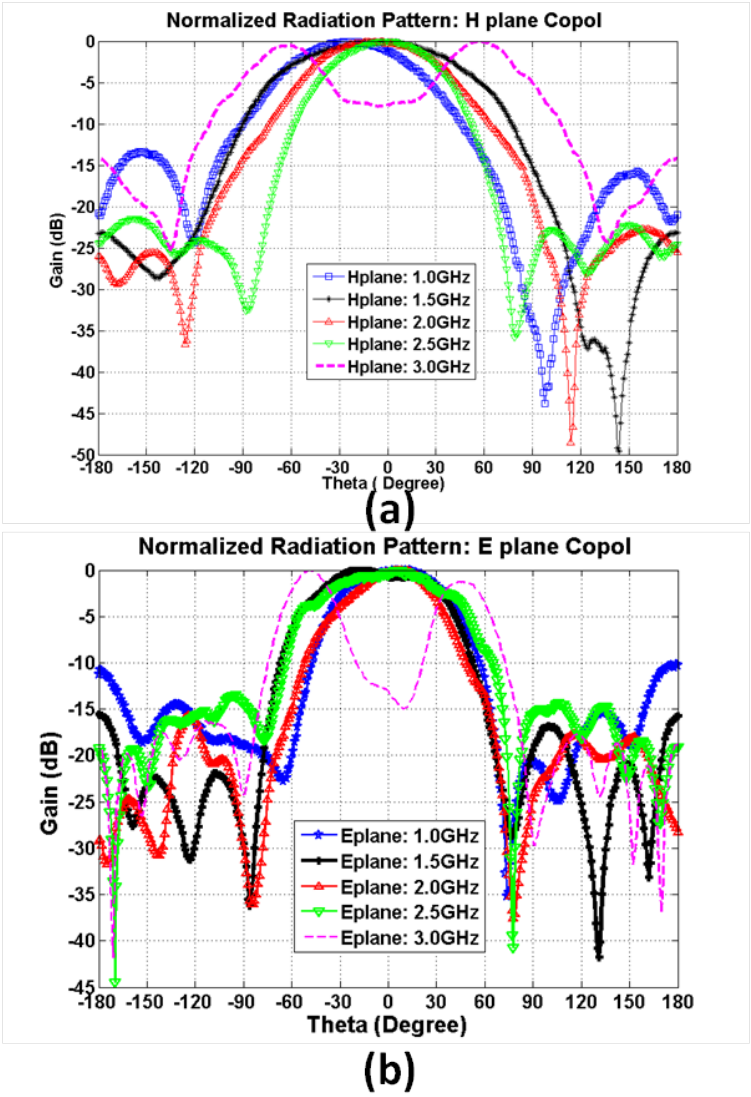

Figure 5.5: Measured radiation pattern of antenna element (V-pol) in E- and H-plane

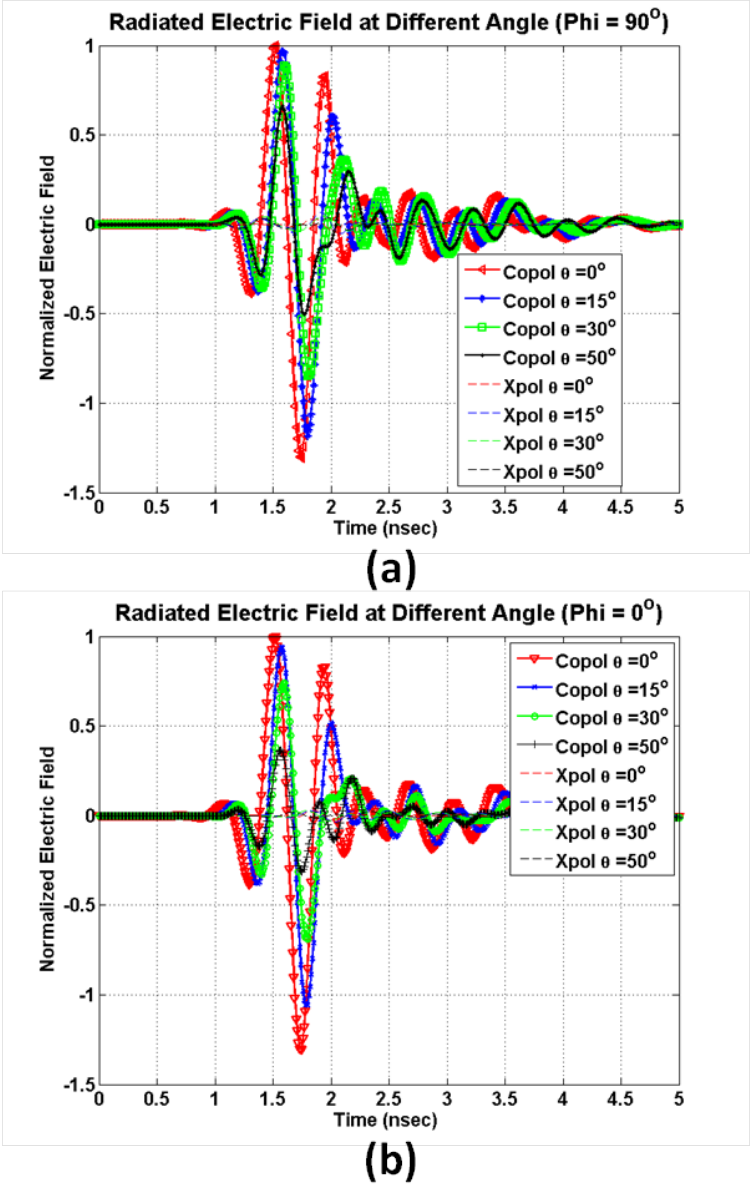

Figure 5.6: Simulated time domain radiated electric field in E-plane ($\phi = 90^o$ and H plane ($\phi = 0^o$)

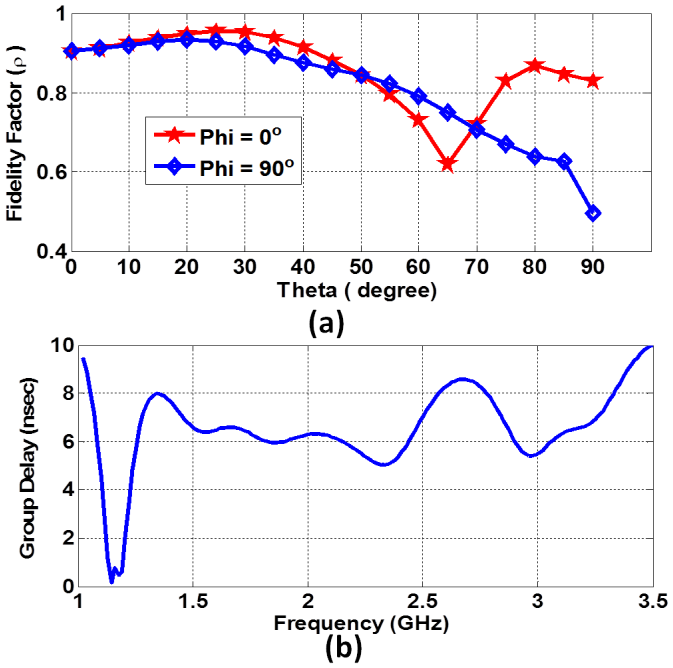

Figure 5.7: Simulated results in time domain: (a) Fidelity factor at different angles (b) Group delay

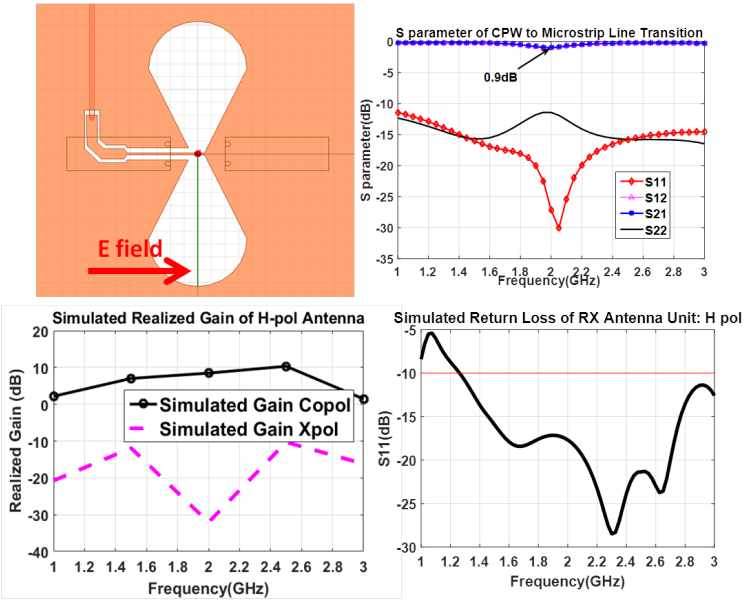

Figure 5.8: Simulted Performance of H-pol Antenna Eleemnt: (a) Top view of H-pol element design (b) S parameter of CPW to microstrip line transition (c) Realized gain (d) Return loss

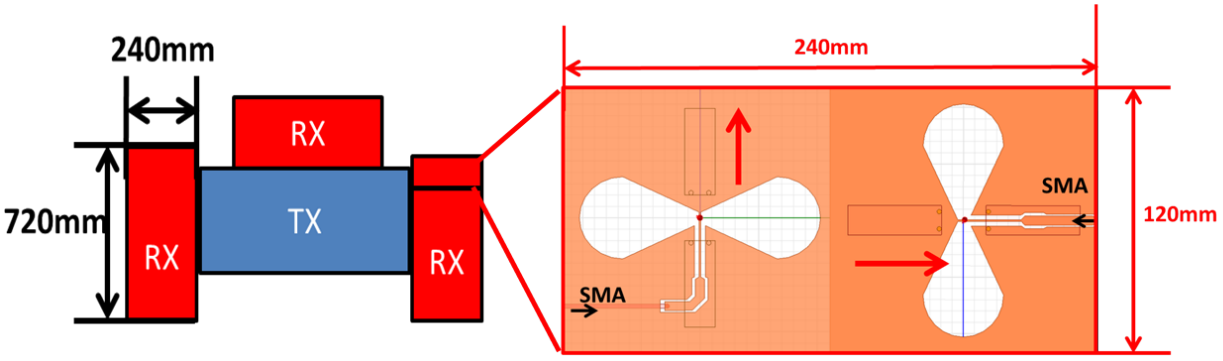

Figure 5.9: Microwave polarimetric imaging antenna array: the V-pol and H-pol antennas are used as a unit cell.

Chapter 6

FURTHER DEVELOPMENT

The development of a real-time and compact microwave imaging radar system is the next step of the continuing research. This new imaging system can be used in the scenario with both lossy dielectric wall and metallic wall as anti-imaging shielding. With the designed sensing system, the suspicious personnel or hazardous object shielded by the metallic wall in a building can be localized accurately. The simplified scene is illustrated in Fig.6.1. The combined technology can combat the shielding created by non-penetrating structures, in two possible cases. The first case (Fig.6.1(b)) is that the hard wall is located at a stand-off distance from the opaque dielectric wall, while the second case (Fig.6.1(c)) has hard wall embedded with the dielectric wall as a multilayered wall structure.

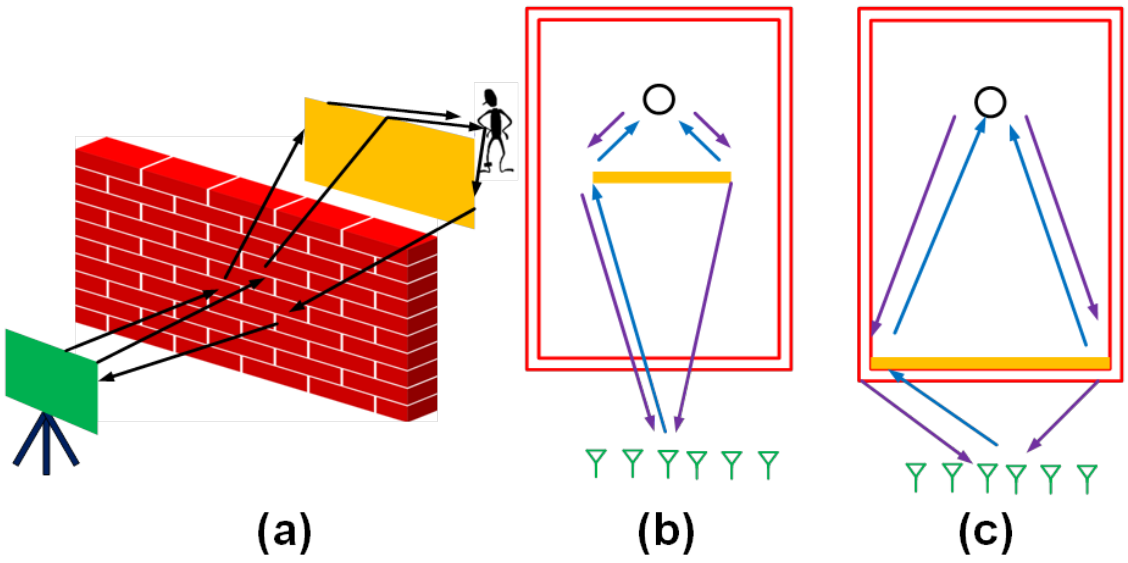

Figure 6.1: (a)Imaging of Shielded Suspicious Personnel in a Building (b) Case 1 (c) Case 2

6.1 Transmit/Receive Antenna Array

The solution to the false pair problem is the employment of diffracted field at more sharp edges. For this reason, the transmit antenna has to illuminate the all the sharp edges available in the scene of radar imaging. In most cases, the metallic wall stands on the ground, so the bottom edge of diffraction is not available. The top left and right edges diffract the backscattered signal from three different directions. The signal diffracted by three different edges are observed by the two-dimensional receive array described in Chapter 4. At the transmitter side, a beam steerable transmit array is required so that the transmit horn antenna can be reduced to a single one from the experiment setup and mechanical alignment error is also eliminated by using the electronically beam steering. The setup of the transmit/receive array are shown in Fig.5.9.

For the transmit array, the tapered slot antenna is a popular design to reach the requirement of wide scanning angle and cross polarization isolation, at the cost of the complicated assembly process and manufacturing. Derived on the tapered slot antenna, the antipodal Vivaldi design is devised to achieve the similar performance with double-layered PCB process as in Fig.6.2(b). However, either tapered slot antenna or antipodal Vivaldi are endfire radiating antenna, which is fragile and hard to manufacture. The Tightly Coupled Dipole Array (TCDA) (Fig.6.2(a)) has been studied extensively for its promise of making wide scanning angle and broadside radiating UWB antenna array as reported in [47]. In the future development, the TCDA is a more promising candidate to transmit antenna array than any other designs.

Also, our S-band antenna operates over a wide bandwidth and narrow beamwidth. For such as system, the beam squint can be enough to steer off of the target, resulting in a greatly reduced return. So the true time delay (TTD) module should be employed, instead of the conventional phase shifter. As shown in Fig.6.3, the flat panel transmit antenna with integrated balun is connected to the power divider feeding network to implement the passive fixed beam in the vertical direction and the steerable beam in the horizontal direction. This

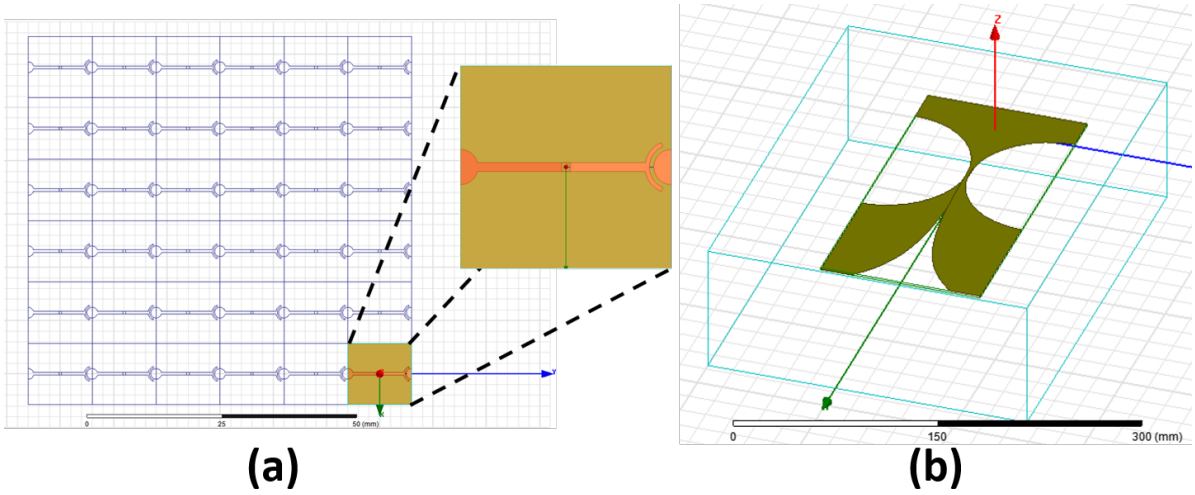

Figure 6.2: UWB Transmit Antenna Array: (a) Tightly Coupled Dipole Array (b) Antipodal Vivaldi Antenna Element

design reduces the number of active phase shifters, because the left/right edge illumination needs fast scanning, while the top edge illumination can be implemented with 90-degree panel rotation if false pair exists.

6.2 FMCW System

The previous radar system is Stepped Frequency Continuous Wave (SFCW) radar based on the network analyzer. This radar architecture has narrow instantaneous bandwidth but an effective wide bandwidth so it releases the specs of ADC and a signal processor. It also has higher SNR due to narrow noise bandwidth. In spite of these advantages, the SFCW is not suitable for the fast beam scanning and radar imaging due to the long sweep time. The impulse radar is another option for high resolution and fast refresh rate radar imaging system, which generates a short pulse, spanning over a wide bandwidth. The impulse radar requires the tolerance of high transient power level. In recent years, it became popular for low power application for its low radiated pulse energy but limited to short range detection. Given our system requirement, the Frequency Modulated Continuous Wave (FMCW) radar

is the best architecture to implement fast sweep imaging system.

There are several advantages of FMCW radar: (1) simultaneous transmission and reception leads to fast scanning, (2) reasonable range detection and hardware requirement, and (3) higher power of chirp pulse leads to more range of detection. The downconverted received signal is passed to an active filter to implement the range gating because the spectrum of the baseband signal corresponds to the range profile. Fig.6.3 demonstrates the future implementation of a real-time radar imaging system.

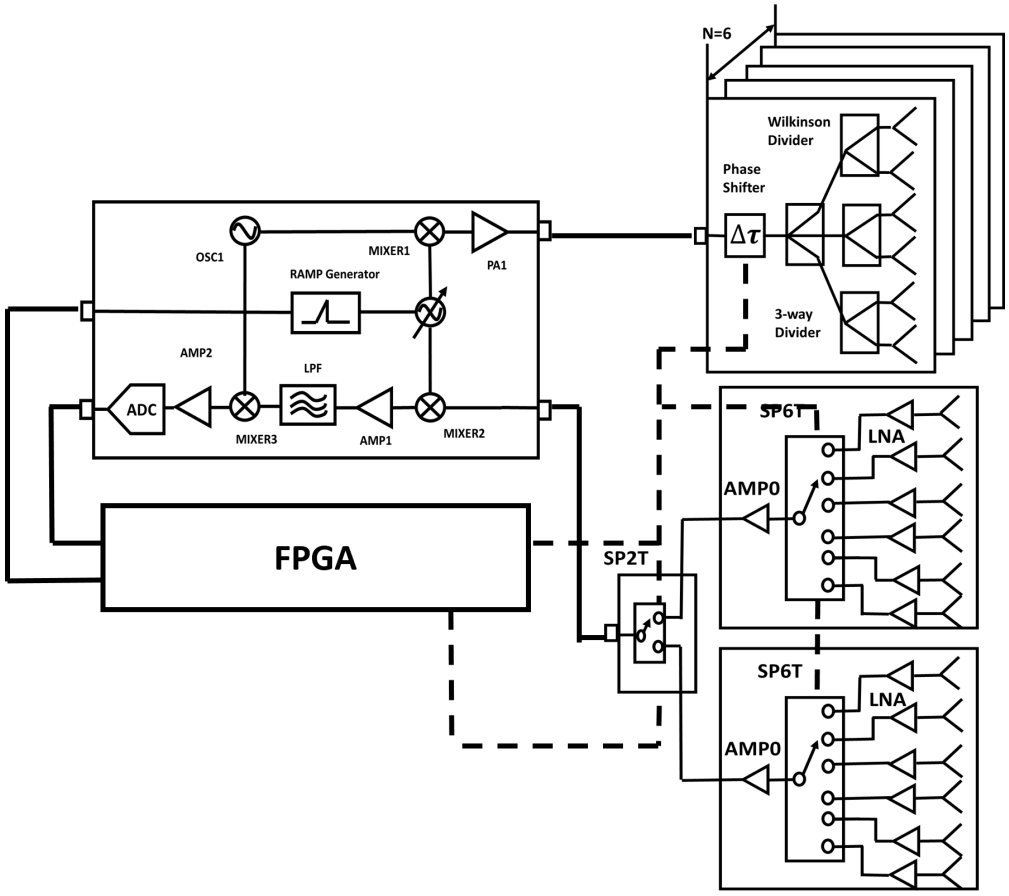

Figure 6.3: Complete FMCW System for Microwave Polarimetric Imaging (Solid line is signal path; dashed line is controlled bus)

6.3 Microwave Polarimetric Radar Imaging Algorithm

Given the antenna configuration is shown in Fig.5.9, the proposed microwave system enables the polarimetric radar imaging algorithm, as the polarimetric scattering response can be formulated. The Horizontal-to-Horizontal (H-to-H) and Vertical-to-Vertical (V-to-V) shows the ripples in the reconstructed image between the wall (either dielectric wall or metallic wall) and the antenna array due to the multiple reflections. However, it has been reported in [24] that such ripples can be effectively suppressed by looking at the cross-polarization response. This phenomenon is very useful for our case.

Moreover, the paper [97] also shows that the comparison of co-polarization image and cross polarization image gives the additional information about the object to be imaged. In a similar way, our system can, therefore, classify the object or exclude the erroneous detection.

Chapter 7

CONCLUSION

My past researches focus on the analytical formulation, algorithm development and hardware design of microwave antenna array system in two applications: wireless power transmission (WPT) and radar imaging of obscured objects by hard wall (metallic shield).

In the area of WPT, I have authored one book chapter, one journal paper, and two conference papers, based on my research at UW and internship work at Mitsubishi Electric Research Lab(MERL). The study on WPT involves the optimal beamforming algorithm development with numerical studies, experiment demonstration of WPT system with an antenna array, and design work of injection locked oscillator array. The relevant work has been summarized in Chapter 2.

In the area of radar imaging, I have authored and co-authored two journal papers, one letter paper, and three conference papers. These papers are all based on the sponsored project by Office of Naval Research Lab. This project explored the modified time reversal imaging technique with numerical simulations (Chapter 3) and demonstrated a multistatic radar imaging system (Chapter 4) verify this algorithm in the experiment. This imaging system is upgraded to a bistatic MIMO configuration and employs a new imaging algorithm, which combines the adaptive nulling and Direction-of-Arrival (DoA) estimation (Chapter 4). This system is further upgraded with a new Ultrawideband(UWB) receive array to reduce the signal-to-clutter ratio (Chapter 5).

Also, I have co-authored several journal and conference papers about the analytical studies of imaging in random and complex medium, which are not shown in this dissertation but summarized in the following section.

7.1 Publications

- **Book Chapters**

  [B1] **Ce Zhang**, Bingnan Wang, Akira Ishimaru and Yasuo Kuga, Optimal Array Beamforming for Microwave Power Transmission in Complex Environment, *Wireless Power Transfer Algorithms and Applications in Ad hoc Communication Networks*, Springer Press, 2016 (Accepted)

- **Journal Papers**

  [J1] **Ce Zhang**, and Y. Kuga, A Unidirectional Stacked Cross Dipole Array for UWB Microwave Imaging Applications, *IEEE Antennas and Wireless Propagation Letters*, 2016 (In Revision)

  [J2] **Ce Zhang**, Y. Kuga and A. Ishimaru, Hard Wall Radar Imaging: Localization of Objects Shadowed by Metallic Walls with Distributed MIMO, *Antennas and Propagation, IEEE Transactions on*, 2016 (To be submitted)

  [J3] **Ce Zhang**, A. Ishimaru, Y. Kuga, Optimal Wireless Power Transmission with Arbitrary Beamforming Array based on Time Reversal Signal Processing, *Antennas and Propagation, IEEE Transactions on*, 2016 (To be submitted)

  [J4] A. Ishimaru, **Ce Zhang**, Y. Kuga, Hard Wall Imaging of Objects Hidden by Non-penetrating Obstacles Using Modified Time Reversal Technique, *Antennas and Propagation, IEEE Transactions on* ,Volume: 62,Issue: 7

  [J5] A. Ishimaru, **Ce Zhang**,M. Stoneback, Y. Kuga, Time-reversal imaging of objects near rough surfaces based on surface flattening transform, *Waves in Random and Complex Media* ,23, no. 3 (2013): 306- 317

  [J6] A. Ishimaru, **Ce Zhang** , Y. Kuga, Statistical Maxwell's Electromagnetic Theories applied to Imaging of Objects in Geophysical and Biological Media (Invited Paper),*Progress In Electromagnetics Research*,Vol. 151, 17-31, 2015

- **Conference Papers**

[C1] **Ce Zhang**, Bingnan Wang, and Koon Hoo Teo, High Efficiency and Scalable Injection-locked Oscillator Array for Wireless Power Transmission,*Progress In Electromagnetics Research Symposium, Shanghai, China*, August 8-11, 2016

[C2] A. Ishimaru, Y. Kuga and **Ce Zhang**, Stochastic Wave Theory applied to SEISMIC CODA waves of P (pressure), S (shear), and Rayleigh surface waves in random media,*URSI Asia-Pacific Radio Science Conference, Seoul, Korea*, August 2016

[C3] A. Ishimaru, Y. Kuga and **Ce Zhang**, Integration of Statistical Wave Theories with Heat Diffusion, Signal Processing, and Seismic Wave Fluctuations,*Progress In Electromagnetics Research Symposium, Shanghai, China*, August 8-11, 2016

[C4] **Ce Zhang**, A. Ishimaru, Y. Kuga, Hard Wall Radar Imaging: Localization of Multiple Objects Shadowed by Metallic Walls with Bistatic Mode MIMO Radar System, *IEEE International Symposium on Antennas and Propagation and North American Radio Science Meeting (APSURSI) in Vancouver, Canada*, July 19-25, 2015

[C5] A. Ishimaru, **Ce Zhang**, Y. Kuga, Improved Image Resolution of Target Near Rough Surfaces Using Generalized Memory Effects of Angular and Frequency Correlations, *IEEE International Symposium on Antennas and Propagation and North American Radio Science Meeting (APSURSI) in Vancouver, Canada*, July 19-25, 2015

[C6] A. Ishimaru, **Ce Zhang**, Y. Kuga, Statistical electromagnetic theories and applications: A review of recent advances, *URSI Atlantic Radio Science Conference (URSI AT-RASC)*, 18-25 May 2015.

[C7] **Ce Zhang**, Akira Ishimaru, Yasuo Kuga, Experimental studies of "Hard Wall Radar Imaging" of objects shielded from line-of-sight, *2014 IEEE International Symposium on Antennas and Propagation and USNC-URSI National Radio Science Meeting Memphis,TN*,6-11 July 2014

[C8] A. Ishimaru, **Ce Zhang**, Y. Kuga, Statistical Electromagnetic Theories Applied to Imaging in Geophysical and Biological Random Media, *Progress In Electromagnetics Research Symposium, Guangzhou, China*, August 25-28, 2014

[C9] **Ce Zhang** , A. Ishimaru, Y. Kuga, Optimal Microwave Power Transfer through

Unknown Region Based On Time Reversal Technique, *USNC-URSI National Radio Science Meeting in Boulder, Colorado*, Jan 8-11, 2014

[C10] **Ce Zhang** , A. Ishimaru, Y. Kuga, Microwave Imaging of Objects Hidden by Non-penetrating Obstacles Using Time Reversal Imaging Technique,*USNC-URSI National Radio Science Meeting in Boulder, Colorado*, Jan 8-11, 2014

[C11] **Ce Zhang**, A. Ishimaru, M. Stoneback, Y. Kuga, Time-Reversal and MUSIC imaging of objects near rough surface based on surface flattening transform, *USNC-URSI National Radio Science Meeting in Boulder, Colorado*, Jan 8-11, 2013

[C12] A. Ishimaru, **Ce Zhang**, M. Stoneback, Y. Kuga, Hard Wall Imaging of Objects hidden by non-penetrating obstacles using Time Reversal technique, *IEEE International Symposium on Antennas and Propagation and USNC-URSI National Radio Science Meeting (APSURSI), Orlando, Florida*, July 7-13, 2013

[C13] A. Ishimaru, **Ce Zhang** ,M. Stoneback, Y. Kuga . "Imaging of objects near rough surfaces based on time-reversal signal processing and surface flattening transform." *Proceedings of 2013 URSI International Symposium on. IEEE Electromagnetic Theory (EMTS)*

[C14] A. Ishimaru, **Ce Zhang**, M. Stoneback, Y. Kuga, Imaging of Objects Located Close to Rough Surfaces Based on Surface Flattening Transform and Time-Reversal Imaging, *IEEE International Symposium on Antennas and Propagation and USNC-URSI National Radio Science Meeting(APSURSI)*, July 8-14, Chicago, IL.

BIBLIOGRAPHY

[1] Grzegorz Adamiuk, Thomas Zwick, and Werner Wiesbeck. Uwb antennas for communication systems. *Proceedings of the IEEE*, 100(7):2308–2321, 2012.

[2] Robert Adler. A study of locking phenomena in oscillators. *Proceedings of the IRE*, 34(6):351–357, 1946.

[3] Fauzia Ahmad, Yimin Zhang, and Moeness G Amin. Three-dimensional wideband beamforming for imaging through a single wall. *Geoscience and Remote Sensing Letters, IEEE*, 5(2):176–179, 2008.

[4] Moeness G Amin. *Through-the-wall radar imaging*. CRC press, 2011.

[5] Jørgen Bach Andersen and Rodney G Vaughan. Transmitting, receiving, and scattering properties of antennas. *Antennas and Propagation Magazine, IEEE*, 45(4):93–98, 2003.

[6] Daniel Arnitz and Matthew S Reynolds. Multitransmitter wireless power transfer optimization for backscatter rfid transponders. *Antennas and Wireless Propagation Letters, IEEE*, 12:849–852, 2013.

[7] Edward J Baranoski. Through-wall imaging: Historical perspective and future directions. *Journal of the Franklin Institute*, 345(6):556–569, 2008.

[8] Joel Birkeland and Tatsuo Itoh. A 16 element quasi-optical fet oscillator power combining array with external injection locking. *Microwave Theory and Techniques, IEEE Transactions on*, 40(3):475–481, 1992.

[9] William C Brown. Adapting microwave techniques to help solve future energy problems. In *1973 IEEE G-MTT International Microwave Symposium*, pages 189–191, 1973.

[10] Kenneth E Browne, Robert J Burkholder, and John L Volakis. Through-wall opportunistic sensing system utilizing a low-cost flat-panel array. *Antennas and Propagation, IEEE Transactions on*, 59(3):859–868, 2011.

[11] Kenneth Bullington. Characteristics of beyond-the-horizon radio transmission. *Proceedings of the IRE*, 43(10):1175–1180, 1955.

[12] Keith Carver and James Mink. Microstrip antenna technology. *Antennas and Propagation, IEEE Transactions on*, 29(1):2–24, 1981.

[13] Paul C Chang, Robert J Burkholder, and John L Volakis. Model-corrected microwave imaging through periodic wall structures. *International Journal of Antennas and Propagation*, 2012, 2012.

[14] Paul C Chang, Robert J Burkholder, John L Volakis, Ronald J Marhefka, and Yakup Bayram. High-frequency em characterization of through-wall building imaging. *Geoscience and Remote Sensing, IEEE Transactions on*, 47(5):1375–1387, 2009.

[15] J-X Chen, Kwok Wai Lau, Kam Yuen Chan, Ching Hong Kevin Chin, Quan Xue, and Chi Hou Chan. A double-sided parallel-strip line push–pull oscillator. *Microwave and Wireless Components Letters, IEEE*, 18(5):335–337, 2008.

[16] Jinli Chen, Hong Gu, and Weimin Su. A new method for joint dod and doa estimation in bistatic mimo radar. *Signal Processing*, 90(2):714–718, 2010.

[17] Jonghoon Choi, Morteza Nick, and Amir Mortazawi. Low phase-noise planar oscillators employing elliptic-response bandpass filters. *Microwave Theory and Techniques, IEEE Transactions on*, 57(8):1959–1965, 2009.

[18] Alvin Clavin, Donald A Huebner, and Francis J Kilburg. An improved element for use in array antennas. *Antennas and Propagation, IEEE Transactions on*, 22(4):521–526, 1974.

[19] Robert E Collin and Francis J Zucker. Antenna theory, 1969.

[20] Anthony Cresp, Ioannis Aliferis, MJ Yedlin, Ch Pichot, and J-Y Dauvignac. Investigation of time-reversal processing for surface-penetrating radar detection in a multiple-target configuration. In *Radar Conference, 2008. EuRAD 2008. European*, pages 144–147. IEEE, 2008.

[21] Afshin S Daryoush. Optical synchronization of millimeter-wave oscillators for distributed architecture. *Microwave Theory and Techniques, IEEE Transactions on*, 38(5):467–476, 1990.

[22] Anthony J Devaney. *Mathematical foundations of imaging, tomography and wavefield inversion*. Cambridge University Press, 2012.

[23] Jonathan P Doane, Kubilay Sertel, and John L Volakis. A wideband, wide scanning tightly coupled dipole array with integrated balun (tcda-ib). *IEEE Transactions on Antennas and Propagation*, 61(9):4538–4548, 2013.

[24] Traian Dogaru and Calvin Le. Simulation of a polarimetric radar imaging system using realistic antenna patterns. In *Proceedings of the 2012 IEEE International Symposium on Antennas and Propagation*, pages 1–2. IEEE, 2012.

[25] Gregory D Durgin. The practical behavior of various edge-diffraction formulas. *Antennas and Propagation Magazine, IEEE*, 51(3):24–35, 2009.

[26] Geoffrey F Edelmann, T Akal, William S Hodgkiss, Seongil Kim, William A Kuperman, and Hee Chun Song. An initial demonstration of underwater acoustic communication using time reversal. *Oceanic Engineering, IEEE Journal of*, 27(3):602–609, 2002.

[27] Mathias Fink. Time reversal of ultrasonic fields. i. basic principles. *Ultrasonics, Ferroelectrics, and Frequency Control, IEEE Transactions on*, 39(5):555–566, 1992.

[28] Mathias Fink. Time-reversal mirrors. *Journal of Physics D: Applied Physics*, 26(9):1333, 1993.

[29] Mathias Fink. Time reversed acoustics. *Physics today*, 50:34, 1997.

[30] Mathias Fink, Claire Prada, Francois Wu, and Didier Cassereau. Self focusing in inhomogeneous media with time reversal acoustic mirrors. In *Ultrasonics Symposium, 1989. Proceedings., IEEE 1989*, pages 681–686. IEEE, 1989.

[31] Isaac Freund. Looking through walls and around corners. *Physica A: Statistical Mechanics and its Applications*, 168(1):49–65, 1990.

[32] Jacob Gavan and Saad Tapuchi. Microwave wireless-power transmission to high-altitude-platform systems. *The Radio Science Bulletin*, 334:25–42, 2010.

[33] Debalina Ghosh, Arijit De, Mary C Taylor, Tapan K Sarkar, Michael C Wicks, and Eric L Mokole. Transmission and reception by ultra-wideband (uwb) antennas. *Antennas and Propagation Magazine, IEEE*, 48(5):67–99, 2006.

[34] Yu-Chun Guo, Xiao-Wei Shi, and Lei Chen. Retrodirective array technology. *Progress In Electromagnetics Research B*, 5:153–167, 2008.

[35] Alexander M Haimovich, Rick S Blum, and Leonard J Cimini. Mimo radar with widely separated antennas. *Signal Processing Magazine, IEEE*, 25(1):116–129, 2008.

[36] Robert C Hansen. Geometric theory of diffraction. *Geometric theory of diffraction., by Hansen, RC. IEEE Press Selected Reprint Series. New York, NY (USA): John Wiley & Sons, 7+ 406 p.*, 1, 1981.

[37] Yukihiro Homma, Takuro Sasaki, Koji Namura, Fuminori Sameshima, Tsuyoshi Ishikawa, Hiroki Sumino, and Naoki Shinohara. New phased array and rectenna array systems for microwave power transmission research. In *Microwave Workshop Series on Innovative Wireless Power Transmission: Technologies, Systems, and Applications (IMWS), 2011 IEEE MTT-S International*, pages 59–62. IEEE, 2011.

[38] Mai Ishiba, Jun Ishida, Kimiya Komurasaki, and Yoshihiro Arakawa. Wireless power transmission using modulated microwave. In *Microwave Workshop Series on Innovative Wireless Power Transmission: Technologies, Systems, and Applications (IMWS), 2011 IEEE MTT-S International*, pages 51–54. IEEE, 2011.

[39] Akira Ishimaru. *Electromagnetic wave propagation, radiation, and scattering*, volume 1. Prentice Hall Englewood Cliffs, NJ, 1991.

[40] Akira Ishimaru, Sermsak Jaruwatanadilok, and Yasuo Kuga. Wireless communications through unknown obscuring media by using time-reversal technique. *IEEE AP Communications*, 2005.

[41] Akira Ishimaru, Sermsak Jaruwatanadilok, and Yasuo Kuga. Imaging through random multiple scattering media using integration of propagation and array signal processing. *Waves in Random and Complex Media*, 22(1):24–39, 2012.

[42] Akira Ishimaru, Ce Zhang, and Yasuo Kuga. Hard wall imaging of objects hidden by non-penetrating obstacles using modified time reversal technique. *Antennas and Propagation, IEEE Transactions on*, 62(7):3645–3651, 2014.

[43] Akira Ishimaru, Ce Zhang, M Stoneback, and Yasuo Kuga. Imaging of objects near rough surfaces based on time-reversal signal processing and surface flattening transform. In *Electromagnetic Theory (EMTS), Proceedings of 2013 URSI International Symposium on*, pages 1019–1022. IEEE, 2013.

[44] Akira Ishimaru, Ce Zhang, M Stoneback, and Yasuo Kuga. Time-reversal imaging of objects near rough surfaces based on surface flattening transform. *Waves in Random and Complex Media*, 23(3):306–317, 2013.

[45] Sermsak Jaruwatanadilok, Akira Ishimaru, and Yasuo Kuga. Optimum wireless communication through unknown obscuring environments using the time-reversal principle: theory and experiments. In *Ultra-Wideband Short-Pulse Electromagnetics 8*, pages 105–112. Springer, 2007.

[46] Tutku Karacolak and Erdem Topsakal. A double-sided rounded bow-tie antenna (dsrba) for uwb communication. *Antennas and Wireless Propagation Letters, IEEE*, 5(1):446–449, 2006.

[47] Justin A Kasemodel, Chi-Chih Chen, and John L Volakis. Wideband planar array with integrated feed and matching network for wide-angle scanning. *IEEE Transactions on Antennas and Propagation*, 61(9):4528–4537, 2013.

[48] Joseph B Keller. Geometrical theory of diffraction. *JOSA*, 52(2):116–130, 1962.

[49] APS Khanna. Microwave oscillators: the state of the technology. *Microwave journal*, 49(4):22, 2006.

[50] Katsuki Kiminami, Akimasa Hirata, and Toshiyuki Shiozawa. Double-sided printed bow-tie antenna for uwb communications. *IEEE antennas and wireless propagation letters*, 1(3):152–153, 2004.

[51] Do-Hoon Kwon. On the radiation q and the gain of crossed electric and magnetic dipole moments. *Antennas and Propagation, IEEE Transactions on*, 53(5):1681–1687, 2005.

[52] David B Leeson. A simple model of feedback oscillator noise spectrum. *Proceedings of the IEEE*, pages 329–330, 1966.

[53] Lianlin Li, Wenji Zhang, and Fang Li. A novel autofocusing approach for real-time through-wall imaging under unknown wall characteristics. *Geoscience and Remote Sensing, IEEE Transactions on*, 48(1):423–431, 2010.

[54] Mingjian Li and Kwai-Man Luk. A differential-fed magneto-electric dipole antenna for uwb applications. *Antennas and Propagation, IEEE Transactions on*, 61(1):92–99, 2013.

[55] Ying Li and Vikram Jandhyala. Design of retrodirective antenna arrays for short-range wireless power transmission. *Antennas and Propagation, IEEE Transactions on*, 60(1):206–211, 2012.

[56] Jenshan Lin and Tatsuo Itoh. Active integrated antennas. *Microwave Theory and Techniques, IEEE Transactions on*, 42(12):2186–2194, 1994.

[57] Yu-Tsung Lo and Jean-Fu Kiang. Comparison of injection-locked and coupled oscillator arrays for beamforming. *Microwave Theory and Techniques, IEEE Transactions on*, 63(4):1353–1360, 2015.

[58] Kwai-Man Luk and Hang Wong. A new wideband unidirectional antenna element. *Int. J. Microw. Opt. Technol*, 1(1):35–44, 2006.

[59] Nadia Maaref, Patrick Millot, Xavier Ferrières, Christian Pichot, and Odile Picon. Electromagnetic imaging method based on time reversal processing applied to through-the-wall target localization. *Progress In Electromagnetics Research M*, 1:59–67, 2008.

[60] Ka-Ming Mak, Hang Wong, and Kwai-Man Luk. A shorted bowtie patch antenna with a cross dipole for dual polarization. *Antennas and Wireless Propagation Letters, IEEE*, 6:126–129, 2007.

[61] Andrea Massa, Giacomo Oliveri, Federico Viani, and Paolo Rocca. Array designs for long-distance wireless power transmission: State-of-the-art and innovative solutions. *Proceedings of he IEEE*, 101(6):1464–1480, 2013.

[62] James O McSpadden and John C Mankins. Space solar power programs and microwave wireless power transmission technology. *Microwave Magazine, IEEE*, 3(4):46–57, 2002.

[63] Aidin Mehdipour, Karim Mohammadpour-Aghdam, Reza Faraji-Dana, and Abdel-Razik Sebak. Modified slot bow-tie antenna for uwb applications. *Microwave and Optical Technology Letters*, 50(2):429–432, 2008.

[64] Hung Tuan Nguyen, Jørgen Bach Andersen, and Gert Frølund Pedersen. The potential use of time reversal techniques in multiple element antenna systems. *IEEE Communications Letters*, 9(1):40–42, 2005.

[65] Lam Nguyen, Marc Ressler, and Jeffrey Sichina. Sensing through the wall imaging using the army research lab ultra-wideband synchronous impulse reconstruction (UWB SIRE) radar. In *SPIE Defense and Security Symposium*, pages 69470B–69470B. International Society for Optics and Photonics, 2008.

[66] Yasuhisa Oda, Toshikazu Yamaguchi, Kimiya Komurasaki, Ken Kajiwara, Koji Takahashi, and Keishi Sakamoto. An experimental study on high power millimeter wave beam transmission for microwave beaming propulsion. In *Microwave Workshop Series on Innovative Wireless Power Transmission: Technologies, Systems, and Applications (IMWS), 2011 IEEE MTT-S International*, pages 181–184. IEEE, 2011.

[67] Akira Oida, Hiroshi Nakashima, Juro Miyasaka, Katsuaki Ohdoi, Hiroshi Matsumoto, and Naoki Shinohara. Development of a new type of electric off-road vehicle powered by microwaves transmitted through air. *Journal of Terramechanics*, 44(5):329–338, 2007.

[68] Giacomo Oliveri, Lorenzo Poli, and Andrea Massa. Maximum efficiency beam synthesis of radiating planar arrays for wireless power transmission. *Antennas and Propagation, IEEE Transactions on*, 61(5):2490–2499, 2013.

[69] Henry Oman. Electric car progress. *Aerospace and Electronic Systems Magazine, IEEE*, 17(6):30–35, 2002.

[70] Sophocles J Orfanidis. *Electromagnetic waves and antennas*. Rutgers University, 2002.

[71] David Pozar. Scattered and absorbed powers in receiving antennas. *Antennas and Propagation Magazine, IEEE*, 46(1):144–145, 2004.

[72] Claire Prada and Mathias Fink. Eigenmodes of the time reversal operator: A solution to selective focusing in multiple-target media. *Wave motion*, 20(2):151–163, 1994.

[73] Claire Prada, Sébastien Manneville, Dimitri Spoliansky, and Mathias Fink. Decomposition of the time reversal operator: Detection and selective focusing on two scatterers. *The Journal of the Acoustical Society of America*, 99:2067, 1996.

[74] Claire Prada and Jean-Louis Thomas. Experimental subwavelength localization of scatterers by decomposition of the time reversal operator interpreted as a covariance matrix. *The Journal of the Acoustical Society of America*, 114:235, 2003.

[75] Yongxi Qian and Tatsuo Itoh. Progress in active integrated antennas and their applications. *Microwave Theory and Techniques, IEEE Transactions on*, 46(11):1891–1900, 1998.

[76] Yahya Rahmat-Samii. Gtd, utd, uat, and std: a historical revisit and personal observations. *Antennas and Propagation Magazine, IEEE*, 55(3):29–40, 2013.

[77] Frank C Robey, Scott Coutts, Dennis Weikle, Jeffrey C McHarg, and Kevin Cuomo. Mimo radar theory and experimental results. In *Signals, Systems and Computers, 2004. Conference Record of the Thirty-Eighth Asilomar Conference on*, volume 1, pages 300–304. IEEE, 2004.

[78] Khan MZ Shams and Mohammod Ali. Wireless power transmission to a buried sensor in concrete. *Sensors Journal, IEEE*, 7(12):1573–1577, 2007.

[79] Naoki Shinohara. *Wireless power transfer via radiowaves*. John Wiley & Sons, 2014.

[80] Francesco Soldovieri and Raffaele Solimene. Through-wall imaging via a linear inverse scattering algorithm. *Geoscience and Remote Sensing Letters, IEEE*, 4(4):513–517, 2007.

[81] Arnold Sommerfeld. Optics lectures on theortical physics, vol. iv. *Optics Lectures on Theortical Physics, Vol. IV by Arnold Sommerfeld New York, NY: Academic Press INC, 1954*, 1, 1954.

[82] Hee C Song, WS Hodgkiss, WA Kuperman, M Stevenson, and T Akal. Improvement of time-reversal communications using adaptive channel equalizers. *Oceanic Engineering, IEEE Journal of*, 31(2):487–496, 2006.

[83] Lin-Ping Song, Chun Yu, and Qing Huo Liu. Through-wall imaging (twi) by radar: 2-d tomographic results and analyses. *Geoscience and Remote Sensing, IEEE Transactions on*, 43(12):2793–2798, 2005.

[84] Tomohiro Takahashi, Tomohiro Mizuno, Manabu Sawa, Takuro Sasaki, Toru Takahashi, and Naoki Shinohara. Development of phased array for high accurate microwave power transmission. In *Microwave Workshop Series on Innovative Wireless Power Transmission: Technologies, Systems, and Applications (IMWS), 2011 IEEE MTT-S International*, pages 157–160. IEEE, 2011.

[85] Chao-Hsiung Tseng and Chih-Lin Chang. Design of low phase-noise microwave oscillator and wideband vco based on microstrip combline bandpass filters. *Microwave Theory and Techniques, IEEE Transactions on*, 60(10):3151–3160, 2012.

[86] Vijayaraghavan Venkatasubramanian and Henry Leung. A novel chaos-based high-resolution imaging technique and its application to through-the-wall imaging. *Signal Processing Letters, IEEE*, 12(7):528–531, 2005.

[87] Joao Vieira, Steffen Malkowsky, Karl Nieman, Zachary Miers, Nikhil Kundargi, Liang Liu, Ian Wong, Viktor Owall, Ove Edfors, and Fredrik Tufvesson. A flexible 100-antenna testbed for massive mimo. In *Globecom Workshops (GC Wkshps), 2014*, pages 287–293. IEEE, 2014.

[88] James R Wait. Distortion of an elf pulse after propagation through an antipode. *Journal of Geophysical Research*, 74(11):2982–2986, 1969.

[89] Werner Wiesbeck, Grzegorz Adamiuk, and Christian Sturm. Basic properties and design principles of uwb antennas. *Proceedings of the IEEE*, 97(2):372–385, 2009.

[90] Hang Wong, Ka-Ming Mak, and Kwai-Man Luk. Wideband shorted bowtie patch antenna with electric dipole. *Antennas and Propagation, IEEE Transactions on*, 56(7):2098–2101, 2008.

[91] Bi Qun Wu and Kwai-Man Luk. A broadband dual-polarized magneto-electric dipole antenna with simple feeds. *Antennas and Wireless Propagation Letters, IEEE*, 8:60–63, 2009.

[92] Biqun Wu and Kwai-Man Luk. A uwb unidirectional antenna with dual-polarization. *Antennas and Propagation, IEEE Transactions on*, 59(11):4033–4040, 2011.

[93] ADavid Wunsch. The receiving antenna: a classroom presentation. *Antennas and Propagation Magazine, IEEE*, 53(4):179–187, 2011.

[94] Yunqiang Yang and Aly E Fathy. See-through-wall imaging using ultra wideband short-pulse radar system. In *Antennas and Propagation Society International Symposium, 2005 IEEE*, volume 3, pages 334–337. IEEE, 2005.

[95] Mehmet Emre Yavuz and Fernando L Teixeira. Space–frequency ultrawideband time-reversal imaging. *Geoscience and Remote Sensing, IEEE Transactions on*, 46(4):1115–1124, 2008.

[96] Mehmet Emre Yavuz and Fernando L Teixeira. Ultrawideband microwave sensing and imaging using time-reversal techniques: A review. *Remote Sensing*, 1(3):466–495, 2009.

[97] Konstantin M Yemelyanov, Nader Engheta, Ahmad Hoorfar, and John A McVay. Adaptive polarization contrast techniques for through-wall microwave imaging applications. *Geoscience and Remote Sensing, IEEE Transactions on*, 47(5):1362–1374, 2009.

[98] Hristomir Yordanov, MT Ivrlač, Peter Russer, and Josef A Nossek. Arrays of isotropic radiators–a field-theoretic justification. In *Proc. ITG/IEEE Workshop on Smart Antennas*, 2009.

[99] Robert York, Tatsuo Itoh, et al. Injection-and phase-locking techniques for beam control [antenna arrays]. *Microwave Theory and Techniques, IEEE Transactions on*, 46(11):1920–1929, 1998.

[100] Ce Zhang, Akira Ishimaru, and Yasuo Kuga. Time-reversal and music imaging of objects near rough surface based on surface flattening transform. In *Radio Science Meeting (USNC-URSI NRSM), 2013 US National Committee of URSI National*. URSI, 2013.

[101] Ce Zhang, Akira Ishimaru, and Yasuo Kuga. Experimental studies of hard wall radar imaging of objects shielded from line-of-sight. In *Radio Science Meeting (Joint with AP-S Symposium), 2014 USNC-URSI*, pages 52–52. IEEE, 2014.

[102] Ce Zhang, Akira Ishimaru, and Yasuo Kuga. Optimal microwave power transfer through unknown region based on time reversal technique. In *Radio Science Meeting (USNC-URSI NRSM), 2014 United States National Committee of URSI National*, pages 1–1. IEEE, 2014.

[103] W. J. Zhang and A. Hoorfar. Three-dimensional real-time through-the-wall radar imaging with diffraction tomographic algorithm. *TRANSACTIONS ON GEOSCIENCE AND REMOTE SENSING, IEEE*, 51(7):4155–4163, 2013.

[104] Wenji Zhang, Ahmad Hoorfar, and Lim Li. Through-the-wall target localization with time reversal music method. *Progress In Electromagnetics Research*, 106:75–89, 2010.

[105] Deshuang Zhao, Yuanwei Jin, Bing-Zhong Wang, and Rui Zang. Time reversal based broadband synthesis method for arbitrarily structured beam-steering arrays. *Antennas and Propagation, IEEE Transactions on*, 60(1):164–173, 2012.

[106] Wenjun Zheng, Zhiqin Zhao, Zai-Ping Nie, and Qing Huo Liu. Evaluation of trm in the complex through wall environment. *Progress In Electromagnetics Research*, 90:235–254, 2009.

[107] Shengli Zhou and Georgios B Giannakis. Optimal transmitter eigen-beamforming and space-time block coding based on channel mean feedback. *Signal Processing, IEEE Transactions on*, 50(10):2599–2613, 2002.